DOE/ET-53088-325 IFSR#325

Topics in Stability and Transport in Tokamaks: Dynamic Transition to Second Stability with Auxiliary Heating; Stability of Global Alfvén Waves in an Ignited Plasma

Guo-Yong Fu
Institute for Fusion Studies
The University of Texas at Austin
Austin, Texas 78712

July 1988

TOPICS IN STABILITY AND TRANSPORT IN TOKAMAKS: DYNAMIC TRANSITION TO SECOND STABILITY WITH AUXILIARY HEATING; STABILITY OF GLOBAL ALFVÉN WAVES IN AN IGNITED PLASMA

by

GUO-YONG FU, B.S.

DISSERTATION

Presented to the Faculty of the Graduate School of

The University of Texas at Austin

in Partial Fulfillment

of the Requirements

for the Degree of

DOCTOR OF PHILOSOPHY

THE UNIVERSITY OF TEXAS AT AUSTIN

AUGUST, 1988

TOPICS IN STABILITY AND TRANSPORT IN TOKAMAKS: DYNAMIC TRANSITION TO SECOND STABILITY WITH AUXILIARY HEATING; STABILITY OF GLOBAL ALFVÉN WAVES IN AN IGNITED PLASMA

APPROVED BY

SUPERVISORY COMMITTEE:

R D Hazeltine

Marshall N Rosenbluth

James W. VanDam

Edward J Powers Jr

Wendell Horton Jr

P. H. Diamond

To my parents and my brother.

Acknowledgments

It has been an extraordinary experience for me to learn from and work with Dr. James W. Van Dam. I am deeply grateful for his teaching me plasma physics, for his infinite accessibility, and for giving me great freedom to do research. His kindness and friendship have made me feel very comfortable.

It has been a great honor for me to learn from Prof. Marshall Rosenbluth. His deep physical insight has been my constant inspiration. Without his many suggestions and critical comments, this work would not have been possible.

I wish to express my deep gratitude to other menbers of my thesis committee: Drs. Patrick Diamond, Richard Hazeltine, Wendell Horton, and Edward Powers. Especially I want to thank Prof. Richard Hazeltine for sharing the burden of being my supervising professor since last fall. Also, I thank Prof. Patrick Diamond for his suggestions which lead to the work in Chap. 2.

It is a great pleasure to thank Dr. David Ross, who kindly provided me with the kinetic Alfvén code, which has been extended to toroidal geometry in Chap. 4. Many discussions with him made it much easier for me to understand this code and the physics of Alfvén waves. I am also pleased to thank Prof. Herbert Berk for his suggestions about curvature-induced electron Landau damping, and Dr. Swadesh Mahajan for his comments regarding kinetic effects on the MHD gap modes. I also wish to thank Dr. Rodolfo Carrera for reading my thesis and giving many helpful comments.

The Institute for Fusion Studies has provided an excellent scientific environment for me. In particular, I thank Carolyn Valentine, Joyce Patton, Dawn East, and Saralyn Stewart for their administrative assistance.

I also appreciate my officemates and fellow graduate students for their warm friendship: Dr. Y. Z. Zhang, W. Q. Li, Dr. C. Y. Chen, Dr. T. H. Chiueh, Dr. C. T. Hsu, Dr. N. Dominguez, J. H. Han, and John Cobb.

I wish to express my deep gratitude to Prof. T. D. Lee of Columbia University for his extraordinary efforts in arranging the CUSPEA program, which brought me to the United States.

Finally, I thank my parents and my brother for their support and understanding during this time.

GUO-YONG FU

The University of Texas at Austin
AUGUST, 1988

Abstract

In this thesis, the problem of access to the high-beta ballooning second stability regime by means of auxiliary heating and the problem of the stability of global shear Alfvén waves in an ignited tokamak plasma are theoretically investigated. These two problems are related to the confinement of both the bulk plasma as well as the fusion-product alpha particles and are fundamentally important to the operation of ignited tokamak plasma.

First, a model that incorporates both transport and ballooning mode stability was developed in order to estimate the auxiliary heating power required for a tokamak plasma to evolve in time self-consistently into a high-beta, globally self-stabilized equilibrium. The critical heating power needed for access to second stability is found to be proportional to the square root of the anomalous diffusivity induced by the ballooning instability. Also, the power scaling tends to favor tokamaks designed with large aspect ratio. For the parameters of the proposed Second Regime Experiment (SRX) tokamak, this theory is applied to obtain results that are close to those of a recent numerical simulation.

Next, the full effects of toroidicity are retained in a theoretical description of global-type shear Alfvén modes whose stability can be modified by the fusion product alpha particles that will be present in an ignited tokamak plasma. Toroidicity is found to induce mode coupling and to stabilize the so-called Global Alfvén Eigenmodes (GAE), whose frequencies are just below the minimum of the shear Alfvén continuous spectrum, as long as the mode frequency is embedded in the toroidal continuum. However, toroidicity also

induces gaps in the frequency continuum, within which discrete eigenmodes can exist; these toroidicity-induced Alfvén gap modes can be destabilized by the alpha particles through their transit resonance. Moreover, compared to the GAE modes, these gap modes have a larger growth rate over a wider range of values for the alpha particle density scale length, when parameters for the proposed Compact Ignition Tokamak are considered.

Table of Contents

List of Tables

List of Figures

Chapter 1

Introduction

1.1 Ballooning Mode Induced Anomalous Transport and Access to the Second Stability Regime

The main goal of magnetic confinement fusion research is to contain plasma in a magnetic bottle for a sufficiently long time and at sufficiently high density and temperature to produce fusion energy. Thus it is quite desirable to operate a tokamak plasma in a high beta regime, where beta is the ratio of the plasma thermal pressure to the magnetic stress pressure, since then the fusion energy output can be maximized. However, the magnetohydrodynamic (MHD) instabilities tend to limit the plasma beta to a low value.

The instabilities that limit beta are kink modes and ballooning modes. A limiting beta scaling due to free-boundary kink instabilities in a tokamak has been found by Troyon et al. [1] as $\beta < 0.14a/Rq$. Similarly, the ideal ballooning instability [2] limits beta to a low value $\beta < 0.28a/Rq$. These limits agree reasonably well with current tokamak experimental results. Thus, the issue of how to stabilize these two instabilities has been a primary concern to the fusion community and much progress has been achieved in recent years. The $n = m = 1$ internal kink mode is driven unstable at the $q = 1$ magnetic flux surface, where q is the safety factor. This mode can be stabilized by raising q at the magnetic axis above unity. For external kink modes, stabilization can be achieved by bringing the wall of tokamak close to the plasma surface. As for

ballooning modes, various schemes of stabilization have been found, e.g., hot particle stabilization [3,4,5], flux surface shaping [6,7], current profile control [8], etc. However, complete stabilization of ballooning modes is still very difficult, even if it is possible. Therefore it is believed that the ballooning instability is a major obstacle to the high-beta operation of tokamaks.

Ballooning modes are pressure-gradient-driven perturbations localized across the plasma radius. The term "ballooning" arises from the nature of the structure, which is localized along a magnetic field line in the regions of unfavorable curvature side, viz., the large-major-radius side of a tokamak. In the high-mode-number limit, the stability of an ideal ballooning mode at radius r can be described in term of two parameters: one is $\alpha = -(2Rq^2/B^2)dp/dr$, a measure of the pressure gradient, and the other is $S = (r/q)dq/dr$, the magnetic field shear. Here, p is the plasma pressure, R is the tokamak major radius, and B is the toroidal magnetic field. For a fixed value of shear S, the ballooning mode is stable for small pressure gradients, namely, $\alpha < \alpha_1(S)$, since the magnetic field shear has a stabilizing effect; i.e., energy must be spent in order to perturb the magnetic field for non-zero shear. When the value of α is increased so as to exceed the limit $\alpha = \alpha_1(S)$, the ballooning mode becomes unstable. However, as α is further increased to the so-called second stability limit at $\alpha = \alpha_2(S)$, the mode becomes stable again. This high-beta regime of operation is called "second stability". The existence of this second regime has been shown analytically and numerically [9,10,11], although experimental demonstration remains to be done.

The theoretical existence of the second stability regime at least opens up the possibility of operating a tokamak at high beta. The question of how the plasma can be brought from first stability across the unstable zone and

into second stability remains a serious problem. As was previously mentioned, various schemes have been proposed for obtaining access to the second regime. Another method, which is straightforward, albeit brute force, is to heat the plasma rapidly through the unstable zone such that the transition occurs before the unstable ballooning modes can develop and induce significant anomalous transport. This scheme has the merit of simplicity, although it suffers a serious disadvantage with the heating power requirement. An order-of-magnitude estimate indicates that at least several gigawatts of power are required to push a plasma through the unstable gap. It is not clear whether current and future technology will be able to meet such a prohibitive requirement. Meanwhile, other methods are more elaborate, such as hot particle stabilization [3,4,5] mentioned above, by which ballooning modes are partially stabilized to provide a bridge between the first and second stability regimes. However, complete stabilization over the whole plasma radius is still difficult to achieve. Therefore, it is inevitable that part of the plasma volume will likely undergo ballooning instability and experience anomalous transport associated with the instabilities, before complete access to the second regime is achieved.

In this work, we study how a tokamak plasma can self-consistently evolve to the second regime under the application of moderately large auxiliary heating power, with the assumption of some method (which need not be specified in detail) for the stabilization of ballooning modes at small shear. Our transport model follows, to some extent, from the works by Azumi et al. [12] and by Connor, Taylor and Turner [13]. The work by Azumi et al. concerned a detailed INTOR calculation in which the plasma pressure limit due to ballooning instability was studied. A $1\frac{1}{2}$–dimensional tokamak transport model [14] was applied in order to follow the evolution of tokamak equilibria subject to auxiliary heating. This model is derived from a flux surface average and can be

applied to complicated realistic tokamak equilibria. Starting from a force-free equilibrium, they examined at every time step the stability condition for ballooning modes: when the modes became unstable in some region, the plasma transport was enhanced accordingly. A simple prescription for very large heat conduction was assumed to apply in the unstable region, such that the pressure profile was fixed at each point at the marginally stable value. Eventually, a equilibrium that is marginally stable over the entire plasma minor radius was attained in the first stability regime.

In contrast with the detailed time-dependent transport calculation by Azumi et al., the work of Connor, Taylor, and Turner (hereafter abbreviated as CTT) was concerned with the general trend of confinement time and scaling. In their model, the plasma column was divided into three zones. The innermost zone, extending from the magnetic axis to the $q = 1$ surface, is the sawtooth zone; in the work to be described in this thesis, we neglect this zone by assuming $q(0) \geq 1$ and focus on the ballooning mode dynamics, which involves two zones. In the ballooning stable zone, the plasma profile was determined by a simple cylindrical steady-state transport equation; whereas in the unstable zone, a sufficiently large thermal diffusion was assumed due to the unstable modes, as in Azumi et al. [12], such that the pressure gradient was held at and thus determined by the first stability boundary. Then the pressure profile can be self-consistently obtained, along with the poloidal magnetic field (or, equivalently, the q profile) which is related to the pressure profile through Ohm's law. In this way, a confinement time scaling was obtained, which agreed fairly well with the empirical L-mode scaling [15].

Our transport model differs from that of CTT in several significant ways. First, in addition to developing several interesting extensions of the CTT

theory, we are primarily concerned with the problem of access to the second stability regime. The supplemental stabilization of ballooning modes that is assumed (e.g., hot particles or something else) provides plasma a route by which to access second stability, at least partially and possibly completely, under the application of enough auxiliary heating power, instead of the pressure gradient being limited by the first stability boundary as in the CTT model. Second, in our time-dependent model, a large but finite, continuously varying thermal diffusivity is assumed in the ballooning unstable zone, rather than the "quasi-infinite" diffusion of CTT that maintains marginal stability. Therefore a critical access power can be found, given the degree of transport enhancement due to instability.

Here, we should mention that a similar, but more sophisticated, transport model has recently been employed by the Columbia group [16] to study the second regime access problem, specifically for the proposed large-aspect-ratio SRX tokamak. In their treatment, a sequence of equilibria that evolve temporally from the first to the second regime of ballooning stability are generated by a version of the BALDUR transport code that calculates the two-dimensional evolution of the magnetic configuration self-consistently with the thermal and the particle diffusion. The stability boundary was recalculated at every time step, as in Azumi et al., and a finite enhancement of diffusion were introduced on the ballooning unstable flux surfaces, as in our model. The q profile was modified by neutral beam current drive so that $q_0 > 1$, which had the effect of reducing the size of the unstable region sufficiently to allow transition to the second regime at a reasonable heating power. We remark that although their model is more sophisticated than ours, when we apply our model to the same parameters, the basic results are very similar. Furthermore, whereas a detailed calculation is their main concern, we are more interested in the universal time-

dependent behavior of the transition and in the general trend of the critical access power and its scaling. Our results can be straightforwardly generalized to more realistic situations, as well.

Our principal results are the following:

1. Several interesting extensions of the CTT model were developed. We formulated and solved the nonlinear coupled transport equation in the CTT model as an eigenvalue problem with the use of the shooting method, instead of the method of functional iteration employed in the CTT approach. We found that CTT scaling is valid even at very large auxiliary heating power. Also an anomalous thermal diffusivity was obtained corresponding to the profiles determined by the CTT model and was compared with neutral beam injection results from the ISX-B experiment [17]. We found that the agreement is quite good for a relatively high beta case, but poor for the low beta case. Also, we obtained an improved CTT scaling when the stability effect of finite beta is included. Finally, the CTT model was applied to the high-beta, purely Ohmic-heated tokamak case, and a confinement scaling law obtained.

2. The CTT model was applied to study the the problem of access to the second stability regime, under the assumption that the ballooning mode is stabilized for small values of the shear. We found that, as the power is increased, the unstable volume of the plasma expands and confinement deteriorates. However, when the power is further increased, the unstable volume finally reaches the nadir point of the marginal stability boundary. At this point, a steady-state solution in the first regime no longer exists, although a steady-state in the second regime does exist. We then conclude that the plasma will somehow transit abruptly to the second regime, and accordingly the plasma confinement time will jump back to the INTOR value.

3. A time-dependent transport model with large but finite anomalous diffusion was constructed for the purpose of studying the dynamic transition into the second regime of stability. Compared to the steady-state approach mentioned in the preceeding paragraph, this model gives a smooth transition into second stability, if the power is sufficiently high. As the power is increased, the unstable volume at first expands, as mentioned above. However, as the power is further increased, the unstable volume actually begins to decrease, since part of the stable volume starts to enter the second regime. When the power finally reaches the critical access value, the plasma transits to a steady state in the second regime. We found, numerically and analytically, that this critical access power scales as the square root of the anomalous diffusivity for a flux-conserving tokamak. This power is much less demanding than that required for a non-flux-conserving tokamak, for which a heating power linearly proportional to the anomalous diffusivity is required.

1.2 The Stability of Toroidal Global Shear Alfvén Waves in the Presence of Fusion Product Alpha Particles

Now we turn to the second topic of this thesis: the stability of global-type toroidal shear Alfvén waves in presence of alpha particles in an ignited tokamak plasma. The effect of alpha particles on MHD waves is a fundamental problem in the consideration of tokamak ignition. Because the bulk plasma confinement is usually correlated with the MHD unstable behavior, the destabilization of MHD waves by alpha particles will likely induce anomalous transport of the bulk plasma, and even of the alpha particles themselves. As a result, the plasma confinement might be degraded and the alpha particle heating reduced.

The effect of energetic particles, such as alpha particles, on the MHD modes is significant since these hot particles behave differently from the background plasma fluid. For the background plasma, the particle magnetic drift frequency ω_d is much smaller than the MHD wave frequency: hence these fluid particles are said to be tied to the magnetic field lines or, in other words, the magnetic field lines are "frozen" in the plasma fluid. On the other hand, the drift frequency of the hot particles can be comparable to or larger than the MHD wave frequency ω. Thus, these hot particles can move off a magnetic field line and, as a result, their response to the field perturbation is not hydrodynamic. Therefore they can contribute to the plasma motion in a very interesting way. In the limit of $\omega_d >> \omega$, the energetic particles drift rapidly across the magnetic field lines and do not respond to the usual $\mathbf{E} \times \mathbf{B}$ drift. These particles thus constitute a "rigid" current ring which may create a magnetic well and stabilize low-frequency MHD modes: e.g., interchange modes in an Elmo Bumpy Torus (EBT) device [18,19,20] or ballooning modes in a tokamak [3].

However, these energetic particles can also resonantly interact with the MHD modes in the limit of $\omega_d \sim \omega$. In this case, the hot particles can destabilize the MHD wave because of the ordering $\omega_* \sim (R/L_n)\omega_d >> \omega$, where ω_* is the hot particle diamagnetic frequency, R is the major radius, and L_n is the density scale length of the energetic particles. The recently discovered fishbone instability [21], in which neutral beam-injected hot trapped ions are thought to excite the internal kink modes, provides such an example. Subsequently the ballooning modes were also found to be destabilized by the same type of resonant hot particles [22,23], thus serving as an explanation for the high-frequency fishbone "precursors" that were experimentally observed.

In the limit of $\omega_d < \omega$, the hot particles behave more or less like the background cold particles. However, the diamagnetic frequency of the hot particles can still be larger than the MHD wave frequency, due to the ordering $\omega_* \sim (R/L_n)\omega_d >> \omega_d$. This is especially true for fusion-product alpha particles, which are created with an energy of 3.52 MeV and with a density profile that is sharply peaked at the center of the plasma, due to the sensitive dependence of the fusion reaction rate on the plasma temperature. In this case, a drift-wave type of instability can be driven by the hot particles through their parallel wave-particle resonance $\omega = k_{\|}v_{\|}$, where $k_{\|}$ is the parallel wave number and $v_{\|}$ is the parallel velocity of the hot particles. Here we consider the destabilization of shear Alfvén waves by fusion-product alpha particles in an ignited tokamak by means of this mechanism.

In the ideal MHD limit with cylindrical symmetry, the shear Alfvén wave is governed by a second-order differential equation that admits a continuous frequency spectrum in the range $(\omega_A)_{min} < \omega < (\omega_A)_{max}$ [24,25]. Corresponding to this continuum, the eigenfunction is singular at $\omega = \omega_A(r)$, i.e., where the mode frequency intersects the continuum. However, it has been shown [26,27,28,29,30,31,32] that a discrete global mode, called the "global shear Alfvén eigenmode" (GAE), can exist with its frequency just below the minimum of the continuum, due to the plasma equilibrium current gradient. When nonideal effects such as finite Larmor radius (FLR) and electron Landau damping are considered, the continuum is discretized and the singular wavefunction becomes a regular, localized eigenmode called the kinetic Alfvén wave (KAW) [33]. These KAW are heavily damped by the electron Landau resonance since they are very localized. On the other hand, the GAE has a global wave structure which extends over most of the plasma radius, and is only slightly damped.

The destabilization of shear Alfvén waves was first studied qualitatively by Mikhailovskii [34], using a local dispersion relation. By including FLR effects to discretize the continuum, Rosenbluth and Rutherford [35] found that the kinetic Alfvén wave can be destabilized by alpha particles. Tsang et al. [36] studied the details of the same problem numerically and reached a similar conclusion. More recently, Li et al. [37] found that the global Alfvén wave (GAE) can also be destabilized in a similar manner.

In this thesis, the full effects of toroidicity are retained in a theoretical description of global-type Alfvén modes that can be destabilized by the alpha particles. Previous studies all assumed the large-aspect-ratio cylindrical limit and neglected toroidal mode coupling. Furthermore, the global-type shear Alfvén waves are our primary concern, since these global waves are negligibly damped and thus can be easily destabilized by alpha particles.

In a toroidal device, the poloidal mode number m is no longer a good "quantum" number, owing to the presence of toroidal coupling. It has been shown [38] that the toroidal shear Alfvén spectrum is still continuous in the MHD limit, although it is not a simple superposition of various cylindrical continua, since the toroidal coupling can shift the cylindrical continua upward or downward exactly as in a quantum system, in which a Hamiltonian perturbation results in shifts of the energy levels. Furthermore, there is a new phenomenon about the toroidal spectrum: that is, the toroidicity induces gaps in the continuum, owing to the degeneracy of the cylindrical continua. Again we can develop an analogy with the quantum mechanics textbook example in which a periodic potential perturbation produces energy gaps in an otherwise continuous energy spectrum for free electrons. However, we caution that this analogy is not exact. Unlike in the quantum system, in which energy levels

within the gap are forbidden, it has been shown that a discrete eigenmode exists within the toroidicity-induced gap in the Alfvén wave spectrum [39]. We call this mode the "toroidal shear Alfvén gap eigenmode" (TAGE). There is also another type of global eigenmode in toroidal geometry, namely, the toroidal version of the cylindrical GAE mentioned above. These two types of global modes will be our main concern in this study.

Toroidicity will induce sidebands that coupled to the cylindrical GAE mode. These sideband may become singular if the mode frequency is embedded in the shear Alfvén continuum. In another words, in a toroidal device the GAE can be coupled to kinetic Alfvén waves. Consequently, the GAE can be heavily damped by the electron Landau damping and become no longer destabilized by the alpha particles. Thus, one effect of toroidicity is to stabilize the GAE modes, which in cylindrical geometry would be unstable in the presence of alpha particles. On the other hand, the TAGE mode is inherently a toroidicity-induced global mode, and it suffers little Landau resonant damping under well defined conditions. Furthermore the TAGE mode has a substantially longer parallel wavelength compared to that of the GAE mode and is therefore more easily destabilized by the alpha particles.

Our principal results are the following:

1. A toroidal Alfvén wave eigenmode equation was derived that includes the alpha particle response and was numerically solved for the GAE modes. Full toroidicity effects were incorporated in the plasma fluid response and in the wave propagation operator. We found that toroidal coupling can stabilize the GAE modes in the presence of alpha particles, as long as the mode frequency is embedded in the sideband continuum.

2. A model eigenmode equation for the TAGE mode was derived

with the use of an $(A_{\|}, \varphi)$ description for the perturbed fields (in the low beta, incompressible limit) and with the inclusion of FLR effects, parallel electron dynamics, and the kinetic alpha response. In the MHD limit, the eigen-equation was analytically solved by means of a two-scale method. Furthermore, numerically we found that the global structure is only slightly changed by FLR effects, and consequently electron Landau damping is negligibly small for this mode.

3. Destabilization of the TAGE mode by resonant alpha particles was studied perturbatively. We found that the growth rate of the TAGE mode is about three times larger than that of the cylindrical GAE over a wide range of values for the alpha particle density scale length, which is a measure of the source of free energy.

These results were applied to the proposed Compact Ignition Tokamak, where it appears that the stability of these global-type Alfvén modes— especially the toroidal gap eigenmodes— will be a serious issue.

Chapter 2

Effects of Ballooning Instability on Tokamak Confinement

2.1 Introduction

Recently, Connor, Taylor, and Turner [13] have proposed a simple ballooning mode transport model to explain the observed deterioration of confinement in tokamaks with auxiliary heating. In this model, the thermal conductivity is taken to have the form established for low-beta ohmic discharges wherever the plasma is theoretically stable with respect to ideal MHD ballooning modes. In regions where the plasma is locally unstable to ballooning, the conductivity is considered to be so large that the pressure profile adjusts itself to remain marginally stable. Although quite simple, this model is able to account for a soft beta limit and a gradual degradation of confinement with input power. The significance of this model is that it provides a self-consistent description of profile evolution that incorporates both stability and transport, in contrast to the usual procedure of obtaining an optimized equilibrium profile that is marginally stable at every point.

More recently, this model has been extended by Freidberg et al. [40,41] to include ohmic, as well as auxiliary, heating effects and to include a phenomenological sawtooth energy convection term to keep the safety factor on axis near unity. Also, they obtained an inverse power scaling for the confinement time in the limit of ultimately large values for the auxiliary heating power.

In an earlier development, Carreras, Diamond, et al. [17] had proposed that resistive ballooning turbulence is responsible for confinement deterioration in auxiliary heated tokamaks. Their theoretically derived anomalous thermal conductivity agreed quite well with measurements reported for the ISX-B experiment. On the other hand, the energy confinement scaling due to ideal ballooning, as obtained by means of the Connor-Taylor-Turner (CTT) treatment, also seems to agree with experimental results.

Here, we propose a method to calculate the anomalous thermal conductivity induced by ideal ballooning instability, based on the CTT model. A comparison of this result with experiment and with the Carreras-Diamond result indicates that the conductivity derived on the basis of the CTT model is in good agreement, but only when a preponderance of the plasma volume is ideally unstable.

Also, we will demonstrate how the CTT model can be improved for high beta plasmas. The original CTT treatment used a ballooning first stability boundary that is based on a low beta equilibrium model and, hence, is not self-consistent for scaling studies. Here we adopt a high beta equilibrium model developed by Choe and Freidberg [42] and show how the transport scaling is modified.

Although the CTT theory was focused on auxiliary-heated tokamaks, one may ask whether a similar deterioration occurs for high beta, purely ohmically heated tokamaks. The confinement time of a low beta, ohmically-heated tokamak has been found to be well described by the "benchmark" scaling law $\tau \propto n$, where τ is the energy confinement time and n is the plasma density [43]. However, if a tokamak can be ohmically heated to sufficiently high beta values, then ballooning instability may set in, and it is interesting to examine

the confinement scaling for this case. Moreover, such a treatment is appealing because of its self-consistent heating profile. Our result, however, indicates that this regime is beyond the operating range of present-day ohmically heated tokamaks.

Finally, we will employ the CTT model to investigate access to the so-called second stability regime [9,10,11] of high beta ballooning modes. Several mechanisms, such as finite Larmor radius effects [44,45], pressure anisotropy [46,47], bean-shaped flux surfaces [6,7], and the introduction of highly energetic trapped particles [3], can significantly enhance tokamak stability. However, it is not clear whether the plasma can actually pass into the second stability regime self-consistently. Our assessment of this question shows that such access is possible, but only at rather high heating power.

The remainder of the chapter is organized in the following manner. In Sec. 2.2, we review the CTT ballooning mode transport model, with particular attention to the behavior of the plasma profile evolution at large values for the heating power. In Sec. 2.3, we calculate the anomalous thermal conductivity based on this model and compare it with experiment. In Sec. 2.4, we obtain a modified CTT confinement scaling by using a high beta tokamak equilibrium model. In Sec. 2.5, we consider the degradation in confinement for a high beta, ohmically-heated tokamak without auxiliary heating. In Sec. 2.6 we investigate the question of accessibility to second stability. Finally, Sec. 2.7 summarizes our conclusions.

2.2 Profile Evolution at Large Heating Power

First, let us briefly review the ballooning mode transport model developed by Connor, Taylor, and Turner [13]. In their treatment, the plasma

is divided into three zones: a sawtooth zone inside the $q = 1$ surface where q is the usual safety factor, a transport zone, and a ballooning zone where the plasma would be linearly unstable. For the sake of simplicity, here we will neglect the sawtooth effects.

Then, in the transport zone, the pressure profile is determined by the thermal conduction equation,

$$\frac{1}{x}\frac{d}{dx}\left[x\frac{d\tilde{p}(x)}{dx}\right] + \frac{1}{\lambda}h(x) = 0, \tag{2.1}$$

and the poloidal magnetic field is determined by Ampere's equation and Ohm's law,

$$\frac{1}{x}\frac{d}{dx}[xb(x)] = \tilde{p}^{3/2}(x)\left[\int_0^1 dx\ x\ \tilde{p}^{3/2}(x)\right]^{-1}. \tag{2.2}$$

Equations (2.1) and (2.2) are written in the large-aspect-ratio cylindrical approximation with dimensionless variables: $x = r/a$ is the minor radius normalized to the plasma radius a; $\tilde{p}(x) = p(r)/p(0)$ is the normalized scalar plasma pressure; $b(x) = B_\theta(r)/B_\theta(a)$ is the normalized poloidal magnetic field; $h(x)$ is related to the heating power density, normalized so that $\int_0^1 h(x)xdx = 1$; and λ plays the role of an eigenvalue that is adjusted to satisfy the boundary condition that the pressure vanish at the edge of the plasma, $\tilde{p}(1) = 0$. Specifically, the parameter λ is related to the energy confinement time, τ, by the relationship

$$\lambda = c(\tau/\tau_I)\left[\int_0^1 dx\ x\ \tilde{p}^{3/2}\right]^{-1} \tag{2.3}$$

where $c = \left[1 - \int_0^1 h(x)x^3dx\right]\Big/4$ is related to the heating profile and $\tau_I = 3ca^2/2\chi_I$ is the INTOR confinement time which is associated with the thermal conductivity $\chi_I(m^2/\sec) = 5\times10^{19}n^{-1}(m^{-3})$ for ohmic discharges without ballooning instabilities. For simplicity, a model in which the density is independent of radius is assumed.

In the ballooning zone, the pressure gradient is determined by the condition for ideal MHD ballooning stability,

$$\alpha \equiv -\frac{A\lambda x^2}{b^2(x)}\frac{d\tilde{p}}{dx} = f(S). \tag{2.4}$$

Here α is essentially the local poloidal beta value multiplied by the inverse aspect ratio: $\alpha = -(2\mu_0 R q^2/B_T^2)(dp/dr)$ in unnormalized form ($\mu_0 = 4\pi \times 10^{-7}$), with R the major radius and B_T the toroidal field. The parameter A is directly proportional to the total input power P:

$$A = 4Pa\tau_I/3cI_p^2R^2\mu_0 = 3.2 \times 10^{-20}\,\frac{P(MW)a^3(m)n(m^{-3})}{I_p^2(MA)R^2(m)}, \tag{2.5}$$

where $I_p = 2\pi a B_\theta(a)/\mu_0$ is the plasma current. The right-hand side of Eq. (2.4), $f(S)$, represents the marginal first stability boundary, which is a function only of the shear $S = b\ d(x/b)/dx$. In the ballooning zone, the poloidal field $b(x)$ is still determined by Eq. (2.2).

The transport zone extends from $x = 0$ to $x = x_0$, where x_0 is the marginal stability point at which the solutions for $\tilde{p}(x)$ and $b(x)$ in this zone first satisfy $\alpha(x_0) = f(S)$. The ballooning zone then extends from $x = x_0$ to $x = 1$. The boundary conditions are that $d\tilde{p}/dx = 0$ at $x = 0$ and $\tilde{p} = 0$ at $x = 1$. Note that $b = 0$ at $x = 0$ and $b = 1$ at $x = 1$, by definition. For a fixed value of the parameter A, the system of Eqs. (2.1), (2.2) and (2.4) then constitutes an eigenvalue problem with λ as the eigenvalue and $\tilde{p}$ and b as the eigenfunctions. (Note that our neglect of sawtooth effects eliminates $q(a)$ as a parameter.)

We propose to solve this coupled set of eigen-equations by means of a two-eigenvalue shooting method. That is to say, in addition to the eigenvalue λ, we introduce the quantity $\kappa = \int_0^1 x\tilde{p}^{3/2}dx$ as another eigenvalue. Both λ and

κ are to be determined for a given value of A, as follows. For arbitrary λ and κ, we obtain $\tilde{p}(x)$ and $b(x)$ in the stable region by integrating Eqs. (2.1) and (2.2) in parallel from $x = 0$ up to $x = x_0$ and subsequently in the unstable region by integrating Eqs. (2.2) and (2.4) from $x = x_0$ up to $x = 1$. In general, the resulting profiles will not satisfy $p = 0$ and $b = 1$ at the plasma edge. Therefore, we use a shooting method with two loops. In the outer loop, we choose a value for λ; in the inner loop we vary κ until the condition $b(1) = 1$ is satisfied; then the value for λ is changed, and the inner loop is repeated. By means of the outer loop adjustments to λ, we are able to search for a profile that satisfies $\tilde{p}(1) = 0$. Ultimately, of course, the results from this two-eigenvalue scheme will be equivalent to those obtained by iterating on the profiles [13].

The effect of various heating profiles was examined by Connor et al. [13], who found that the saturated beta values are relatively independent of the heating profile. In this work, therefore, we will for convenience assume uniform heat deposition and adopt a constant profile for the heating power density: $h(x) = 2$. We then note that Eqs. (2.1) and (2.2) in the stable transport region can immediately be integrated to give

$$\tilde{p}(x) = 1 - x^2/2\lambda \quad \text{for} \quad 0 \leq x \leq x_0 \tag{2.6}$$

and

$$b(x) = \left(\frac{2\lambda}{5\kappa x}\right)\left[1 - \left(1 - \frac{x^2}{2\lambda}\right)^{5/2}\right] \quad \text{for} \quad 0 \leq x \leq x_0. \tag{2.7}$$

Also note that $c = 1/8$ in this case. Following the two-eigenvalue shooting procedure previously described, we then only need to use numerical integration for Eqs. (2.2) and (2.4) in the ballooning region, $x_0 \leq x \leq 1$, where we employ a fourth-order Runge-Kutta method.

As a result of doing so, we are able to reproduce the CTT result that for $A \geq 4.4$, the confinement scaling is well represented by $\tau \propto A^{-0.72}$. We find, moreover, that this scaling remains valid at very large heating powers, at least up to $A = 85.4$.

Figure 2.1 displays, for various values of A, the profile trajectories of the plasma, plotted as implicit functions of radius in the two-dimensional space of shear versus α, which is a measure of the local pressure gradient. That is to say, the minor radius increases along each trajectory away from the $S-\alpha$ origin, which corresponds to the magnetic axis $x = 0$. The point where the trajectory intersects the marginal stability curve corresponds to the point $x = x_0$ where the ballooning zone begins. As this intersection point drops down the marginal boundary curve, the size of the ballooning zone expands. Figure 2.1 clearly demonstrates that, as the value of A is increased, the unstable volume of the plasma at first expands rapidly for small A. However, at larger A, this rate of expansion slows down, until at $A \cong 80$, it expands very little. It is precisely due to this feature of the self-consistent evolutionary behavior that the validity of the CTT scaling law survives even at very large heating powers. Consequently, this result indicates that it is nearly impossible to have an inverse power scaling, $\tau \propto A^{-1}$, as has been suggested in Ref. 41. Such an inverse scaling derives directly from Eq. 2.4 if one were to assume that the entire plasma volume is ballooning marginally unstable. However, the boundary condition $d\tilde{p}/dx \rightarrow 0$ at $x = 0$ tends to prevent this situation for all but unreasonably large heating powers.

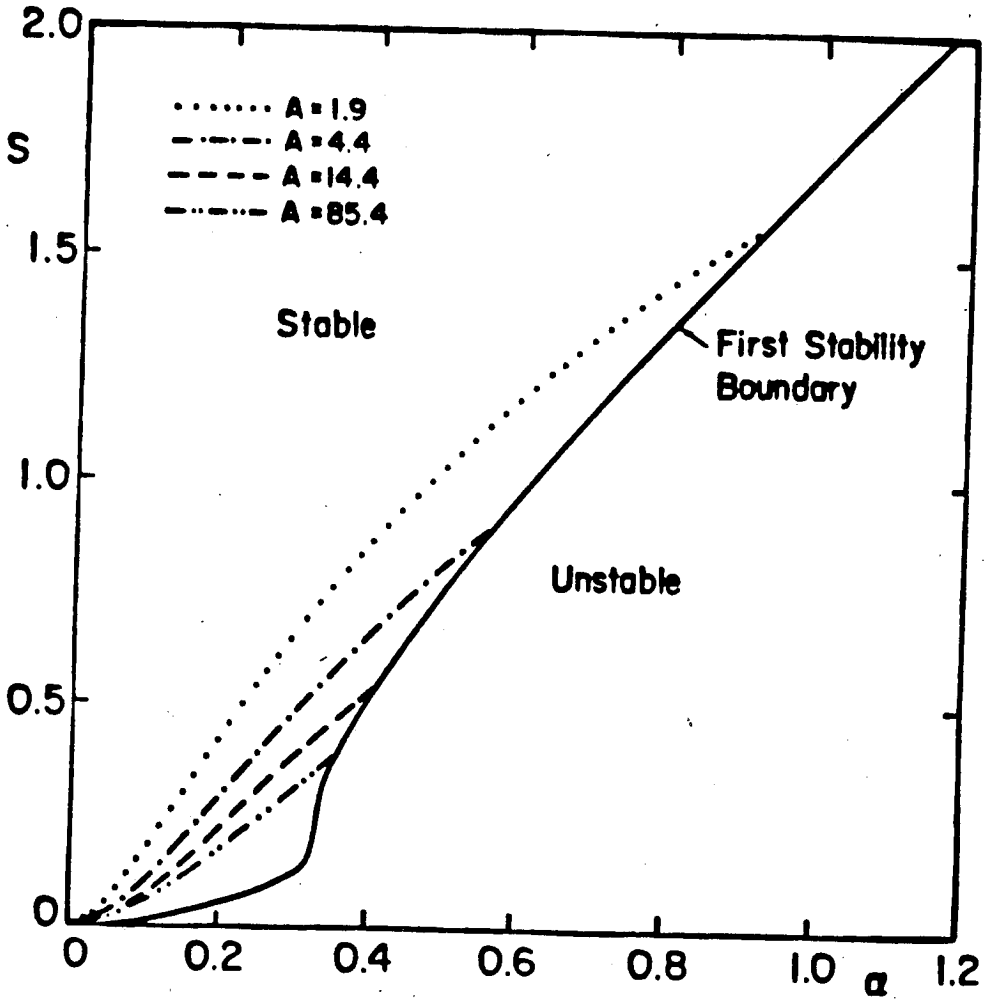

Figure 2.1: Plasma profiles of shear versus pressure gradient, for increasing values of the heating power.

2.3 Anomalous Thermal Conductivity Induced by Ideal Ballooning Instability

We now propose to employ the CTT model in order to calculate the anomalous thermal conductivity that would be induced by ideal MHD ballooning modes. Assuming that the thermal conductivity $\chi(r)$ is continuous over the entire plasma volume, we can write down the transport equation for all radii:

$$\frac{1}{x}\frac{d}{dx}\left(\frac{\chi(x)}{\chi_I}x\frac{d\tilde{p}}{dx}\right)+\frac{1}{\lambda}\,h(x)=0. \tag{2.8}$$

In the ballooning-stable transport region, we have $\chi=\chi_I$ by assumption, and the $\tilde{p}$ and b profiles can be obtained. In the ballooning-unstable regions, we do not *a priori* know the form of χ. Hence, in the style of the CTT approach, we rely on the first stability condition, Eq. (2.4), to obtain the profiles in that region. For given A, then, eventually one obtains $\lambda(A)$, $\tilde{p}(x,A)$, and $b(x,A)$.

On the other hand, once the profiles are known, we can return to the transport equation, Eq. (2.8), and integrate it *a posteriori* to obtain the thermal conductivity also in the unstable region. Thus, we have

$$\frac{\chi(x,A)}{\chi_I}=-\frac{\int_0^x xh(x)dx}{\lambda(A)x\partial\tilde{p}(x,A)/\partial x}, \tag{2.9}$$

with λ and $\tilde{p}$ now as known quantities.

Figures 2.2 and 2.3 display the results of calculating the anomalous thermal conductivity in this way for the parameter values $a=0.27$ m, $R=0.93$ m, and $n=7\times10^{19}$ m^{-3} corresponding to two typical high-poloidal-beta discharges in the ISX-B tokamak (Carreras et al. [17]). For the case shown in Fig. 2.2, the beam power and plasma current were measured to be $P_b=2$ MW and $I_p=83$ kA, respectively. Through Eq. (2.3), these values correspond to $A=14.8$. Figure 2.2 shows that our result for χ coincides with that calculated

by Carreras and Diamond (1983) on the basis of resistive ballooning turbulence and also agrees fairly well with the experimental conductivity over the effective confinement region ($1 < q < 2$).

The case shown in Fig. 2.3 had $P_b = 0.6$ MW and $I_p = 143$ kA, corresponding to $A = 1.5$. Our calculated χ agrees with neither the Carreras-Diamond result nor the experimental result. The reason for the discrepancy is that the case of Fig. 2.3 had a relatively low beta value: the volume-averaged poloidal beta was $\beta_p = 0.85$. Hence the ideally unstable volume of the plasma is small, and resistive ballooning, dominates the transport.

Nevertheless, in the case corresponding to Fig. 2.2, the beta value is relatively high ($\beta_p = 1.7$), so that the effect of the ideal ballooning modes is prevalent, because a large portion of plasma volume is ideally unstable. Then the thermal conductivity induced by ideal ballooning modes can represent the experimental results about as well as does the Carreras-Diamond result.

2.4 Modified Confinement Scaling for Finite Beta

The original CTT theory was based on a low-beta tokamak equilibrium model. In this section we consider how the theory can be improved for high beta plasmas.

Recently, a high beta equilibrium for tokamaks has been proposed by Choe and Freidberg [42], in which the flux surfaces are assumed to be circular but have a finite Shafranov shift due to the plasma beta. According to their model, the previous low-beta first stability boundary $\alpha = f(S)$ of Eq. (2.4) is modified to become $\alpha = f(S, \delta)$, where the quantity δ is given by

$$\delta(x) = \frac{3^{3/2}}{2xb^2(x)} \int_0^x dx' b^2(x')\alpha(x'). \tag{2.10}$$

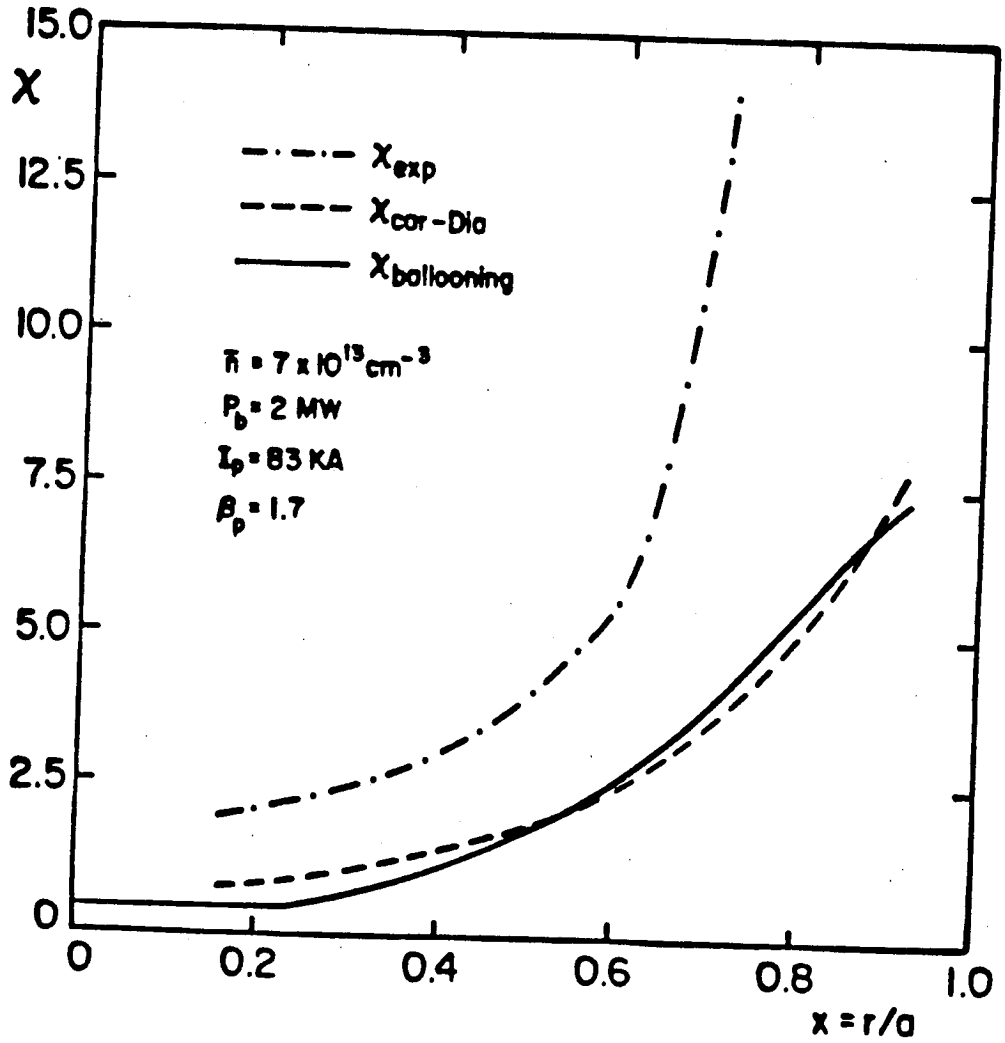

Figure 2.2: High-beta radial profiles of the thermal conductivities for the ISX-B experiment, for the Carreras-Diamond theory, and for the ideal ballooning mode.

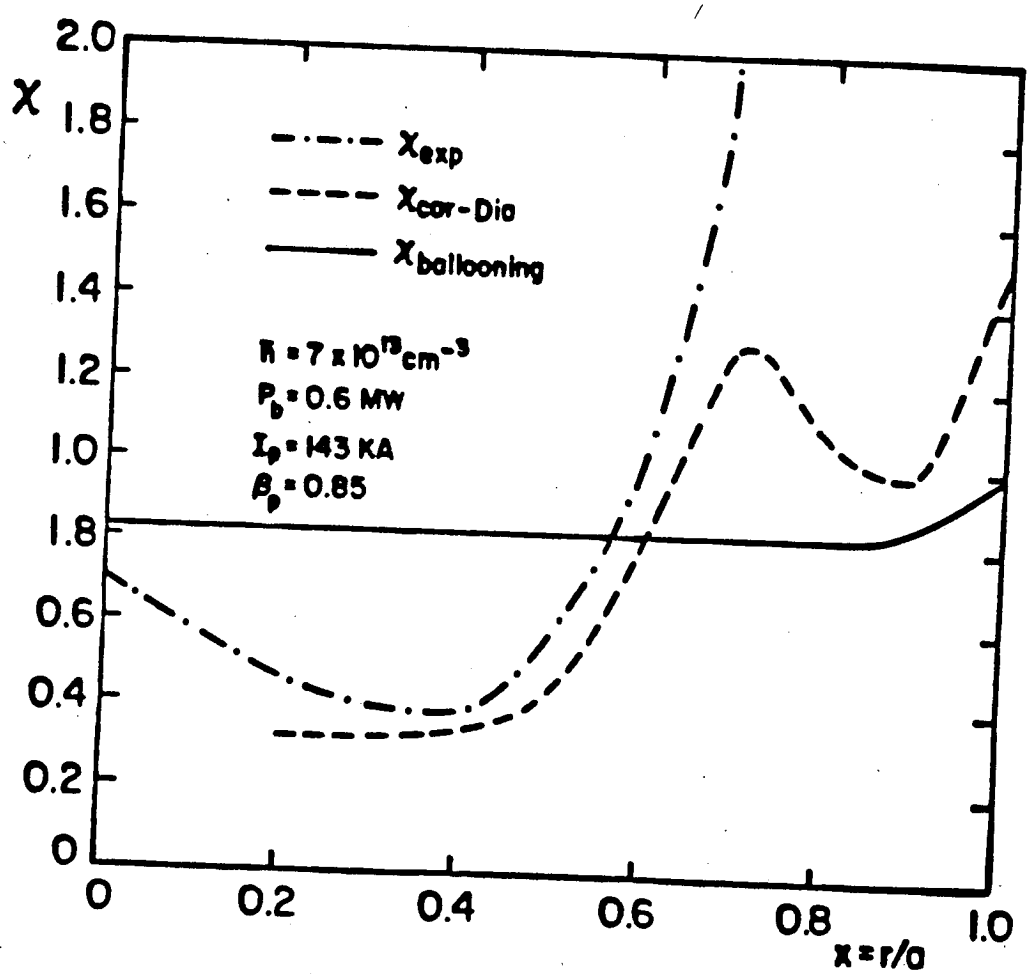

Figure 2.3: Low-beta radial profiles of the thermal conductivities for the ISX-B experiment, for the Carreras-Diamond theory, and for the ideal ballooning mode.

From the plots of $f(S,\delta)$ given in Choe and Freidberg (1986) for certain fixed values of δ, we note that, to a fair approximation,

$$f(S,\delta) \approx f(S) + \delta/4, \tag{2.11}$$

which provides us with $f(S,\delta)$ as a continuous function of δ. This expression in Eq. (2.11) holds when $S \geq 0.5$ (i.e., A not too large) and also $S \geq \alpha$.

Using this high-beta equilibrium and the same method as before, we obtain a modified CTT scaling law,

$$\tau \propto A^{-0.62}, \tag{2.12}$$

which is shown in Fig. 2.4, in comparison to the low-beta CTT scaling of $\tau \propto A^{-0.72}$. With the high-beta equilibrium, confinement is therefore improved. This result is clearly related to the stabilizing effect of the Shafranov shift for finite beta.

2.5 Confinement Scaling for Ohmically Heated, High Beta Plasma

The energy confinement time for a low beta, ohmically heated tokamak generally increases linearly with the density, the so-called INTOR scaling [43]. The CTT model [13] derived the confinement scaling for a high-beta, purely auxiliary-heated tokamak, and a hybrid treatment of ohmic effects combined with auxiliary heating has been given by Freidberg et al. [41]. We now consider how confinement may be degraded by ideal ballooning modes in a high-beta, purely ohmically-heated tokamak plasma.

With the assumption of pure ohmic heating, the heating density profile can be treated self-consistently as

$$H(r) = E_z J_z = E_z^2/\eta \propto p^{3/2}(r), \tag{2.13}$$

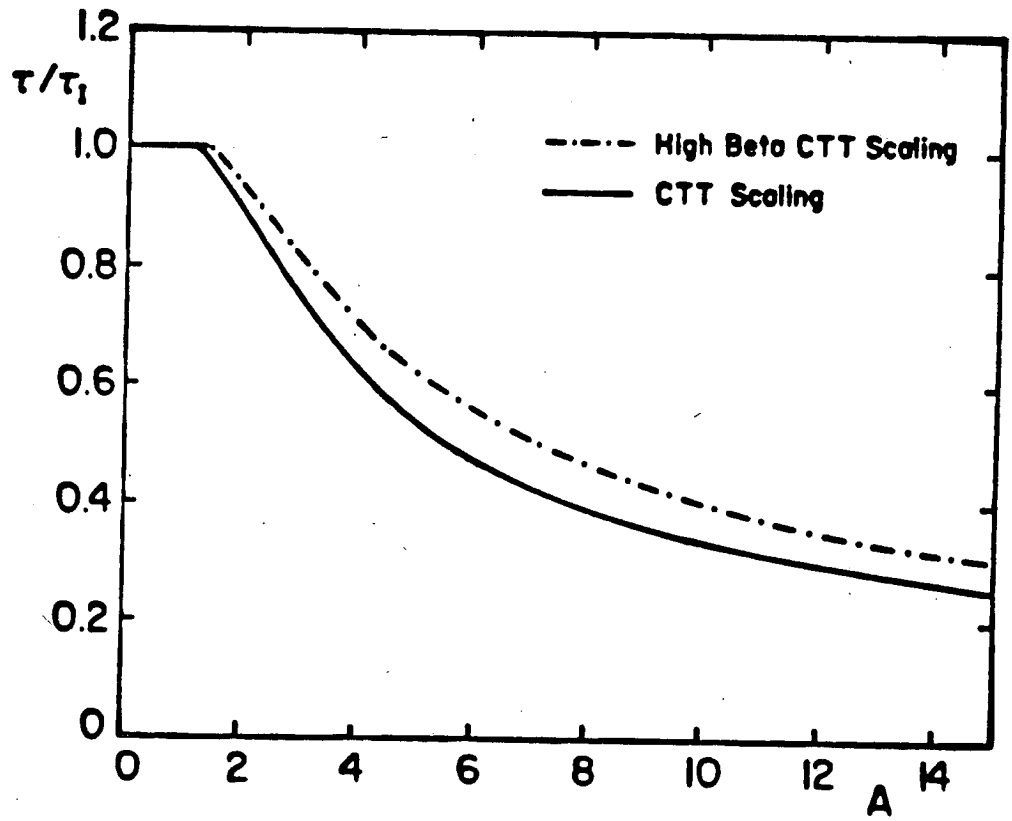

Figure 2.4: Dependence of the confinement time on input power, for a high-beta model tokamak equilibrium.

in contrast to the auxiliary heating case of Sec. 2.2 where the heating power profile is independent of the plasma profile. In Eq. (2.13), we use Spitzer resistivity [48], which for a hydrogen plasma is given by

$$\eta(\text{ohm} - \text{m}) = 5.22 \times^{-5} Z\ \ell n\Lambda / T_e^{3/2}(e\text{V}). \tag{2.14}$$

Using $p = 2nT$, we write

$$\eta = \eta_0 [n/p(0)]^{3/2} \tilde{p}^{-3/2}(x),$$

where $\eta_0 = 9.75 \times 10^{-33} Z \ln \Lambda$ is a constant and we continue to assume uniform density, as in Connor et al. [13]. The normalized heating density in dimensionless units, as in Eq. (2.1), is given by

$$h(x) = \frac{4\pi^2 R a^2 H(r)}{P} = \frac{\tilde{p}^{3/2}(x)}{\int_0^1 dx\ x\ \tilde{p}^{3/2}(x)}. \tag{2.15}$$

Note that the ohmic heating input power, $P = \int d^3 r \sigma E_z^2$, can be written as

$$P = 2\pi R I_p E_z, \tag{2.16}$$

if we use Eq. (2.2) to relate the current I_p to the electric field E_z and the quantity $\kappa = \int_0^1 dx\ x\ \tilde{p}^{3/2}$:

$$I_p = \frac{2\pi a}{\mu_0} B_\theta(a) = 2\pi a^2 \int_0^1 dx\ x\ \sigma E_z = 2\pi a^2 [p(0)/n]^{3/2} E_z \kappa / \eta_0. \tag{2.17}$$

As in Sec. 2.2, we solve self-consistently for the plasma pressure and poloidal field profiles in the ballooning stable and unstable zones, again neglecting sawtooth effects. In the ballooning-stable transport zone, $0 \leq x \leq x_0$, the determining equations are again Eqs. (2.1) and (2.2), here rewritten in view of Eq. (2.15) as

$$\frac{1}{x} \frac{d}{dx} \left(x \frac{d\tilde{p}}{dx} \right) + \frac{\tilde{p}^{3/2}(x)}{\lambda \kappa} = 0 \tag{2.18}$$

$$\frac{1}{x} \frac{d}{dx}(xb) = \frac{\tilde{p}^{3/2}(x)}{\kappa}. \tag{2.19}$$

The eigenvalue $\lambda = 4\pi^2 Rp(0)\chi_I/P$ is still given by Eq. (2.3), which can be written as $\lambda\kappa = c(\tau/\tau_I)$, with the constant c defined as before but with the $h(x)$ of Eq. (2.15). In the marginally unstable zone, $x_0 \leq x \leq 1$, the pressure gradient is determined by the ideal stability condition of Eq. (2.4), in conjunction with Eq. (2.19) for the field. However, we rewrite Eq. (2.4) in terms of a scaling parameter A' that involves neither $p(0)$ nor E_z, since for ohmic heating we desire a confinement scaling that depends on n, I_p, and R. This objective is satisfied by rewriting Eq. (2.4) in the form

$$-A'(\lambda/\kappa)^{2/5}\,\frac{x^2}{b^2}\,\frac{d\tilde{p}}{dx} = f(S), \tag{2.20}$$

with the scaling parameter given by

$$A' = 5.52 \times 10^{-21} n(m^{-3}) a^{2.2}(m) R^{-1}(m) I_p^{-1.2}(MA). \tag{2.21}$$

The results of solving the system of Eqs. (2.18)–(2.20),, again by a two-eigenvalue method, are shown in Fig. 2.5. For $A' > 1$, we obtain the confinement $\tau/\tau_I \propto A'^{-0.44}$, or

$$\tau \propto a^{1.03} n^{0.56} R^{0.44} I_p^{0.53}. \tag{2.22}$$

It is interesting to see whether the saturation point ($A' \approx 1$) is relevant to contemporary ohmically heated tokamaks. For example, Alcator C ($a = 0.165$ m, $R = 0.64$ m, $I_p = 0.5$ MA) is an ohmically heated tokamak with fairly high densities. The point where $A' = 1$ then corresponds to a critical density of $n_c \cong 2.7 \times 10^{21}$ m^{-3}, which is beyond the usual operating range of Alcator C. From this we conclude that confinement deterioration due to the ballooning instability has little effect in purely ohmically heated tokamaks.

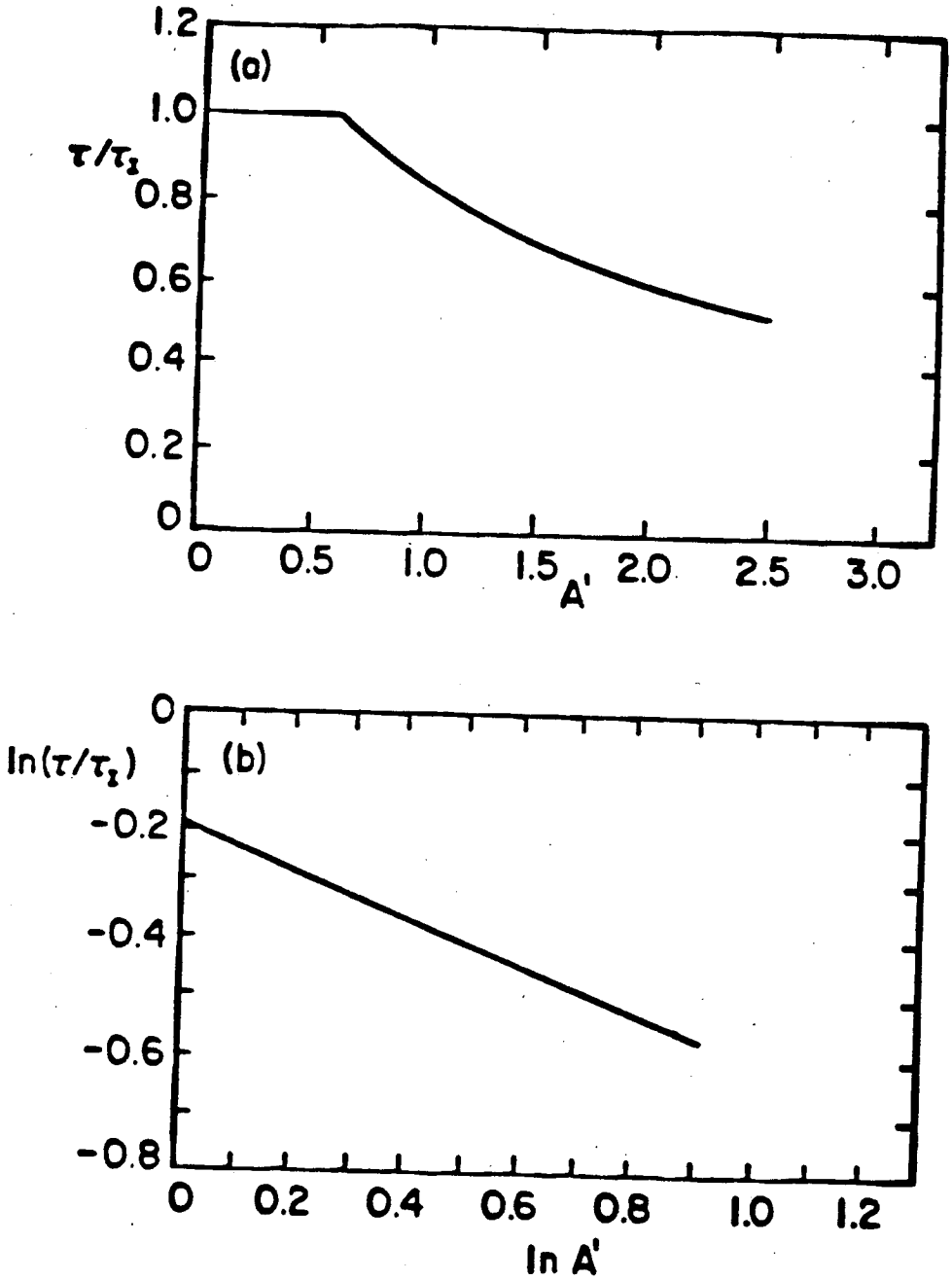

Figure 2.5: (a) Dependence of the confinement time on the input power parameter A' for a purely ohmically heated plasma. (b) Logarithmic dependence of the confinement time, for $A' \geq 1$.

2.6 Accessibility to Second Stability

The question of accessibility to the second stability regime for ballooning modes is rather subtle. In general, it is studied under the assumption of a given plasma profile. That is to say, one assumes profiles for, say, the normalized pressure $\beta = \beta_0\hat{\beta}(\psi)$ and the safety factor $q = q_0\hat{q}(\psi)$, solves the Grad-Shafranov equilibrium equation for the flux ψ, and determines the linear stability boundary in (β_0, q_0) parameter space. The claim, then, is that the plasma can access second stability along any path that does not intersect the unstable region. However, this type of approach has the intrinsic defect of not being self-consistent, since it assumes a certain profile. In this section, we propose to address the accessibility issue by means of the CTT method, which, although oversimplified, does allow for a self-consistent determination of the plasma profile.

Let us recall that in the ideal MHD theory of ballooning modes, accessibility is prevented by an unstable gap that separates the regions of first and second stability. (We do not consider the case where the plasma may be able to penetrate this gap by very rapid heating [49]. However, tokamak stability can be significantly enhanced by the introduction of certain supplemental stabilizing mechanisms. For example, the effects of finite gyroradius [44,45] and pressure anisotropy [46,47] can be taken into account, the plasma cross-section can be bean-shaped [6,7] or highly energetic trapped particles could be injected [3]. For each of these schemes, or possibly a combination thereof, with judicious choice of parameters, a direct avenue of accessibility can open up between the first and second stable regions.

2.6.1 Generic Model

For the sake of simplicity, we will here represent the enhanced marginal stability boundary in generic form as

$$\alpha_c = f'(S) = 1.2S \pm 0.6\sqrt{S^2 - S_m^2}. \tag{2.23}$$

Here the α of the toroidal core plasma is designated as α_c, in order to distinguish it, for example, from that for a hot particle component. Figure 2.6 displays the model marginal curves of Eq. (2.23), plotted for several values of the parameter S_m, which is a measure of the supplemental stabilization. For whatever provides the enhancement, the larger the value of S_m, the greater its stabilizing effect. For instance, the curve for $S_m = 0.5$ approximately models the FLR-stabilized boundary [45] for $k\rho_i = 0.4$; or, the curve for $S_m = 0.9$ is similar to the stability boundary for hot particles trapped with a half-width of $\pi/4$ on the outer side of a tokamak [3]. In our analysis, the parameter S_m will be considered to be constant. We caution that S_m is actually not a constant, but is related back to an equilibrium profile. For example, the stability boundary obtained by Rosenbluth et al. [3] was based on a very special distribution function such that α for the hot particles, α_h, is at each point chosen to have its maximum value as allowed by the condition of non-reversal of the magnetic curvature drift. Hence, the self-consistent determination of S_m is a fairly complicated matter and will be left for future study.

We now propose to use the CTT ballooning transport model described in Sec. 2.2, but with Eq. (2.23) in place of Eq. (2.4). The major difference is that now the ballooning stability boundary bifurcates as a function of the shear. There is a minimum value for the shear, S_m, below which ballooning modes are stable for all values of α_c. This feature allows the possibility of access to second

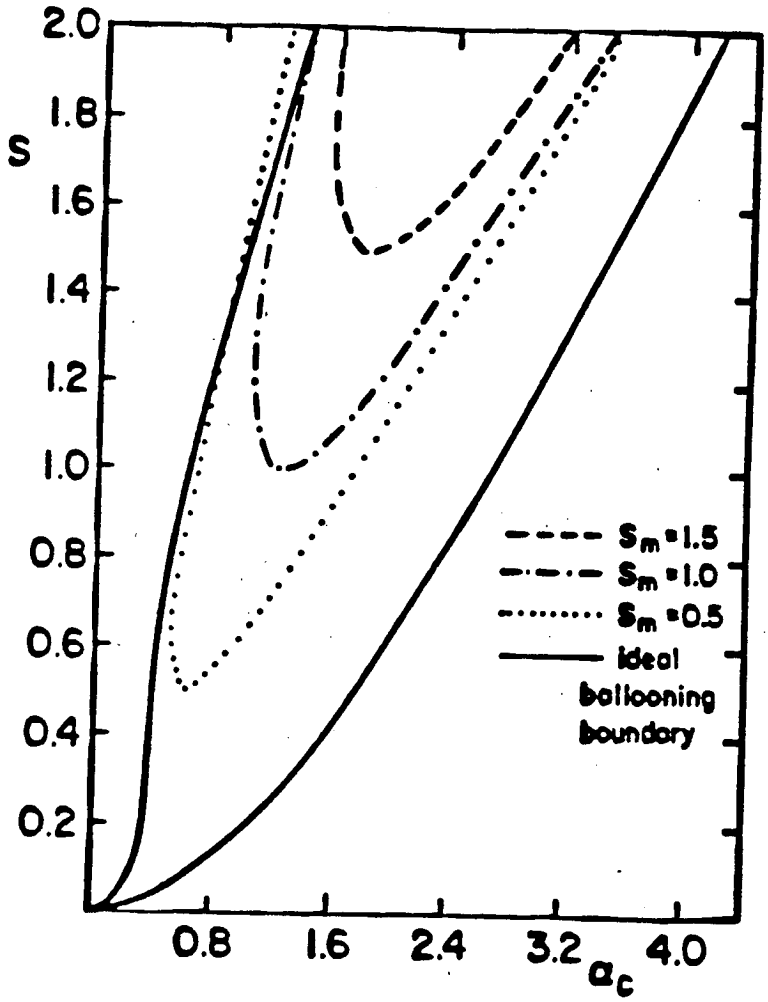

Figure 2.6: Model stability boundary for a tokamak with supplemental stabilization whose effectiveness is characterized by S_m.

stability. We wish to determine whether access can occur, by calculating the $S-\alpha_c$ profile evolution and the corresponding confinement time as the auxiliary heating power is adiabatically increased from zero to large values.

The numerical results for the case $S_m = 1.0$ are shown in Fig. 2.7. As the power (proportional to A) is increased, Fig. 2.7 shows that the point that divides the stable and unstable portions of the $S-\alpha_c$ trajectory and thus corresponds to $x = x_0$, moves down along the left side of the marginal stability boudary. This indicates that the unstable volume of the plasma expands. At the critical value $A_c \cong 21.0$, this point reaches the nadir of the stability curve, at $S = S_m$. If A is slightly increased beyond its critical value, there is no longer a solution in the first stability region, but a solution exists in the second stability region. The consequence is an abrupt change in the profile evolution and, correspondingly, a jump in the confinement time, which is shown in Fig. 2.8. Also shown is the situation where the power is reduced, beginning from large values. For very large P, the $S-\alpha_c$ trajectory does not know about the unstable gap since it passes completely under it, and therefore the confinement time settles down to INTOR scaling. As the power is reduced, the trajectory will partially lie along the right side of the stability boundary, with the lower endpoint of this segment at some $S > S_m$. Note that the confinement time is slightly enhanced above INTOR confinement. This enhanced confinement may be understood as follows: Recall that the energy confinement time is related to the pressure gradient and the applied power by $\tau \propto \int_0^a p(r)rdr/P = \int_0^a (-dp/dr)r^2dr/2P$. Then, as the power is reduced, since the magnitude of the pressure gradient cannot decrease below the second marginal stability limit, the confinement may be slightly better than INTOR. (This is exactly the opposite of what occurs when the power is raised, beginning from low values, in the first

stability regime.) When the power is further reduced, the trajectory reverts abruptly to first stability, thus yielding a hysteresis behavior for confinement.

A comparison of the confinement time scalings for various values of S_m is presented in Fig. 2.9. The critical power to access second stability from below is given by $A_c \cong 11.5$ for $S_m = 1.3$ and $A_c \cong 21$ for $S_m = 1.0$. The value of A_c obviously has a strong dependence on S_m. Since in practice, as was mentioned previously, the parameter S_m may assure values from approximately 0.5 to 0.9, rather high power would be required for accessibility. This result is seen to be consistent with the statement in Sec. 2.2 that the CTT scaling remains valid at moderately large heating powers.

2.6.2 Realistic Model

Here we note that the average magnetic well of a tokamak is well known to be stabilizing against low-beta weakly-ballooning instabilities on rational surfaces for which the value of the safety factor is larger than unity [50,51]. A necessary stability condition that incorporates both the effects of the mean magnetic well and the self-stabilization has been obtained by Mikhailovskii et al. [52,53] as following:

$$\frac{S^2}{2} + \alpha\epsilon(1 - \frac{1}{q^2}) - \frac{1}{2}S\alpha^2 + \frac{13}{128}\alpha^4 = 0 \tag{2.24}$$

where $\epsilon = r/R$ is the inverse aspect ratio. The first term reprents shear stabilization, the second term is the average magnetic well, the third term arises from pressure-gradient-driven destabilization, and the fourth term represents self-stabilization at finite beta. We see that Eq. (2.24) can be written as:

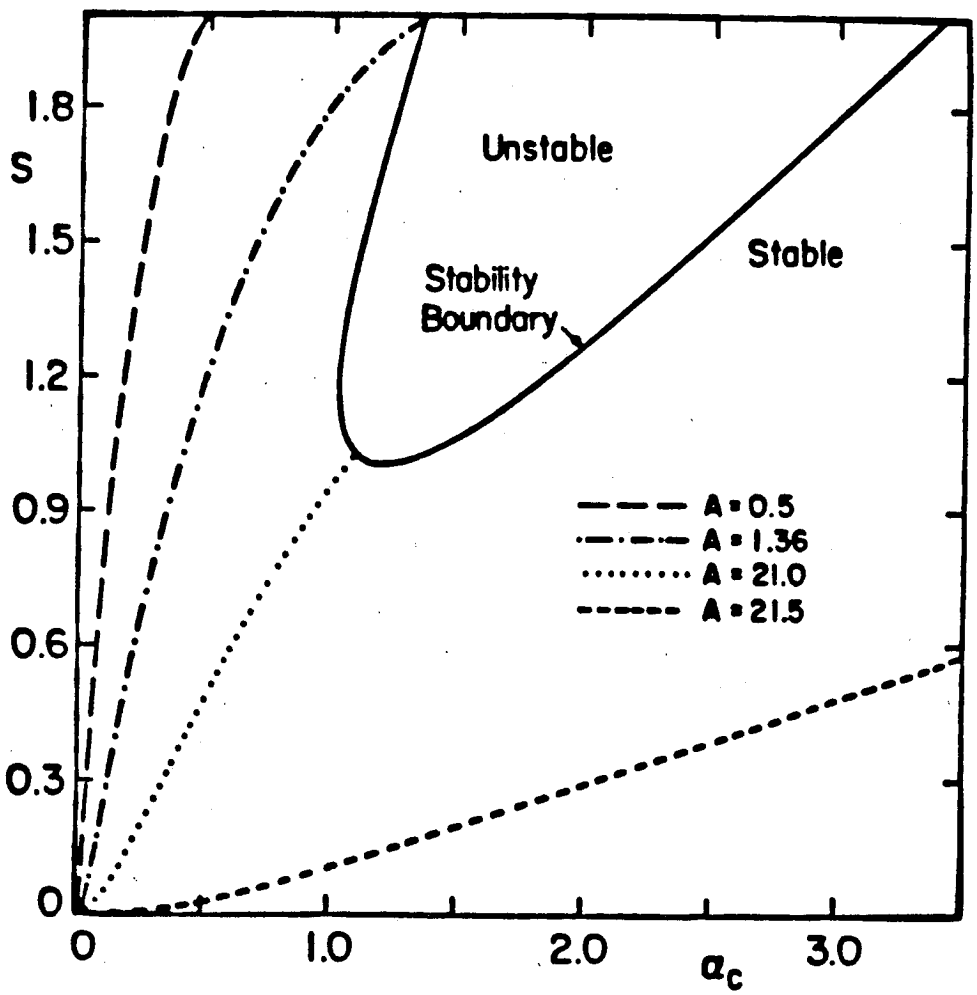

Figure 2.7: Plasma profiles of shear versus pressure gradient, for increasing values of the input power, with the model stability boundary ($S_m = 1.0$).

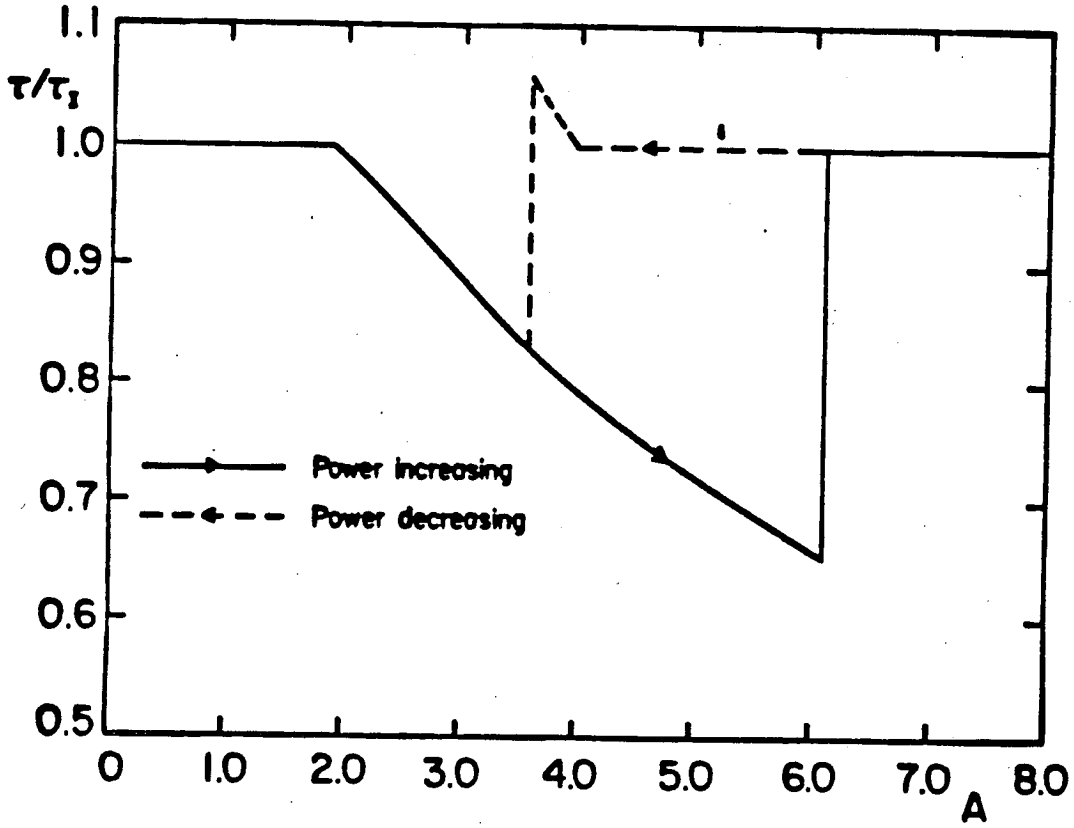

Figure 2.8: Hysteresis dependence of the confinement time on input power, with the model stability boundary ($S_m = 1.5$).

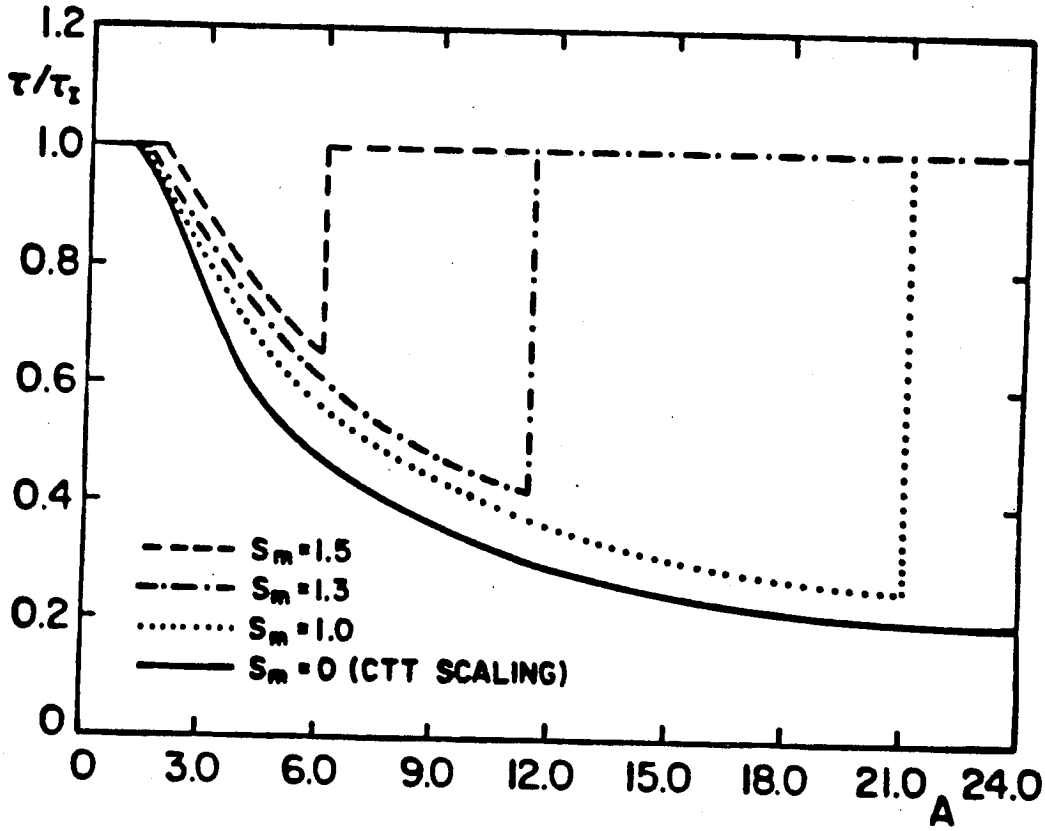

Figure 2.9: Comparison of the confinement time scaling with power for various values of S_m (increasing power only).

$$S(\alpha) = \frac{\alpha^2}{2} \pm \left[\frac{2}{64}\alpha^4 - 2\alpha\epsilon_*\right]^{1/2} \tag{2.25}$$

where we have defined $\epsilon_* = \epsilon(1 - q^{-2})$. There is no instability for $\alpha < \alpha_0 = 3.49\epsilon_*^{1/3}$, at which point $S = S_0 = 6.10\epsilon_*^{2/3}$, or for $S < S_m = 5.65\epsilon_*^{1/3}$, at which point $\alpha = \alpha_m = 3.64\epsilon_*^{1/3}$. For large α values, the stability boundary becomes parabolic $S \approx \frac{\alpha^2}{2}(1 \pm \sqrt{3}/4)$.[Note that Eqs.(4.4)-(4.6) of Ref. 52 contain minor typographical errors.]

The stability boundary of Eq. (2.24) has the features that it bifurcates as a function of the shear and that there is a minimum value of the shear, S_m, below which ballooning modes are stable for all α. Therefore, it qualitatively resembles the generic stability boundary considered in Sec. 3.5.1. Since we have considered the case for which $S_m = 1.0$ in the preceeding section, here we will take $\epsilon_* = \epsilon(1 - q^{-2}) = 0.074$. Strictly speaking, the stability boundary of Eq. (2.24) is valid in the low-beta, small-shear limit of a circular cross-section tokamak. In the present analysis, we transcend this limit for the sake of comparison at finite shear values.

With this ballooning-enhanced stability boundary due to average magnetic well and finite beta, we now proceed to reexamine the ballooning transport equation studied in the last section. Fig. 2.10 shows the steady-state $S - \alpha$ profile trajectory for several increasing values of the power parameter A. Fig. 2.11 shows the confinement time against A. For values of A greater than approximately 35, the $S - \alpha$ trajectory enters the second stability region without encountering ballooning instability. Accordingly the confinement time recovers the INTOR value. We observe that the qualitative features of these results are same as the results with a generic boundary in the last section.

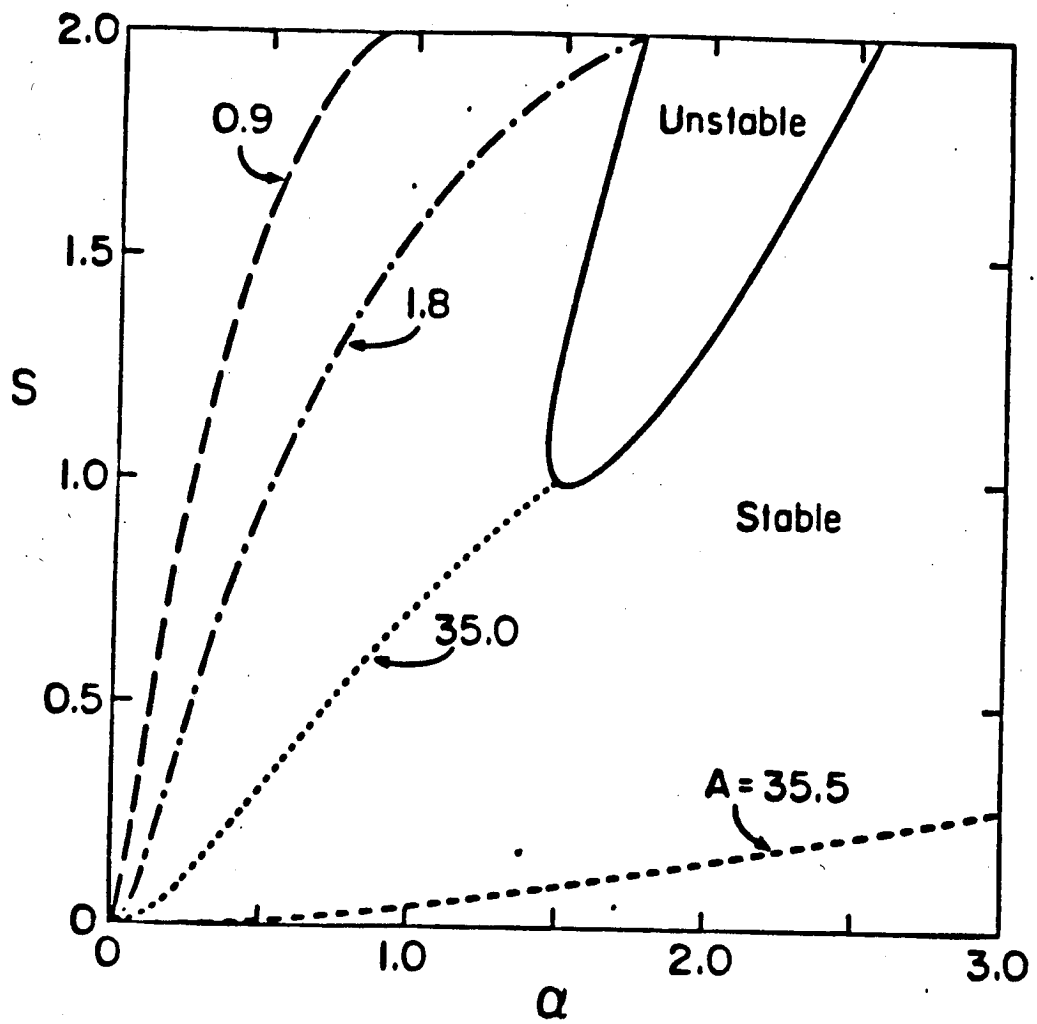

Figure 2.10: Plasma profiles of shear versus pressure gradient, for increasing values of input power A, with $\epsilon(1-q^{-2}) = 0.074$.

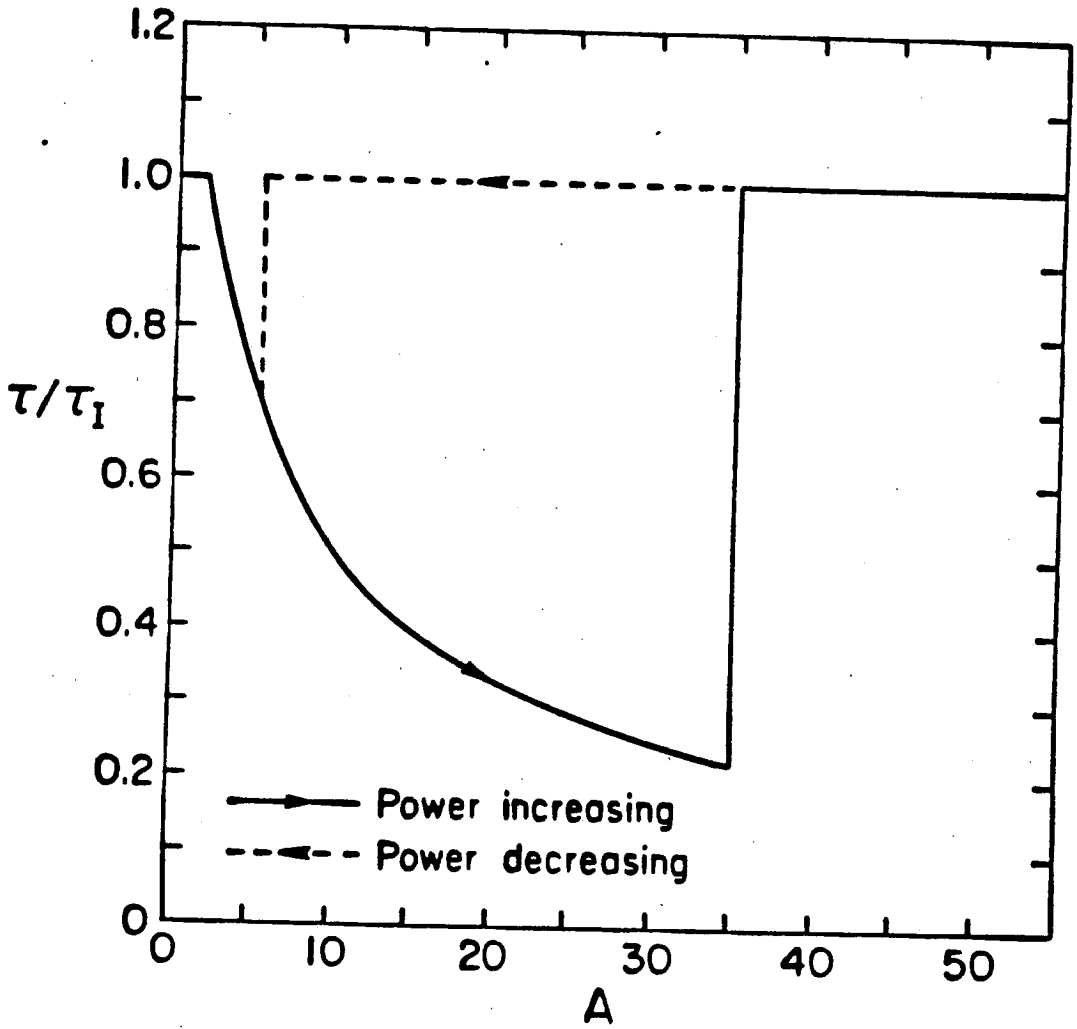

Figure 2.11: Hysteresis dependence of the confinement time on input power.

2.7 Summary

In this chapter, we have presented some extensions and applications of the ballooning transport model that was proposed by Connor et al. [13] to study the self-consistent profile evolution and confinement of an auxiliary-heated plasma. We find that the CTT confinement scaling $\tau \propto P^{-0.72}$ remains valid even for extremely large values of the heating power, so that the inverse linear scaling suggested by Freidberg et al. [41] seems improbable. It was shown that the anomalous thermal conductivity induced by ideal ballooning modes can be obtained in this model and that it compares well with both the experimental result and the theoretical result of Carreras and Diamond [17] at high beta, but not so well at low beta where the resistive modes are dominant. The simplicity of the CTT model, which is its strength, thus also restricts its validity. For high beta, it was also shown that use of a semi-analytic improved equilibrium [42] leads to a slightly improved prediction for the confinement time.

We also applied the CTT method to study confinement in a high beta, purely ohmically heated tokamak. The results indicate that confinement degradation would set in at rather high values. Therefore, ideal ballooning appears to have little influence on ohmic confinement.

Finally, we applied the method to study accessibility to the second stability regime for ballooning modes, whose stability is modeled by a generic stability boundary as well as a necessary stability condition that incorporates both the effects of the mean magnetic well and the self-stabilization. We find that rather large input power would be required. This treatment was not entirely self-consistent. However, it may indicate that experiments aimed at attaining second stability should consider a variety of schemes, including non-

adiabatic heating scenarios.

Chapter 3

Dynamic Transition to the Second Stability Regime

3.1 Introduction

It is well known that ballooning modes can limit the beta value attainable in a tokamak operating in the usual first stability parameter regime, but that the existence of the theorectically predicted second stability regime could allow for the possibility of high-beta operation. It has been shown that various methods– e.g., highly energetic particles [3], cross-sectional shaping [6,7], current profile control [8], etc.– can stabilize ballooning modes on individual flux surfaces for low value of the shear, thus providing a route by which to access the second stability regime.

In this chapter, we investigate the dynamical process by which a plasma confined in a tokamak can globally evolve twoard second stability under the application of auxiliary heating. We employ a simple one-dimensional time-dependent transport model, with a large but finite anomalous thermal conductivity coefficient induced by ideal ballooning instability, and numerically solve for the pressure profile, in the large aspect ratio limit. For a flux-conserving plasma, the problem of access to second stability can also be analytically recast in the form of a nonlinear laminar shock solution near the edge of the plasma. The numerical and analytical results predict a threshold heating power, as a function of the magnitude of the ballooning mode-enhanced transport, that is required for the plasma to attain a stable high-beta, steady-state profile.

The calculation in the present work follows, to some extent, from

the ideal MHD ballooning mode transport model that was proposed by Connor,Taylor, and Turner (hereafter referered to as CTT) [13] to explain the experimentally observed degradation of confinement in tokamak with auxiliary heating. In their model, the time-independent pressure profiles corresponding to various applied powers were obtained, subject to INTOR transport scaling in the ballooning stable regime and to virtually infinite transport in the unstable regime (i.e., the profile adjusts itself to remain marginally stable). In the preceeding chapter we employed a similar treatment to study tokamak confinement for the case of bifurcated marginal stability and found that globally second-stable equilibria can exist when the applied power exceeds a certain threshold. In this chapter the temporal evolution problem, with finite thermal transport in the unstable regime, is solved in order to show that the plasma can actually evolve self-consistently to a high-beta globally second-stable equilibrium with the application of sufficient power.

3.2 Theoretical Model

The evolution of the plasma profile will be described by the thermal transport equation:

$$\frac{3}{2}\frac{\partial p}{\partial t} = \frac{1}{r}\frac{\partial}{\partial r}(r\chi\frac{\partial}{\partial r}p) + h \tag{3.1}$$

Here, equal ion and electron temperatures, a constant density profile, and large-aspect-ratio geometry are assumed. In Eq. (3.1), $p(r,t)$ is the plasma pressure, χ is the thermal conductivity, and h is the auxiliary power deposition density (also, for simplicity, assumed to be constant in radius). Normalizing the radial coodinate r to the minor radius a, the thermal conductivity χ to χ_0 (its value in the ballooning stable regime), the time t to $3a^2/2\chi_0$, and the pressure to $aB^2/(2\mu_0 R q_a^2)$, where R is the major radius , q_a is the safety factor at the edge,

and B is the toroidal magnetic field, we obtain following normalized transport equation:

$$\frac{3}{2}\frac{\partial \tilde{p}}{\partial \tau} = \frac{1}{x}\frac{\partial}{\partial x}(x\chi_n \frac{\partial}{\partial x}\tilde{p}) + H \tag{3.2}$$

with normalized radius x, conductivity χ_n, time τ, pressure $\tilde{p}$, and heating density H, where

$$H = \frac{64 P a \tau_E}{3\mu I_p^2 R^2} \tag{3.3}$$

Here P is the total heating power and τ_E is the confinement time in the stable regime, $\tau_E = 3ca^2/16\chi_0$.

Now we are ready to incorporate into the transport equation the anomalous transport induced by ballooning instability. Information about the stability of high-mode-number ideal ballooning mode is included through a specification of the marginal stability boundary in terms of the pressure gradient parameter $\alpha = -(2\mu_0 R q^2/B^2)\partial p/\partial r$ and the shear $S = (r/q)dq/dr$. The solid curves shown in Fig. 3.1 are the well-known first stability and second stability boundaries for the ideal ballooning mode. We will assume that the ballooning mode has some sort of supplemental stabilization at small values of the shear (e.g., provided by energetic particles, etc.). The improved stability boundary is shown schematically in Fig. 3.1 as a dotted curve. For simplicity we adopt the generic boundary proposed in Chap. 2:

$$\alpha_{1,2}(S) = c_1 S \pm c_2 \left(S^2 - S_m^2\right)^{1/2} \tag{3.4}$$

Note that the parameter S_m is a measure of the supplemental stabilization and that c_2 is related to the width of the unstable region. Furthermore, within the unstable region, the thermal conductivity is taken to be enhanced as follows:

$$\chi_n(\alpha, S) = 1 + \frac{4(\chi_{max} - 1)}{(\overline{\alpha}_2 - \overline{\alpha}_1)^2}\left[\alpha - \alpha_1(S)\right]\left[\alpha_2(S) - \alpha\right] \tag{3.5}$$

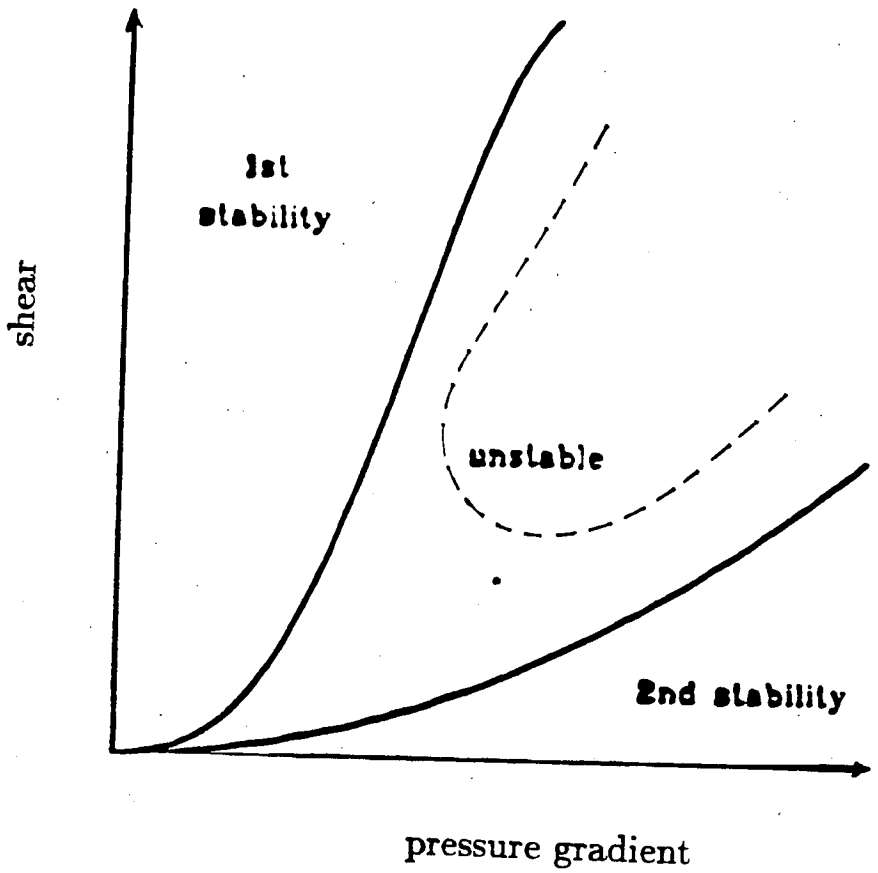

Figure 3.1: Ideal ballooning stability boundary of shear versus pressure gradient and the enhanced stability boundary (dotted line).

where $\bar{\alpha}_{1,2}$ are evaluated at the plasma edge and χ_{max} controls the degree of transport enhancement. Notice that near the second stability boundary $\alpha_2(S)$, the "effective" thermal conductivity $\chi_{eff} = \chi_n + \alpha(\partial\chi_n/\partial\alpha)$ will be negative since χ_n decreases with increasing pressure gradient α. Since χ_{eff} is the coefficient of the highest-order derivative term, this negative conductivity will cause numerical instability and will result in infinite steepening of the pressure gradient. To prevent this unphysical instability, we add a small ad hoc biharmonic term on the right-hand side of Eq. (3.2). The resultant equation is then given by

$$\frac{3}{2}\frac{\partial\tilde{p}}{\partial\tau} = \frac{1}{x}\frac{\partial}{\partial x}(x\chi_n\frac{\partial}{\partial x}\tilde{p}) + H - \lambda\frac{1}{x}\frac{\partial}{\partial x}x\frac{\partial^3}{\partial x^3}\tilde{p} \tag{3.6}$$

where λ is a small but nonzero positive constant. With this biharmonic term, infinite steepening of the pressure profile is avoided. However, the negative diffusion can still drive instabilities with wavelengths longer than $\sqrt{\lambda/\chi_{max}}$. In the numerical calculation, the gridsize Δx is finite, so the shortest wavelength of such instabilities is Δx. To stabilize this numerical instability at the shortest wavelength, we require $\lambda > (\chi_{eff})_{max}(\Delta x)^2$. On the other hand, we require $\lambda << 1$ so that the dissipation of this biharmonic term on the bulk of the plasma is very small. As long as $\lambda << 1$, the biharmonic term is important only in a narrow layer near the plasma edge, whose width is proportional to $\sqrt{\lambda}$. We will show later that our analytic results have a well-defined limit as $\lambda \to 0$.

We still need to determine the safety factor q profile. We consider two limiting cases: one is the flux-conserving tokamak case, and the other is the non-flux-conserving case. For the flux-conserving case, we assume rapid heating compared to the magnetic skin time , so that the poloidal field is constant and the q profile is fixed; in particular, we take it to have the form $q = 1+2x^2$. Note

that $S = 1.33$ at the plasma edge for this particular choice of profile. On the other hand, for the flux non-conserving case, we assume slow heating compared to the skin time; then $q(x,t)$ can be self-consistently determined from Ohm's law and Ampere's equation:

$$J_z = \frac{1}{r}\frac{\partial}{\partial r} r B_\theta = \sigma E_z, \tag{3.7}$$

where J_z is the toroidal current density, E_z is the toroidal electrical field, and σ the electrical conductivity. Using the Spitzer resistivity, we have $\sigma \propto p^{3/2}$ for uniform density. Then the normalized form of Eq. (3.7) is as follows:

$$\frac{\partial}{\partial x}\left(\frac{x^2 q_a}{q}\right) = \frac{x\bar{p}^{3/2}}{\int_0^1 x\bar{p}^{3/2} dx} \tag{3.8}$$

3.3 Numerical Results

Eq. (3.6) was integrated as an initial value problem in time with an implicit scheme, and as a boundary value problem in radius with a centered difference scheme. The boundary conditions employed here were $\partial p/\partial r = 0$ and $\partial^3 p/\partial r^3 = 0$ at $r = 0$ (magnetic axis), and $p = 0$ and also $\partial^2 p/\partial r^2 = 0$ at $r = a$ (plasma edge).

Figure 3.2 shows the time evolution of the pressure gradient profile for the flux-conserving case. Recall that the safety factor profile, which is constant in this case, was taken to be $q = 1 + 2x^2$. The sequence shown in Fig. 3.2 was obtained with $H = 30$, $\chi_{max} = 20$, $\lambda = 0.025$, $S_m = 0.8$, $c_1 = 0.8$, and $c_2 = 0.4$. The dotted curve is the generic ballooning stability boundary, plotted in the $(-\partial p/\partial r, r/a)$ space. Inside this dotted curve the ballooning mode is unstable, whereas the region below the unstable regime is the first stability regime and the region above it is the second stability regime. Initially, for small heating power, the plasma profile (solid curve a) is completely in the first

stability regime. At time $\tau = 0$, we increased the heating power to $H = 30$, which is above the critical threshold power; then the plasma pressure begins to increase, as does the pressure gradient. After a time $\tau = 0.1$ has passed, a large part of plasma (curve b) has entered the ballooning unstable region. At time $\tau = 0.15$, the profile (curve c) has entered the second stability regime at all radii except near the plasma edge. Finally, at $\tau = 0.175$, the entire plasma profile (curve d) is in the second regime, although it is still evolving to higher pressure gradients. Eventually, the profile attains a globally second-stable equilibrium that no longer changes in time.

Figure 3.3 shows the result when the power is not sufficiently large: the pressure profile reaches a steady state, but the profile is not everywhere in the stable domain. Figure 3.3 was obtained with $H = 21$, which is just below the critical value $H_{crit} = 21.5$.

By varying the applied power, one finds the critical value below which such access becomes impossible. Shown in Fig. 3.4 are the numerical results for the critical heating power parameters H_{crit} versus the transport enhancement factor χ_{max}, with the parameters of Fig. 3.2 (except for λ). Approximately, we have the scaling relationship:

$$H_{crit} = 5\sqrt{\chi_{max}} \tag{3.9}$$

Choosing an appropriate value for λ is a subtle issue. On the one hand, λ must be large enough to overcome the negative diffusion-induced instability and to maintain numerical accuracy; on the other hand, λ must be small enough to make our result independent of λ. We found, within numerical error, that H_{crit} does slightly depend on λ for finite values of λ. But as λ goes

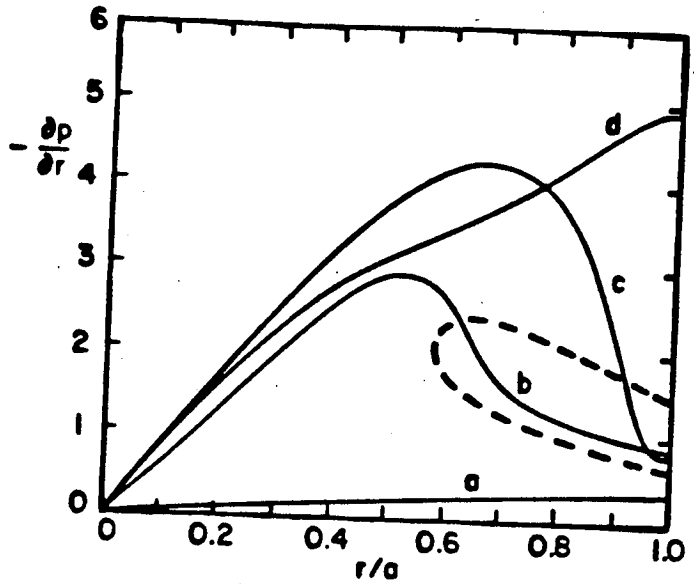

Figure 3.2: Pressure–gradient profile evolution relative to the ballooning stability boundary (dotted line) with parameters $H = 30$, $\chi_{max} = 20$, $\lambda = 0.025$ $S_m = 0.8$, $c_1 = 0.8$, and $c_2 = 0.4$.

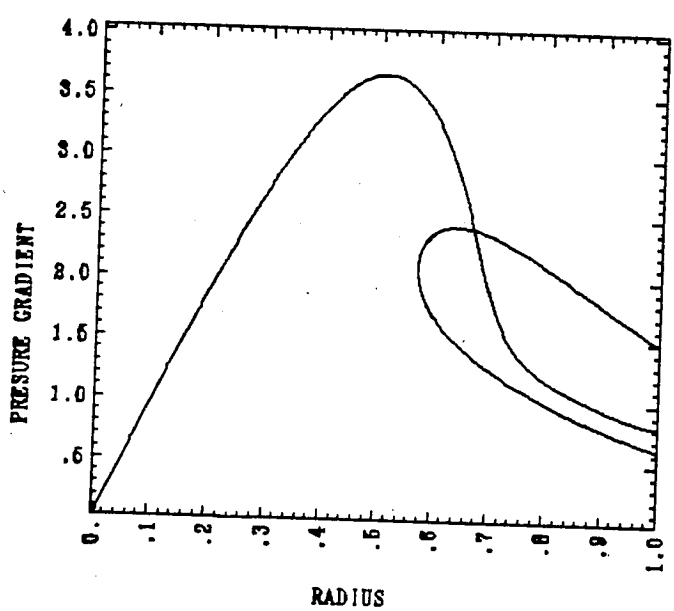

Figure 3.3: Steady-state pressure–gradient profile with $H = 21$, just below the critical value $H_{crit} = 21.5$, for the parameters of Fig. 3.2.

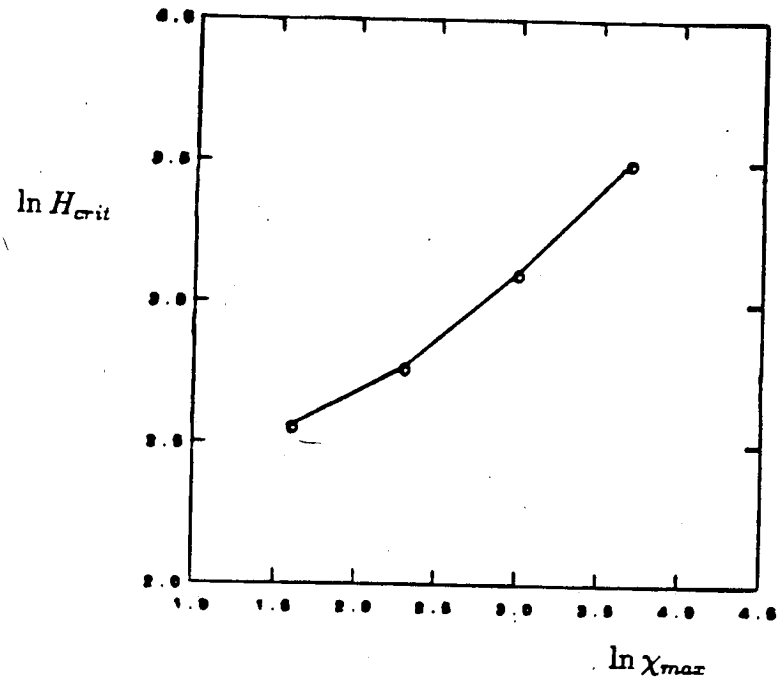

Figure 3.4: Numerically obtained critical heating power parameter H_{crit} versus χ_{max} for a fixed q-profile with the parameters of Fig. 3.2 and $\lambda = 1.25 \times 10^{-3}\chi_{max}$.

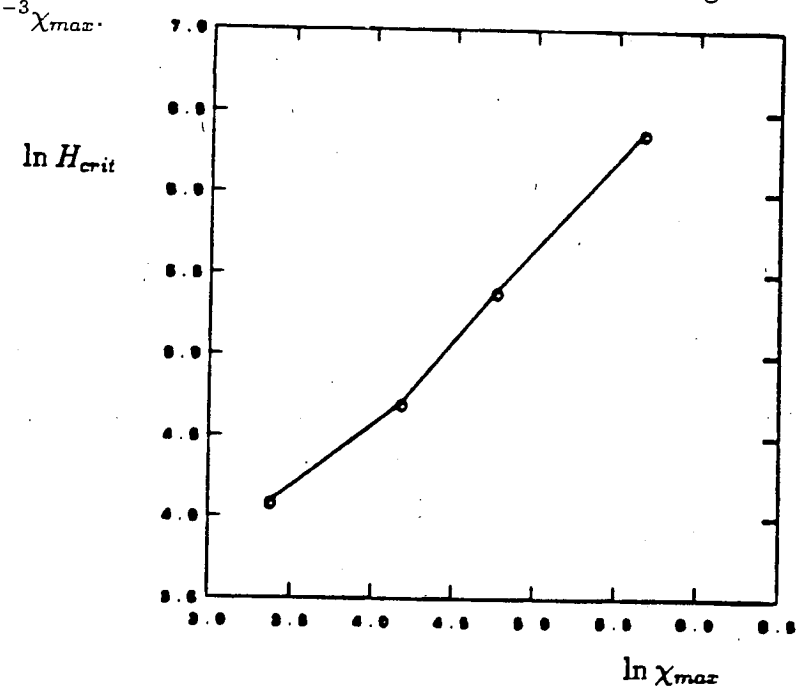

Figure 3.5: As in Fig. 3.4, but for a q-profile that varies in time according to Ohm's law, with $\lambda = 2 \times 10^{-4}\chi_{max}$.

to zero, H_{crit} saturates to a limiting value. In obtaining Eq. (3.9), we have chosen λ as

$$\lambda = 1.25 \times 10^{-3} \chi_{max} \tag{3.10}$$

In the next section we will show that as long as λ is small enough, H_{crit} does not depend on λ.

We have also studied the non-FCT case. Here the q profile is determined in terms of $\tilde{p}$ from Eq. (3.8), and our transport equation Eq. (3.6) has to be solved in conjunction with Eq. (3.8). Shown in Fig. 3.5 are the numerical results for H_{crit} versus χ_{max}, plotted for the same parameters as Fig. 3.4, but with $\lambda = 2 \times 10^{-4} \chi_{max}$. We obtain approximately

$$H_{crit} = 1.7 \chi_{max} \tag{3.11}$$

Notice that in the flux non-conserving case, a linear scaling with χ_{max} holds instead of the square root scaling for the flux-conserving case. In the next section we will derive these scalings analytically in the small λ limit.

3.4 Analytic Theory

3.4.1 Analysis of Edge Behavior

In Fig. 3.2 it can be observed that the last part of the pressure profile to make the transition into the second stability regime occurs near the edge of the plasma, where the enhanced thermal conductivity is maximum. Therefore, let us consider the behavior of the transport equation near the plasma boundary.

To begin with, integrate Eq. (3.6) once to obtain

$$\frac{\partial}{\partial \tau} \int_0^x dx' x' \tilde{p}(x', t) = x \chi_n \frac{\partial}{\partial x} \tilde{p} + \frac{1}{2} x^2 H - \lambda x \frac{\partial^3}{\partial x^3} \tilde{p} \tag{3.12}$$

Now explore the possibility of the existence of a stationary solution ($\partial/\partial\tau = 0$), near the edge of the plasma. Change the radial coordinate to $\xi = 1 - x$ (with $|\xi| << 1$), take $S = S(x = 1)$ =constant, and define $y = \partial\tilde{p}/\partial\xi$ as the independent variable. Equation (3.12) can then be rewritten as

$$\lambda \frac{d^2 y}{d\xi^2} = -\frac{\partial}{\partial y} V(y), \tag{3.13}$$

with

$$V(y) = \frac{1}{2} H y - \frac{1}{2} y^2 - \int_{\bar{\alpha}_1}^{y} dy' y' \left[\chi_n(y') - 1\right] \tag{3.14}$$

Equation (3.13) has the form for the one-dimensional motion of a particles of "mass" λ in a potential $V(y)$. We pursure this analogy, adopting techniques that have been used by Sagdeev [54] and others to study laminar shocks. In particular, we desire a bounded solution for the "coordinate" y that extends in "time" ξ from first stability at the plasma edge (i.e., small y, meaning small pressure gradient) to large y (second stability) in the plasma interior. The form for the potential $V(y)$, which is shown in Fig. 3.6, has a valley between two peaks; the height of the peak at large y increases with the applied power, whereas the height of the peak at small y is nearly constant. In the language of the motion of a ball in a potential, we want a solution for which a ball (which starts with zero velocity) rolls down the hill from the peak at large y and goes no farther than the peak at small y. This desired motion of a ball is possible only if the height of the peak at the large y is the same or lower than the peak at small y. Therefore the critical heating power, i.e., the heating power below which the plasma cannot gain access to the second regime, is determined by the condition that the two peaks of the potential have equal height. For $\chi_{max} >> 1$, this threshold can be analytically determined as:

$$H_{crit} = \left\{ 8 \int_{\bar{\alpha}_1}^{\bar{\alpha}_2} dy y \left[\chi(y) - 1\right] \right\}^{1/2} \tag{3.15}$$

This edge analysis reproduces the $\chi_{max}^{1/2}$ scaling of H_{crit} that was obtained numerically. However, the proportionality coefficient predicted from Eq. (3.15), when evaluated for the parameters of Fig. 3.2, is

$$H_{crit} = 2.2\sqrt{\chi_{max}} \tag{3.16}$$

which is approximately one-half of the value for the coefficient that was found numerically and is given in Eq. (3.9). In next section we will give a refined theory to explain this discrepancy.

3.4.2 Boundary Layer Analysis

Here we will develop a refined theory to resolve the discrepancies between the numerical results of Eq. (3.9) and Eq. (3.11) and the analytic scaling of Eq. (3.16). In particular, there is a factor of two difference for the flux-conserving case. The problem is more serious for the flux non-conserving case, where the discrepancy lies not merely in the coefficient but rather in the scaling. Therefore, a unified analytic theory is called for.

We also are motivated by the numerical results for the typical marginal steady state profile just before transition to second stability regime. Shown in Fig. 3.7 is a typical marginal profile of y versus x. Notice we can characterize $y(x)$ in terms of three parts: namely, interval A in the stable regime $0 < x < x_1$; interval B with $x_1 < x < x_2$, which is a boundary layer in which y changes very rapidly; and finally interval C with $x_2 < x < 1$ in the unstable regime, in which y varies slowly. Observe that the boundary layer for the marginal steady state is located at $x = x_1 < 1$, rather than at $x = 1$, as was assumed in the edge analysis of Sec. 3.4.1. Here we will show that the location of the boundary layer is very crucial to the coefficient of the H_{crit} scaling and that

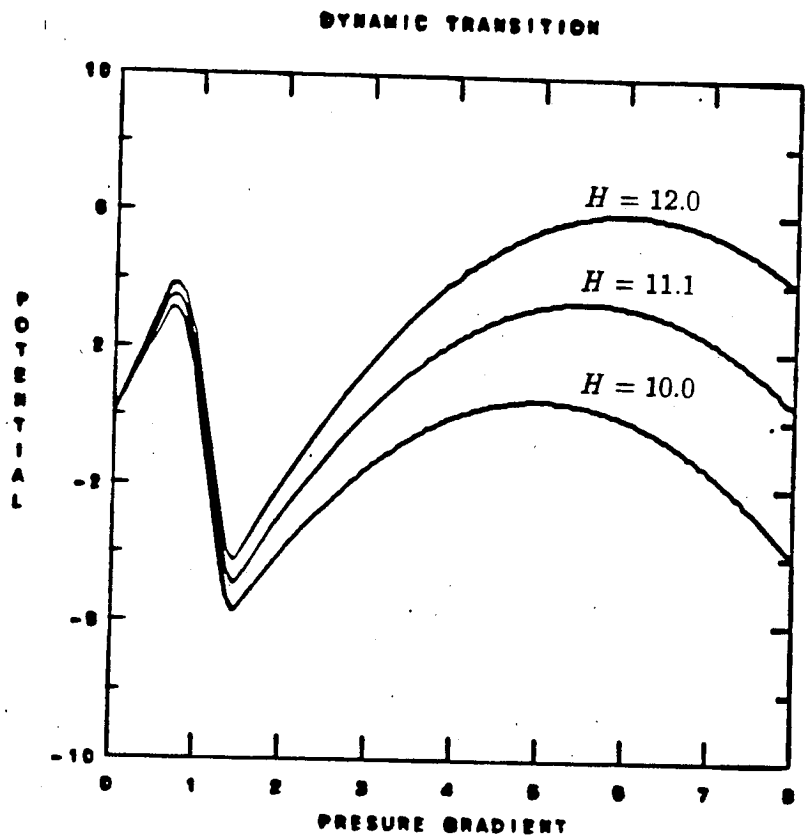

Figure 3.6: Potential $V(y)$ for the same parameters as in Fig. 3.2.

the assumption of the boundary layer being at the edge is exactly the reason for the existence of the discrepancies.

Here we solve Eq. (3.6) in the unstable interval B by the boundary layer method, and then we match this boundary layer solution to the stable solution in the interval labelled A. To begin with, Eq. (3.6) can be integrated once in x, and rewritten, as for the steady state in the following form:

$$\lambda \frac{d^2y}{dx^2} = \chi_n(y,x)y - \frac{1}{2}Hx \tag{3.17}$$

The solution for Eq. (3.17) in interval A can be easily obtained because $\chi_n = 1$; we find

$$y = \frac{1}{2}Hx + (y_1 - \frac{1}{2}Hx_1)\frac{\sinh(x/\sqrt{\lambda})}{\sinh(x_1/\sqrt{\lambda})} \tag{3.18}$$

where the boundary conditions $y(0) = 0, y'' = 0$, and $y(x_1) = y_1$ have been used. Note that y_1 is the value of y at the second stability boundary, with $x = x_1$. Then the derivative of y at $x = x_1$ is

$$y'_{x_1^-} = (\frac{dy}{dx})_{x=x_1} \cong -\frac{1}{2}H\frac{(x - \sqrt{\lambda} - 2y_1/H)}{\sqrt{\lambda}} \tag{3.19}$$

Here we assumed $\lambda << 1$ so that $\sinh(x_1/\sqrt{\lambda}) \approx \cosh(x_1/\sqrt{\lambda})$.

In interval B, since y varies rapidly as a function of x, Eq. (3.17) can be treated as a boundary layer problem. That is to say, because $\lambda << 1$, we can neglect the x variation on the right-hand side of Eq. (3.17). Then the solution can be obtained with potential analysis, and Eq. (3.17) can be rewritten in form

$$\lambda \frac{d^2y}{dx^2} + \frac{dV(y)}{dy} = 0 \tag{3.20}$$

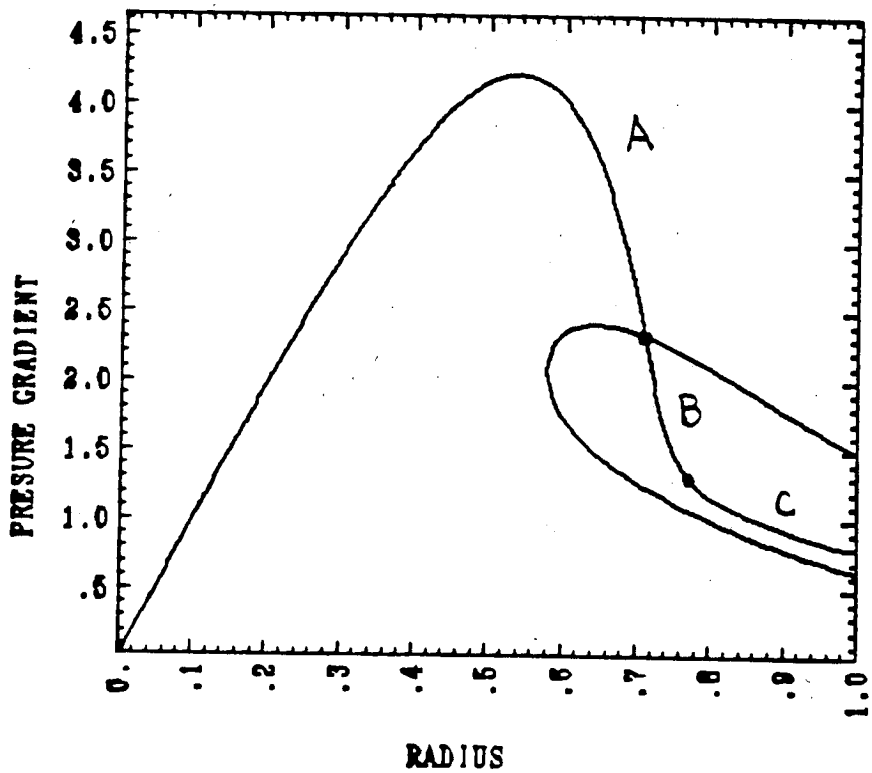

Figure 3.7: A typical steady-state pressure gradient profile just before transition to the second stability

where

$$V(y) = \frac{1}{2}Hx_1 y - \frac{1}{2}y^2 - \int_{y_1}^{y} dy' y' \left[\chi_n(y', x_1) - 1\right] \tag{3.21}$$

Here Eq. (3.20) is same as Eq. (3.13), except that now the boundary layer is located at $x = x_1 < 1$ instead of at $x = 1$. The solution to Eq. (3.20) is easily obtained as

$$\begin{aligned} & \frac{1}{2}\lambda(y'^2(x) - y'^2(x_1)) = V(y_1) - V(y) \\ = \; & \frac{1}{2}Hx_1(y_1 - y) - \frac{1}{2}(y_1^2 - y^2) + \int_{y_1}^{y} dy' y' \left[\chi_n(y', x_1) - 1\right] \end{aligned} \tag{3.22}$$

or for $x = x_2$:

$$\begin{aligned} y'^2_{x_1^+} &= y'^2(x_1) \\ &= \frac{2}{\lambda}\left\{\int_{y_2}^{y_1} dy' y'(\chi_n(y', x_1) - 1) \right. \\ &\quad \left. + \frac{1}{2}(y_1^2 - y_2^2) - \frac{1}{2}Hx_1(y_1 - y_2)\right\} \end{aligned} \tag{3.23}$$

where we have neglected y'^2_{x2} for simplicity (since $|y'_{x_2}| << |y'_{x_1}|$).

Matching Eq. (3.19) and Eq. (3.23), we obtain

$$y'^2_{x_1^-} = y'^2_{x_1^+} \tag{3.24}$$

or

$$H = \frac{2\delta y_2 + \sqrt{8\int_{y_2}^{y_1} \chi_n(y, x_1) y dy + 4(\delta^2 - 1)y_2^2}}{x_1 - \sqrt{\lambda}} \tag{3.25}$$

with

$$\delta = \frac{1 - \sqrt{\lambda} y_1/(x_1 y_2)}{1 - \sqrt{\lambda}/x_1} \tag{3.26}$$

We make the following observations regarding Eq. (3.25):

(1) In general, H is a function of the parameters λ, χ_{max}, and x_1 and also of the stability boundary. For the case of a flux-conserving tokamak, the stability boundary in $y - x$ space is fixed, since $q(x)$ is fixed. Then H is only a function of x_1, for a given value of λ. Shown in Fig. 3.8 is H plotted as a function of x_1, for the parameters of Fig. 3.2. Notice that there is a maximum; at this point, the critical power parameter H_{crit} can be determined. Figure. 3.9 compares the numerical results and the analytic results from both edge analysis and boundary layer theory. It is evident that the boundary layer theory provides a substantial improvement over the edge analysis in terms of agreement with the numerical results. In fact, we have approximately from Eq. (3.25),

$$H_{crit} = 4\sqrt{\chi_{max}} \tag{3.27}$$

(2) In the limit of $\lambda = 0$, $x_1 = 1$, and $\chi_{max} >> 1$, Eq. (3.25) reproduces the analytic scaling given by the edge analysis, viz., that in Eq. (3.15)

(3) For the flux non-conserving case, the procedure to obtain H_{crit} is more subtle, since now the safety factor profile $q(x)$ is related to $\tilde{p}(x)$, or $y(x)$, and Eq. (3.17) has to be solved self-consistently in conjunction with Ohm's law. As H increases, the $\tilde{p}(x)$ profile tends to peak near the center, and as a result the stability boundary in $y - x$ space will change accordingly; in particular, the nadir point, corresponding to $S = S_m$, will be lowered. Numerically, we find that the net effect is to decrease the value of x_1 in Eq. (3.25). It is readily shown analytically that x_1 scales approximately as $x_1 \propto 1/\sqrt{H}$, for the marginal steady state. Therefore, from Eq. (3.25), we obtain a linear scaling: $H_{crit} \propto \chi_{max}$. To determine the coefficient for this linear scaling, one has to

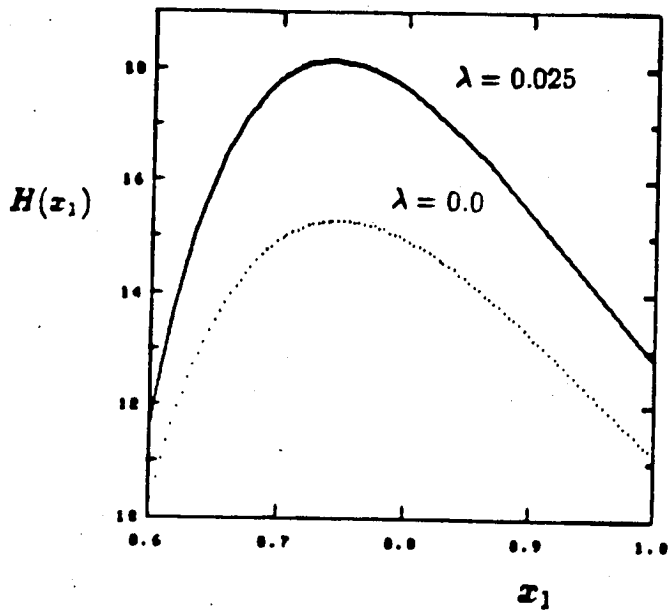

Figure 3.8: Function $H(x_1)$ with the parameters of Fig. 3.2. The $\lambda = 0$ limit is shown as a dotted curve.

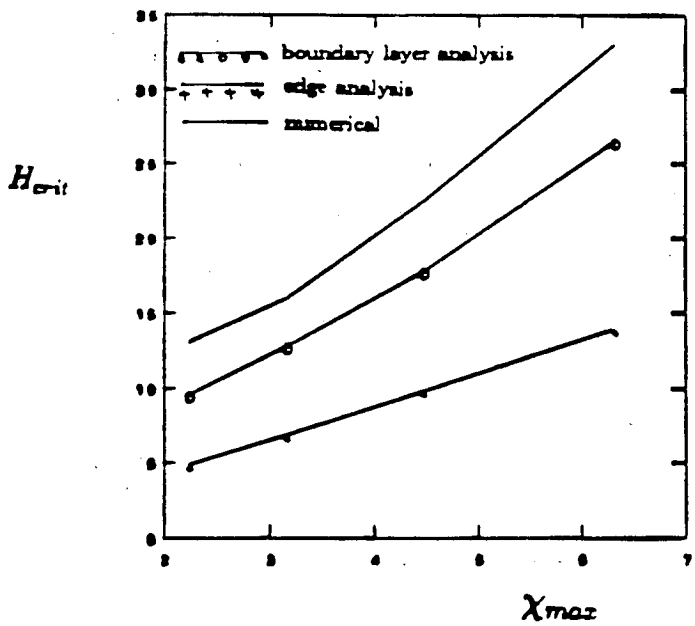

Figure 3.9: Comparison of the numerical H_{crit} with the analytic results from the edge analysis and the boundary layer analysis, with the parameters of Fig. 3.2.

solve for the entire profile $\tilde{p}(x)$ self-consistently; this algebra is quite involved and not illuminating, so we will not pursue it here farther.

(4) The effect of hot particle stabilization (or whatever supplemental stabilization is assumed) on H_{crit} is implicitly seen through the dependence on the stability boundary in Eq. (3.25). For example, the presence of hot particles [3] tends to raise the nadir point ($S = S_m$) of the stability boundary. As a result, the value for the boundary layer position x_1 is increased and H_{crit} decreases accordingly. Shown in Fig. 3.10 is the plot for H_{crit} versus S_m, with $\chi_{max} = 20$. As expected, the value for H_{crit} is seen to decrease as $S_m$increases.

3.5 Power Threshold Estimate

Having derived the threshold for the numerical quantity H, we now proceed to calculate the corresponding power. Obviously, any such estimate depends on what type of confinement scaling is taken to be dominant in the stable regime, how large an enhancement factor is assumed to be produced by the unstable ballooning modes, and what the size of the unstable region is in parameter space.

As a useful point of comparison, we apply our results to the Second Regime Experiment (SRX), a large-aspect-ratio tokamak that has been proposed at Columbia University [16,55]. Recently, the SRX group [16] has coupled the two-dimension PEST equilibrium and stability code with the flux-surface averaged BALDUR transport code and has numerically studied the time evolution of a flux-conserving tokamak plasma under the influence of neutral beam heating. The tokamak parameters in their study were $R = 1.53$ m, $a = 0.17$ m, $B_0 = 1.0$ T, and $q_a = 4.0$. Using L-mode transport scaling in the

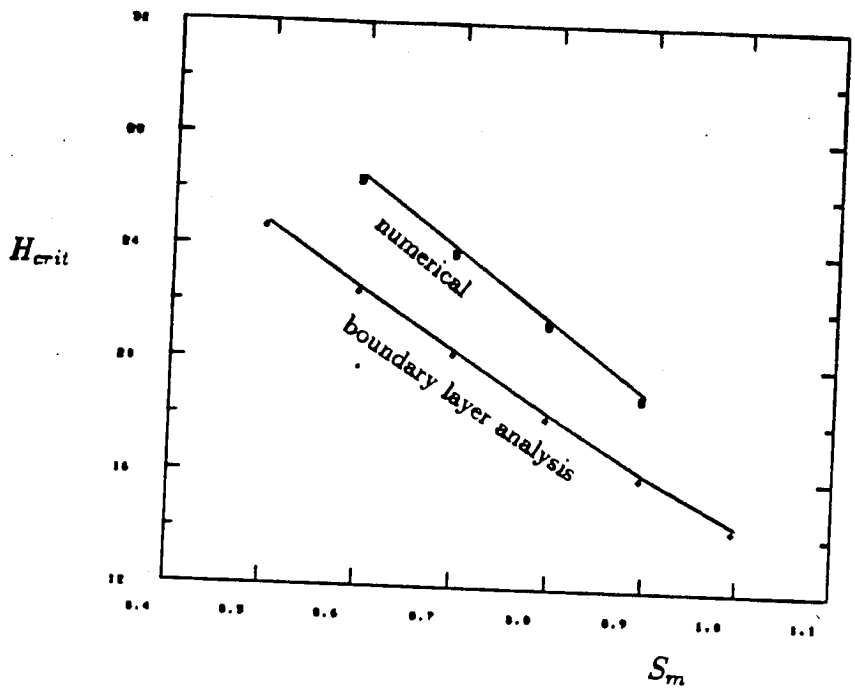

Figure 3.10: H_{crit} as a function of S_m, with the parameters of Fig. 3.2.

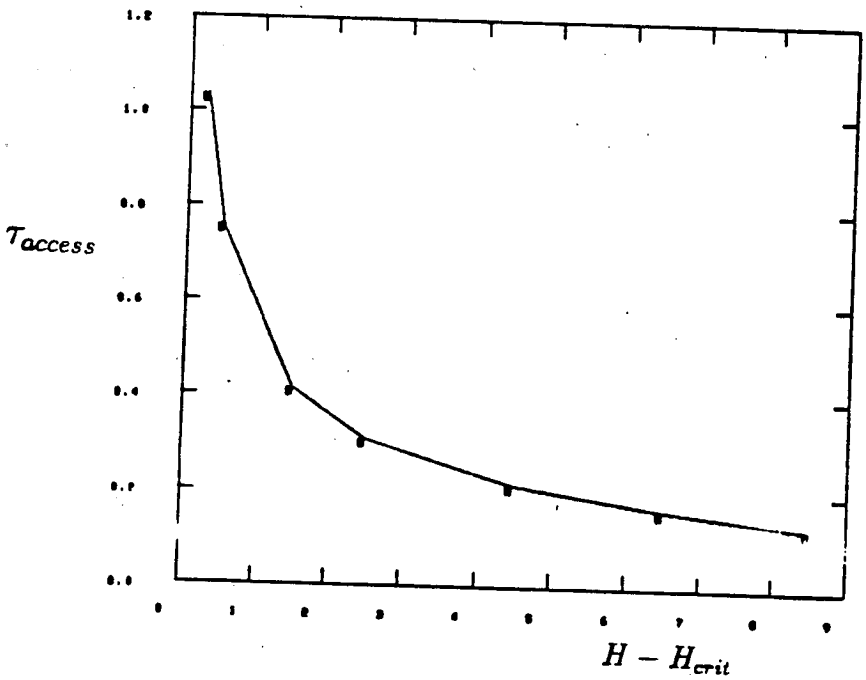

Figure 3.11: Time required for the plasma to go through the ballooning unstable zone, with parameters $S_m = 0.8$, $c_1 = 0.80$, $c_2 = 0.40$, $\lambda = 2.5 \times 10^{-2}$, and $\chi_{max} = 20$.

ballooning stable regime and enhancing it by a factor of ten in the unstable regime (which brings it up to the Bohm level, approximately), they found that the application of 2.6 MW of neutral beam heating would be sufficient to power the SRX plasma into a second-stable configuration.

Accordingly, with our model, we incorporate Kaye-Goldston L-mode confinement scaling [15] (i.e., $\tau_E \approx P^{-0.59}$), take $\chi_{max} = 10$, and select the parameters $S_m = 1.0$, $\bar{\alpha}_1 = 0.5$, and $\bar{\alpha}_2 = 1.3$, which approximately correspond to the simulation of Ref. 16. Then our analytic result, in the limit of $\lambda \to 0$, would predict $P_{crit} = 7.5$ MW. This number is reasonably close to the 2.6 MW of the simulation, considering how many simplications were made in our model.

We have also calculated the time T_c needed for the plasma to go through the ballooning unstable gap. The result is shown in Fig. 3.11 for the parameters $c_1 = 0.80$, $c_2 = 0.40$, $S_m = 0.8$, $\lambda = 2.5 \times 10^{-2}$, and $\chi_{max} = 20$. We observe that the time T_c decreases very rapidly with increasing H. Approximately one energy confinement time is found to be required for access when the power is about 30% higher than the critical power value. (of course, more time passes before the solution eventually settles down to a truly time-independent equilibrium.)

3.6 Concluding Remarks

We have numerically and analytically obtained the H_{crit} versus χ_{max} scalings for both flux-conserving tokamaks and flux non-conserving tokamaks. The difference between these two scalings implies that the flux-conserving tokamak demands much less heating power for access to the second stability regime.

Even though this theory for dynamical access to second stability predicts a large pressure gradient and a threshold in power, we do not claim it as

an explanation for the L-mode to H-mode transition in auxiliary heated tokamak. However, the application of this type of transport treatment to equilibria that incorporate the effect of a separatrix on ballooning modes, such as have been considered by Bishop [56], could be useful.

Also, we distinguish between our globally second stable, time-asymptotic solution and a "locally" second stable profile that has been recently described by Seki et al. [57]. In the latter, the pressure is strongly peaked near the magnetic axis, but relaxes to a flat, first-stable configuration for large values of the minor radius. (This sort of profile would appear to be susceptible to moderate-mode-number infernal modes [58].) In contrast, our solution lies above the second stability limit.

It should be pointed out that the power requirements for access to second stability tend to favor small machines with large aspect ratios. For example, with Kaye-Goldston L-mode confinement, the threshold power scales as $P_{aux} \propto \chi_{max}^{1.19} a^{2.04} B^{1.40} q_a^{-1.19} (R/a)^{-0.36}$. Thus, estimates similar to that of Sec. 3.5, but applied to the proposed Compact Ignition Tokamak(CIT) and International Thermonuclear Experimental Reactor (ITER) would require hundreds of megawatts, simply because these devices are not designed to exploit second stability.

Finally, we again note that our simple transport/stability model appears to give results that are both qualitatively and quantitatively in reasonable agreement with more sophisticated computational results. This correlation tends to bolster the viability of a large-aspect-ratio tokamak experiment designed to explore the second stability regime.

Chapter 4

Destabilization of Toroidal Global Shear Alfvén Wave by Fusion-Product Alpha Particles

4.1 Introduction

In an reacting tokamak, the fusion alpha particles are born with an energy of 3.52 Mev and a density that is sharply peaked at the center of the plasma due to the sensitive dependence of the fusion reaction rate on the plasma temperature. Thus the drift-type instabilities may occur due to this free energy source of alpha particle density inhomogenity. In particular, shear Alfvén waves may be driven unstable by the passing alpha particles if $\omega_A < \omega_{*\alpha}$, where ω_A is the shear Alfvén wave frequency and $\omega_{*\alpha}$ is the diamagnetic frequency of alpha particle, since the alpha particle velocity is comparable to the Alfvén wave phase velocity.

There are two kinds of shear Alfvén waves: one kind is the kinetic Alfvén wave (KAW), which is localized at the shear Alfvén singularity, i.e., $\omega^2 = \omega_A^2(r)$; the other is the global-type Alfvén wave, which has no shear Alfvén resonance, i.e., $\omega^2 \neq \omega_A^2(r)$ for all radii of the plasma. There are also two types of global Alfvén waves. The first type is called the global Alfvén eigenmode (GAE), which has its wave frequency located just below the lower edge of the Alfvén continuum, i.e., $\omega^2 < (\omega_A^2)_{min}$. The second type of global mode is called the toroidicity-induced shear Alfvén gap mode (TAGE); its mode frequency is located within the toroidicity-induced gap in the shear Alfvén continuum. In this chapter, the GAE mode is our main concern. Recently, Li,

Mahajan, and Ross [37] studied the stability of the GAE modes in the presence of the fusion alpha particles in an ignited tokamak plasma. They found that GAE modes can be destabilized by the fusion alpha particles. However, in their study, cylindrical geometry was assumed and only one poloidal mode was considered. Here we study the effect of toroidicity on the stability of the cylindrical GAE. Shown in Fig. 4.1 are the shear Alfvén continua for various modes (n, m), where n and m are the toroidal and poloidal mode numbers, respectively. The eigenfrequency of GAE is located just below the minimum of the corresponding continuum. In particular, the $(1, -2)$ GAE mode, with its frequency indicated by a dotted line, has two sidebands $(1, -1)$ and $(1, -3)$ induced by toroidal coupling. More significantly, the sideband $(1, -1)$ has a shear Alfvén singularity at $\omega^2 = k_{\|}^2 v_A^2$ near the edge of the plasma; i.e., the $(1, -1)$ mode is basically a KAW mode with large Landau damping. We will show later that this coupling to a KAW sideband mode can enhance the Landau damping of a GAE mode substantially and can stabilize the cylindrical GAE mode.

In Sec. 4.2 of this chapter, we will give a short review of how the cylindrical GAE mode is destabilized by alpha particles. In particular we will calculate the GAE growth rate for the proposed Compact Ignition Tokamak (CIT) parameters. The importance of using a slowing-down distribution to model the alpha particles will be discussed in detail. Section 4.3 deals with the construction of a proper set of toroidal kinetic equations for the shear Alfvén eigenmode with alpha particles. Section 4.4 describes and discusses our numerical results on the toroidal stabilizing effect. Sec. 4.5 is devoted to a discussion of our conclusions.

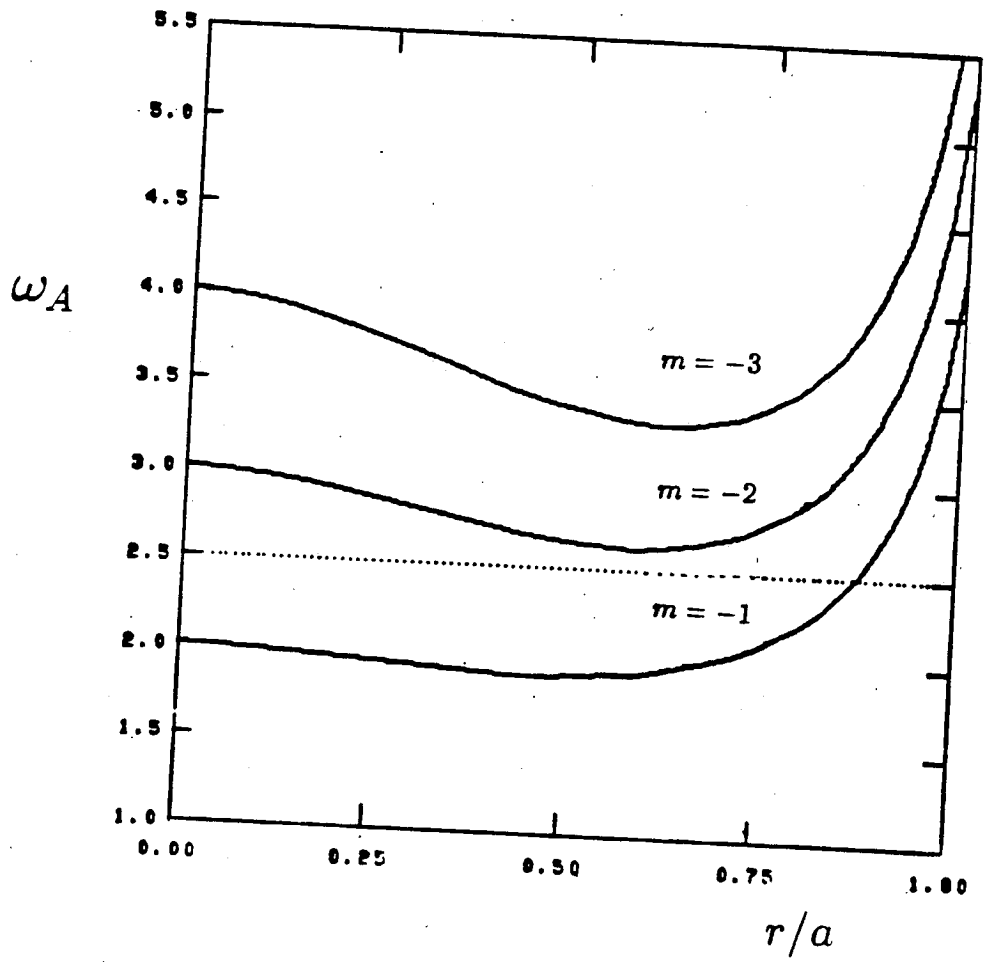

Figure 4.1: Cylindrical shear Alfvén continua for mode number $n = 1$ and $m = -1, -2$, and -3.

4.2 Destabilization of Global Alfvén Wave in Cylindrical Limit

4.2.1 Review of Global Alfvén Wave Destabilized by Alpha Particles

Here we give a unified overview of the cylindrical results for the destabilization of the GAE mode by alpha particles. The proper set of eigenmode equations for the problem has been derived by Li, Mahajan, and Ross [37]. They started from Ampere's law:

$$\nabla \times \nabla \times \mathbf{E} = (\frac{\omega^2}{c^2})\chi \cdot \mathbf{E} \tag{4.1}$$

All the physics of the plasma response is included in the susceptibility χ. An ignited tokamak plasma has two components– the bulk plasma, which constitutes the first component, has relatively high density and low temperature, whereas the fusion-product alpha particles, which are the other component, have low density and high temperature. Accordingly, the susceptibility has two parts, i.e., $\chi = \chi_c + \chi_\alpha$, where χ_c and χ_α comes from the cold component and the hot component alpha particles, respectively. From the well-known low-frequency ($\omega < \omega_{ci}$) susceptibility tensor for a uniform plasma, a simple self-adjoint χ_c [28] for the nonuniform cold plasma is constructed, including all the important kinetic effects. Meanwhile the form for χ_α has been obtained [37] by solving the drift kinetic equation for passing alpha particles (the effect of trapped particles is neglected). Furthermore, it is convenient to decompose the electric field $\mathbf{E}$ into $\mathbf{E} = E_r\mathbf{r} + E_\perp \mathbf{b} \times \mathbf{r} + E_\parallel \mathbf{b}$ where we have defined the unit vector $\mathbf{b} = \mathbf{B}/B$. Also, the parallel component of Ampere's law is replaced by $\nabla \cdot \mathbf{J} = 0$, which in turn enables us to eliminate $E_\parallel$ in terms of E_r and $E_\perp$. Thus, from the other two components of Ampere's law, we have the following

two second-order differential equations, written in matrix form as

$$\tilde{L}\tilde{E} = \begin{pmatrix} L_{rr} & L_{r\perp} \\ L_{\perp r} & L_{\perp\perp} \end{pmatrix} \begin{pmatrix} E_r \\ E_\perp \end{pmatrix} \tag{4.2}$$

where $\tilde{L}$ is the differential matrix operator with the following elements:

$$\begin{aligned} L_{rr} &= \frac{\omega^2}{v_A^2} - {k_\parallel}^2 - {k_\perp}^2 - \frac{11}{8} b_i {k_\perp}^2 + \frac{d}{dr}\frac{3}{8} b_i \frac{1}{r}\frac{d}{dr} r \\ &\quad + k_\parallel \frac{d}{dr} {k_\parallel}^{-1} d_e \frac{v_A^2}{\omega^2}\frac{1}{r}\frac{d}{dr} r \frac{\omega^2}{v_A^2} + S_{rr} - Q_{m-1} - Q_{m+1} \end{aligned} \tag{4.3}$$

$$\begin{aligned} L_{r\perp} &= i\left[-\frac{k_\perp}{r}\frac{d}{dr} r - \frac{k_\perp}{r}\frac{11}{8} b_i \frac{d}{dr} r + \frac{d}{dr}\frac{3}{8} b_i k_\perp \right. \\ &\quad \left. + k_\parallel \frac{d}{dr} {k_\parallel}^{-1} d_e k_\perp - i S_{r\perp} + Q_{m-1} - Q_{m+1} \right] \end{aligned} \tag{4.4}$$

$$\begin{aligned} L_{\perp\perp} &= \frac{\omega^2}{v_A^2} - {k_\parallel}^2 + \frac{d}{dr}\frac{1}{r}\frac{d}{dr} r + \frac{d}{dr}\frac{11}{8} b_i \frac{1}{r}\frac{d}{dr} r - \frac{3}{8} b_i {k_\perp}^2 \\ &\quad - d_e {k_\perp}^2 + S_{\perp\perp} - Q_{m-1} - Q_{m+1} \end{aligned} \tag{4.5}$$

$$\begin{aligned} L_{\perp r} &= -i\left[-\frac{d}{dr} k_\perp - \frac{d}{dr}\frac{11}{8} b_i k_\perp + k_\perp \frac{3}{8} b_i \frac{1}{r}\frac{d}{dr} r \right. \\ &\quad \left. + k_\perp d_e \frac{v_A^2}{\omega^2}\frac{1}{r}\frac{d}{dr} r \frac{\omega^2}{v_A^2} - i S_{\perp r} - Q_{m-1} + Q_{m+1} \right] \end{aligned} \tag{4.6}$$

Here $b_i = (\omega^2/v_A^2)\rho_i^2$ and $d_e = (k_\parallel \rho_s)^2 \left(1 + \omega/k_\parallel v_e Z(\omega/k_\parallel v_e)\right)^{-1}$, with $\rho_i^2 = 2T_i/m_i\omega_{ci}^2$ and $\rho_s^2 = T_e/m_i\omega_{ci}^2$. The wave numbers are given approximately by $k_\perp = m/r$ and $k_\parallel = (n - m/q)/R$, where n and m are the toroidal mode number and the poloidal mode number, respectively. The terms S_{rr}, $S_{r\perp}$, $S_{\perp\perp}$, and $S_{\perp r}$, which arise from the equilibrium current and the shear of the magnetic field, are given in Ref. 28, and the term $Q_{m\pm1}$ is the alpha contribution given in Eqs. (24-25) of Ref. 37 as follows:

$$Q_{m\pm1} = -i\frac{\beta_\alpha}{2R^2}\left(P_{m\pm1} - \frac{\omega_{*\alpha m}}{\omega} R_{m\pm1}\right) \tag{4.7}$$

$$P_{m\pm1} = \frac{\pi\omega}{v_\alpha^4}\int d^3v \left(v_\perp^2/2 + v_\parallel^2\right)^2 \left(-T_\alpha \frac{\partial f_{\alpha 0}}{\partial \epsilon}\right) \delta(\omega - k_\parallel v_\parallel) \tag{4.8}$$

$$R_{m\pm1} = \frac{\pi\omega}{v_\alpha^4}\int d^3v\left(v_\perp^2/2+v_\parallel^2\right)^2 f_{\alpha0}\delta(\omega-k_\parallel v_\parallel) \tag{4.9}$$

Here, $\beta_\alpha = 8\pi n_\alpha T_\alpha/B^2$, and $v_\alpha^2 = 2T_\alpha/m_\alpha$, with T_α, n_α, β_α and v_α being the temperature, density, beta value, and thermal velocity of the alpha particles, respectively. Also, $f_{\alpha0}$ is the alpha particle distribution function. Notice that in the alpha particle terms, the parallel wave-particle Landau-type resonance is of the form $\omega = k_{\parallel m\pm1}v_{\parallel\alpha}$, rather than $\omega = k_{\parallel m}v_{\parallel\alpha}$; i.e., the alpha particles interact with the sideband of the perturbed field. That is because the poloidal variation of the alpha drift velocity $\mathbf{v}_{d\alpha}$ enables the perpendicular fields $E_\perp$ and E_r of mode m to resonantly drive two sidebands, $m\pm1$, of the perturbed alpha particle distribution. This kind of sideband resonance was vividly described by Mikhalovskii [34] — " A particle moving in a magnetic field with an alternating curvature and in the field of perturbation with longitudinal wave number $k_\parallel$ behaves as if it moved in a straight magnetic field and in a field of wave with an effective longitudinal wavenumber $k_{\parallel eff} = k_\parallel \pm 1/qR$." However, in the end, these two sidebands of the distribution amount to a perturbed alpha drift current with the same poloidal mode number as the perturbed field. We observe that toroidal coupling in the alpha particle response is necessary even only one poloidal mode number is considered. This is the first manifestation of the toroidal effect in an otherwise cylindrical problem. In Sec. 4.3, we will study the essential toroidal coupling due to the intrinsically finite value of the inverse aspect ratio (r/R), which drives various poloidal harmonics of the waves under consideration.

The physics of Eq. (4.2) can be stated briefly as following. The b_i terms represent the effect of finite ion Larmor radius, whereas the d_e terms come from the electron parallel dynamics, which result in Landau damping. Without these b_i and d_e terms, the matrix equation Eq. (4.2) can be combined

into a single second-order differential equation, the coefficient of whose second derivative term vanishes at $\omega^2 = k_\parallel^2 v_A^2$: this admits a continuous spectrum. On the other hand, with these terms, a forth-order equation results, and the spectrum is discretized. Furthermore, the alpha terms, $Q_{m\pm1}$, can amount to a positive imaginary part of eigenfrequency; i.e., the alpha particles are destabilizing. To understand this, it is useful to examine the simplest local dispersion relation given by Eq. (39) – (40) of Ref. 37. If one considers the case of a uniform background plasma density and a Maxwellian distribution for the alpha particles, the shear Alfvén wave is described by

$$\frac{\omega^2}{v_A^2} - {k_\parallel}^2 - A_\alpha - ({k_\perp}^2 + {k_r}^2)d_e = 0 \tag{4.10}$$

where

$$\begin{aligned} A_\alpha &= (Q_{m+1} + Q_{m-1}) \\ &= -i\frac{\beta_\alpha}{2R^2}\left(1 - \frac{\omega_{*\alpha}}{\omega}\right)(R_{m+1} + R_{m-1}) \end{aligned} \tag{4.11}$$

The growth rate is given by the following expression:

$$\begin{aligned} \gamma/\omega_A &= -\frac{\beta_\alpha}{4{k_\parallel}^2 R^2}\left(1 - \frac{\omega_{*\alpha}}{\omega}\right)(R_{m+1} + R_{m-1}) \\ &\quad - \left({k_r}^2 + {k_\perp}^2\right)\rho_s^2 \pi^{1/2}\frac{v_A}{v_e} \end{aligned} \tag{4.12}$$

We observe that for $\omega_{*\alpha} > \omega$, the alpha term is destabilizing; this competes with the second term on the right-hand side of Eq. (4.12), i.e., the Landau damping. Also note that the Landau damping is proportional to $(k_r^2 + k_\perp^2)\rho_s^2$, so that for a global mode like GAE mode, the damping is very weak, whereas for the localized KAW modes, with their large k_r, Landau damping can be quite large.

Table 4.1: CIT tokamak parameters

major radius	R(cm)	140
minor radius	a(cm)	67
wall radius	r_w(cm)	85
toroidal field	B_0(T)	10
central electron density	$n_0(10^{14}/cm^3)$	10
central electron temperature	T_{e0}(kev)	30
central ion temperature	T_{i0}(kev)	30
effective mass	m_{eff}(proton mass)	2.5
effective charge	Z_{eff}(electron charge)	3.0

4.2.2 Slowing-Down Distribution Versus Maxwellian Distribution

Here we study the effect of using a slowing-down distribution on the destabilization of the GAE mode by alpha particles for CIT parameters, as compared to using a Maxwellian distribution for the alpha particles, The eigenmode equation, Eq. (4.2), can be solved by the cubic-B spline finite element method. Shown in Fig. 4.2 are the GAE eigenfunctions $(1, -2)$ and $(0, -2)$; Fig. 4.3 gives the corresponding growth rates for both Maxwellian and slowing-down distributions. The parameters for the proposed Compact Ignition Tokamak (CIT) have been used in the calculation; these are given in Table 4.1. Profiles used for the CIT were as follows:

$$n = n_0 \left[1 - r^2/(a+d)^2\right] \tag{4.13}$$

$$T_{e,i} = T_{0e,i} \left[1 - (r/a)^2\right] \tag{4.14}$$

$$q = 1 + 2(r/a)^2 \tag{4.15}$$

where the value of d is chosen such that $n(a)/n_0 = 0.1$. Notice that the $(1, -2)$

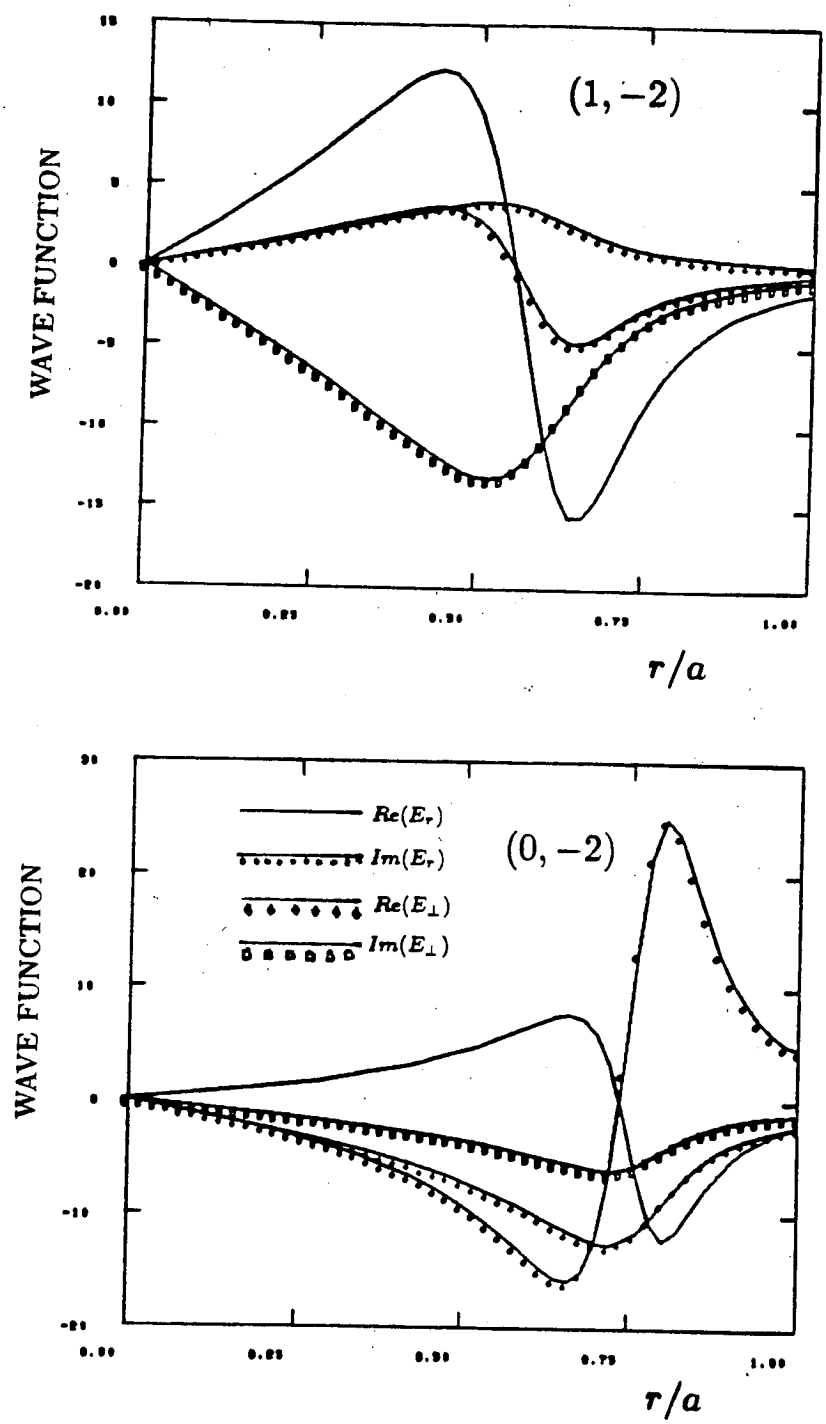

Figure 4.2: Numerical eigenfunctions for the cylindrical global Alfvén eigenmodes with CIT parameters: (a) mode $(1, -2)$; (b) mode $(0, -2)$.

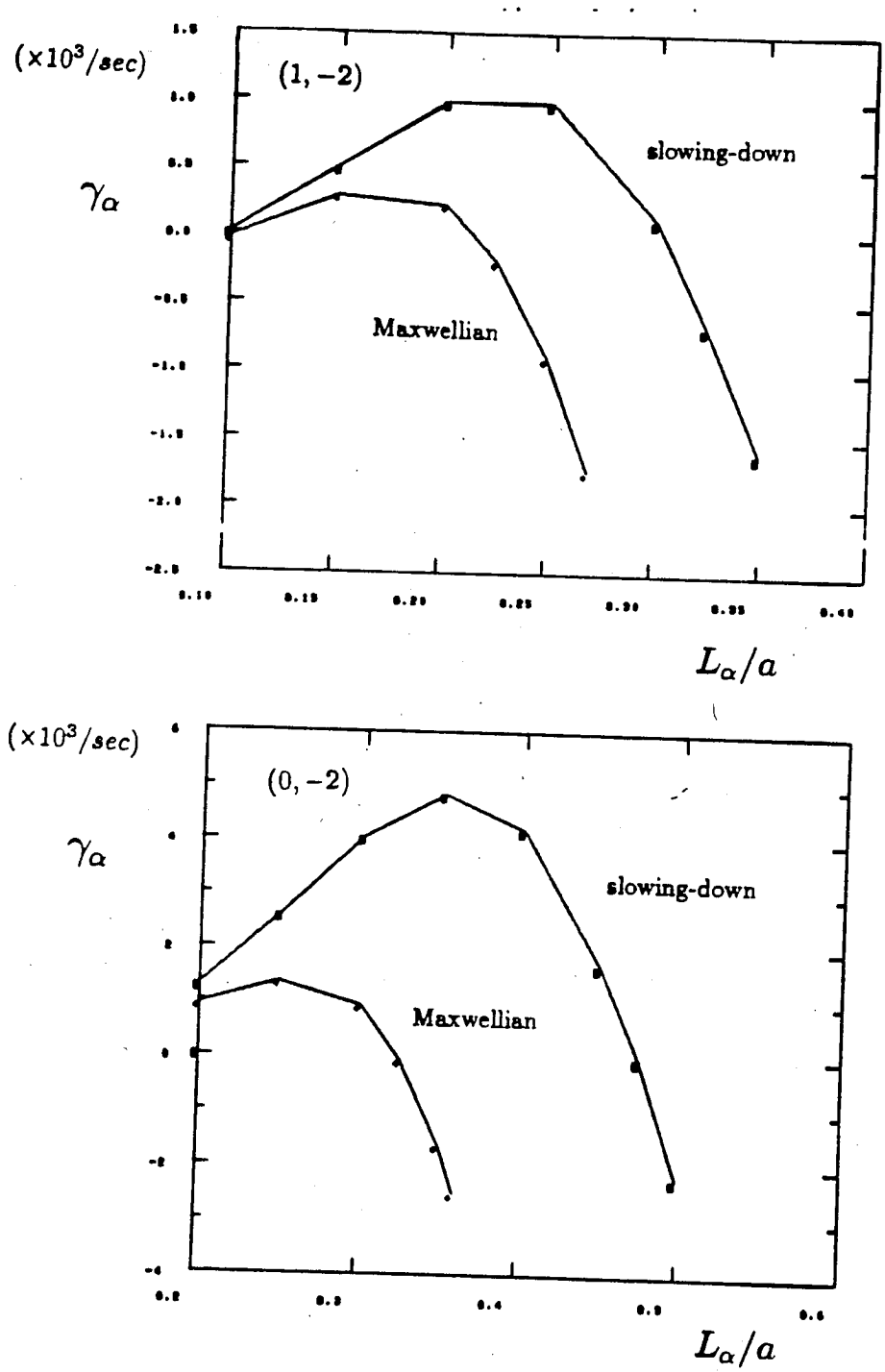

Figure 4.3: Growth rate γ_α for the cylindrical global Alfvén eigenmodes as a function of L_α for a Maxwellian distribution and for a slowing–down distribution, for CIT parameters: (a) mode $(1, -2)$; (b) mode $(0, -2)$.

is weakly damped for a Maxwellian distribution, but is slightly unstable for a slowing-down distribution. However, for the $(0,-2)$ mode, which has been identified as the most unstable mode for TFTR parameters [37], the effect of modeling the alpha particles with a slowing-down distribution is quite remarkable. We observe that the growth rate for a slowing-down distribution is about twice that for a Maxwellian distribution. More significantly, at the expected CIT alpha particle density scale length of $L_\alpha = 0.4a$, the mode is substantially unstable for a slowing-down distribution, but is stable for a Maxwellian distribution.

For a Maxwellian distribution, we have $\partial f_\alpha/\partial E = -f_\alpha/T_\alpha$ so that $P_{m\pm1} = R_{m\pm1}$; on the other hand, for a slowing-down distribution we have $R_{m\pm1} > P_{m\pm1}$, since the velocity integral weights heavily on the large energy side where $-T_\alpha \partial f_\alpha/\partial E \approx (3/2)(T_\alpha/E)f_\alpha > f_\alpha$. Note that for CIT parameters we have $T_\alpha \approx 1$ Mev and the maximum energy of the alphas is 3.52 Mev. Indeed, this has been borne out by our numerical results. Shown in Fig. 4.4 is the ratio of $R_{m\pm1}$ for the two distributions plotted versus the phase quantity $\omega/k_{\|m\pm1}v_{\alpha0}$ and the ratio of $P_{m\pm1}$ to $R_{m\pm1}$ for a slowing-down distribution. We observe that

$$(R_{m\pm1})_{slowing-down} \approx (R_{m\pm1})_{maxwellian} \tag{4.16}$$

for $\omega/k_{\|m\pm1}v_{\alpha0} < 0.8$, and more interestingly that

$$(P_{m\pm1})_{slowing-down} \approx \frac{1}{2}(R_{m\pm1})_{slowing-down} \tag{4.17}$$

Not surprisingly, the growth rate for a slowing-down distribution is greater than with a Maxwellian, as shown in Fig. 4.3. It is also worthwhile to point out that we can estimate the ratio of the critical alpha scale length $L_{\alpha,cr}$ corresponding

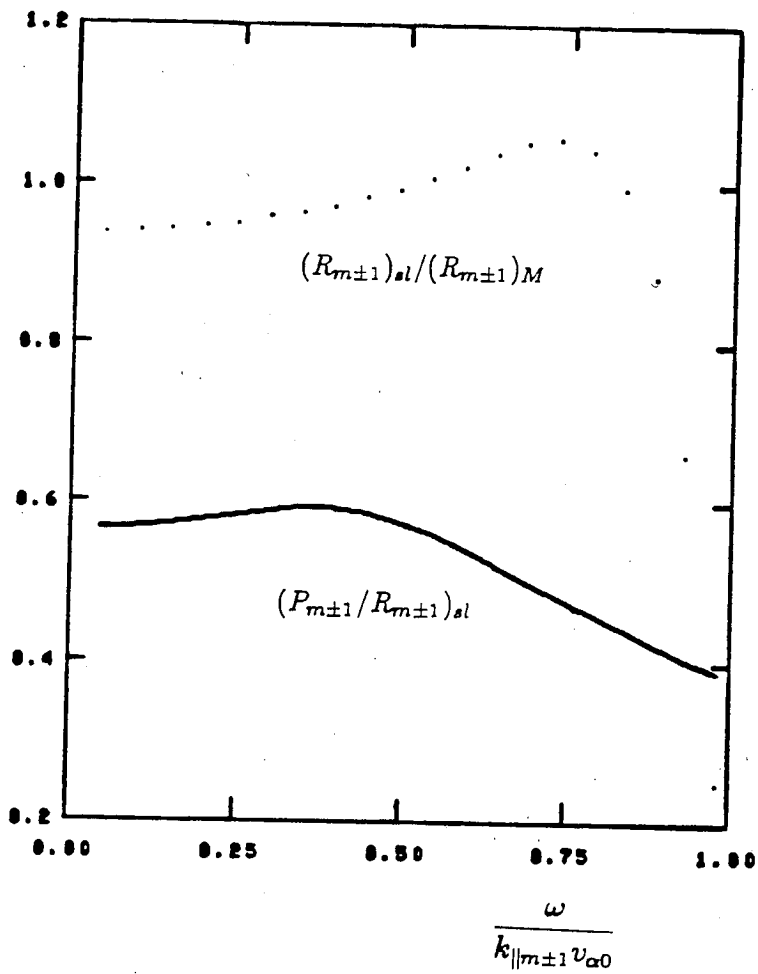

Figure 4.4: Ratio of $(R_{m\pm1})_{sl}/(R_{m\pm1})_M$ and the ratio of $(P_{m\pm1}/R_{m\pm1})_{sl}$ as functions of the phase $\omega/k_{\|m\pm1}v_{\alpha0}$.

to zero growth rate for two the distributions:

$$\frac{(L_{\alpha,cr})_{slowing-down}}{(L_{\alpha,cr})_{maxellian}} \approx \left(\sqrt{\frac{R_{m\pm1}}{P_{m\pm1}}}\right)_{slowing-down} \approx 1.4 \tag{4.18}$$

which is remarkably close when compared to the numerical results shown in Fig. 4.3, which give

$$\frac{(L_{\alpha,cr})_{slowing-down}}{(L_{\alpha,cr})_{maxellian}} = \frac{0.47}{0.33} = 1.4 \tag{4.19}$$

4.3 Toroidal Kinetic Model for Alfvén Wave Eigenmode with Alpha Particles

We start with Ampere's law, Eq. (4.1). It is convenient for us to separate the susceptibility tensor χ into three distinctive parts:

$$\chi = \chi_f + \chi_k + \chi_{alpha} \tag{4.20}$$

Here χ_f is the cold plasma fluid response and χ_k is the cold plasma kinetic response, which includes the finite ion Larmor radius effect and the parallel electron dynamics. The form of χ_f can be derived from the ideal MHD equations, as the following:

$$\chi_f = \frac{c^2}{v_A^2}(\mathbf{I} - \mathbf{bb}) \tag{4.21}$$

where $\mathbf{I}$ is the unit tensor. To have a clear physical picture, we rewrite Ampere's law into the following form:

$$\left(\nabla \times \nabla \times -\frac{\omega^2}{c^2}\chi_f\right)\mathbf{E} = \left(\chi_k + \chi_{alpha}\right)\mathbf{E} \tag{4.22}$$

with the left-hand side corresponding to the ideal MHD dynamics, and the righthand side representing the kinetic effects of the cold component and the alpha particles, respectively. In toroidal geometry, all the terms in Eq. (4.22)

contain some mode coupling. Here we keep only the coupling from the left-hand side of Eq. (4.22) and neglect the toroidicity due to the kinetic response from the cold component and alpha particles. This approximation may be justified for the following reasons. The mode coupling from the alpha particles is small because of the ordering $\beta_\alpha << 1$. Meanwhile, the kinetic term χ_k is small except near the shear Alfvén resonance, so we can neglect the toroidicity contribution of χ_k, at least away from the Alfvén resonance. Furthermore, we find that the kinetic mode coupling near the resonance can also be neglected, since the mode coupling due to $\frac{\omega^2}{v_A^2}$ and ${k_\parallel}^2$ combines. Therefore, we may use the cylindrical form of χ_k in Eq. (4.22).

To simplify the mode coupling due to the operator term $\nabla \times \nabla \times$ and the χ_f term, we assume concentric flux surfaces and use the following toroidal coodinates:

$$\begin{cases} x = R\cos(-\varphi) \\ y = R\sin(-\varphi) \\ z = r\sin\theta \\ R = R_0 + r\cos\theta \end{cases}$$

In terms of this toroidal coodinate system and with the representation $\mathbf{E} = (E_r, E_\perp, E_\parallel)$ for the electric field, we find the components of $\nabla \times \nabla \times \mathbf{E}$ to be

$$\begin{aligned} & (\nabla \times \nabla \times \mathbf{E})_r \\ = & \left(\frac{1}{R^2}\frac{\partial^2}{\partial\varphi^2} + \frac{1}{r^2 R}\frac{\partial}{\partial\theta}R\frac{\partial}{\partial\theta}\right)E_r + \\ & \left(-\frac{1}{r^2 R}\frac{\partial}{\partial\theta}R\frac{\partial}{\partial r}\frac{r}{\sqrt{1+\delta^2}} + \frac{1}{R^2}\frac{\partial}{\partial\varphi}\frac{\partial}{\partial r}\frac{R\delta}{\sqrt{1+\delta^2}}\right)E_\perp - \\ & \left(\frac{1}{rR}\frac{\partial}{\partial\theta}R\frac{\partial}{\partial r}\frac{r\delta}{\sqrt{1+\delta^2}} + \frac{1}{R^2}\frac{\partial}{\partial\varphi}\frac{\partial}{\partial r}\frac{R}{\sqrt{1+\delta^2}}\right)E_\parallel \end{aligned} \tag{4.23}$$

$$
\begin{aligned}
&(\nabla \times \nabla \times \mathbf{E})_\perp \\
= &\left(-\frac{1}{R\sqrt{1+\delta^2}}\frac{\partial}{\partial r}\frac{R}{r}\frac{\partial}{\partial\theta} + \frac{\delta}{r\sqrt{1+\delta^2}}\frac{\partial}{\partial r}\frac{r}{R}\frac{\partial}{\partial\varphi}\right)E_r + \\
&\left[\frac{1}{R\sqrt{1+\delta^2}}(\frac{\partial}{\partial\varphi}+\frac{1}{q}\frac{\partial}{\partial\theta})\frac{1}{R}(\frac{\partial}{\partial\varphi}+\frac{1}{q}\frac{\partial}{\partial\theta})\frac{1}{\sqrt{1+\delta^2}}+\right. \\
&\left.\frac{1}{R\sqrt{1+\delta^2}}\frac{\partial}{\partial r}\frac{R}{r}\frac{\partial}{\partial r}\frac{r}{\sqrt{1+\delta^2}} + \frac{\delta}{r\sqrt{1+\delta^2}}\frac{\partial}{\partial r}\frac{r}{R}\frac{\partial}{\partial r}\frac{R\delta}{\sqrt{1+\delta^2}}\right]E_\perp + \\
&\left[\frac{1}{R\sqrt{1+\delta^2}}(\frac{\partial}{\partial\varphi}+\frac{1}{q}\frac{\partial}{\partial\theta})\frac{1}{rR}(\delta^2 q\frac{\partial}{\partial\varphi}-\frac{\partial}{\partial\theta})\frac{R}{\sqrt{1+\delta^2}}+\right. \\
&\left.\frac{1}{R\sqrt{1+\delta^2}}\frac{\partial}{\partial r}\frac{R}{r}\frac{\partial}{\partial r}\frac{r\delta}{\sqrt{1+\delta^2}} - \frac{\delta}{r\sqrt{1+\delta^2}}\frac{\partial}{\partial r}\frac{r}{R}\frac{\partial}{\partial r}\frac{R}{\sqrt{1+\delta^2}}\right]E_\parallel \qquad (4.24)
\end{aligned}
$$

It is straightforward to show that the cylindrical limit of Eqs. (4.23) and (4.24) (i.e., with R replaced by R_0) is exactly the same as the cylindrical form as derived by Ross et al. (see Eq. (1) of Ref. 28). Following Ref. 28, we shall not make use of the parallel component of Ampere's law. Also, $E_\parallel$ can be eliminated in terms of E_r and $E_\perp$ by means of $\nabla \cdot \mathbf{J} = 0$:

$$
E_\parallel = -\frac{B}{\chi_{\parallel,\parallel}}(R^2\mathbf{B}\cdot\nabla)^{-1}\left(R^2\nabla\cdot(\boldsymbol{\chi}\cdot\mathbf{E})_\perp\right) \qquad (4.25)
$$

Notice that the operator $R^2\mathbf{B}\cdot\nabla = R_0B_0(\partial/\partial\varphi + \partial/q\partial\varphi)$ contains no toroidicity so we can invert it algebraically. In any case, we will neglect the toroidicity due to $E_\parallel$ terms since these are kinetic terms.

Eventually, we find that Eq. (4.22) can be rewritten in the same form as Eq. (4.2), but now the operator $\tilde{L}$ contains toroidal coupling. It can be expanded straightforwardly, with the inverse aspect ratio $\varepsilon = a/R$ as a small parameter:

$$
\tilde{L} = \tilde{L}_0 + \varepsilon\frac{r}{a}(2\cos\theta\tilde{L}_s + 2i\sin\theta\tilde{L}_A) \qquad (4.26)
$$

where $\tilde{L}_0$ is the cylindrical operator and is the same as given in Eq. (4.3), and $\tilde{L}_s$ and $\tilde{L}_A$ are given by:

$$
\begin{aligned}
(\tilde{L}_S)_{rr} &= -\frac{1}{R_0^2}\frac{\partial^2}{\partial\varphi^2} \\
(\tilde{L}_S)_{r\perp} &= -\frac{1}{2r^3}\frac{\partial}{\partial\theta}\frac{\partial}{\partial r}r^2\delta_0^2 - \frac{1}{R_0}\frac{\partial}{\partial\varphi}\frac{\partial}{\partial r}\frac{\delta_0}{\sqrt{1+\delta_0^2}} \\
(\tilde{L}_S)_{\perp r} &= -\frac{1}{2}\left(\frac{1}{\sqrt{1+\delta_0^2}} - \delta_0^2 + \frac{\delta_0^2}{r}\frac{\partial}{\partial r}\right)\frac{\partial}{\partial\theta} - \frac{\delta_0}{rR_0\sqrt{1+\delta_0^2}}\left(\frac{3}{2} + r\frac{\partial}{\partial r}\right)\frac{\partial}{\partial\varphi} \\
(\tilde{L}_S)_{\perp\perp} &= \frac{1}{2}\left[\delta_0^2\frac{\partial}{\partial r}\frac{1}{r}\frac{\partial}{\partial r}\frac{r}{\sqrt{1+\delta_0^2}} + \frac{1}{r\sqrt{1+\delta_0^2}}\frac{\partial}{\partial r}\frac{1}{r}\frac{\partial}{\partial r}r^2\delta_0^2\right. \\
&\quad + \frac{1}{r^2\sqrt{1+\delta_0^2}}\frac{\partial}{\partial r}\frac{r}{\sqrt{1+\delta_0^2}} - \frac{\delta_0}{r\sqrt{1+\delta_0^2}}\frac{\partial}{\partial r}\frac{\delta_0}{\sqrt{1+\delta_0^2}} \\
&\quad \left. - \frac{2\delta_0}{r\sqrt{1+\delta_0^2}}\frac{\partial}{\partial r}r\frac{\partial}{\partial r}\frac{\delta_0}{\sqrt{1+\delta_0^2}}\right] - \frac{1}{R_0^2}\left(\frac{\partial}{\partial\varphi} + \frac{1}{q}\frac{\partial}{\partial\theta}\right)^2 \\
(\tilde{L}_S)_{rr} &= \frac{i}{2r^2}\frac{\partial}{\partial\theta} \\
(\tilde{L}_A)_{r\perp} &= -\frac{i}{2}\left(\frac{1}{r^2}\frac{\partial}{\partial r}\frac{r}{\sqrt{1+\delta_0^2}} + \frac{1}{r^3}\frac{\partial}{\partial r}r^2\delta_0^2\right) \\
(\tilde{L}_A)_{\perp r} &= 0 \\
(\tilde{L}_A)_{\perp\perp} &= -\frac{i\delta_0}{4rR_0\sqrt{1+\delta^2}}\left(\frac{\partial}{\partial\varphi} + \frac{1}{q}\frac{\partial}{\partial\theta}\right)
\end{aligned}
$$

Under Fourier transformation and keeping only sideband coupling, we find that Eq. (4.22) then becomes an infinite set of coupled equations:

$$\hat{\varepsilon}(\tilde{L}_S + \tilde{L}_A)_{m-1}\tilde{E}_{m-1} + (\tilde{L}_0)_m\tilde{E}_m + \hat{\varepsilon}(\tilde{L}_S - \tilde{L}_A)_{m+1}\tilde{E}_{m+1} = 0 \qquad (4.27)$$

where $\hat{\varepsilon} = \varepsilon r/a$. In the limit of $\varepsilon \to 0$, Eq. (4.27) reduces to the cylindrical form, i.e., $\tilde{L}_{0m}\tilde{E}_m = 0$. For nonzero ε, we have an infinite series of coupled equations.

To truncate this infinite series, we consider only three poloidal modes. This is consistent with expanding only to first order in ε. Thus, we finally obtain the following six-by-six matrix of coupled second-order differential equations to be solved numerically:

$$\begin{pmatrix} (\tilde{L}_0)_{m-1} & \hat{\varepsilon}(\tilde{L}_S - \tilde{L}_A)_m & 0 \\ \hat{\varepsilon}(\tilde{L}_S + \tilde{L}_A)_{m-1} & (\tilde{L}_0)_m & \hat{\varepsilon}(\tilde{L}_S - \tilde{L}_A)_{m+1} \\ 0 & \hat{\varepsilon}(\tilde{L}_S + \tilde{L}_A)_m & (\tilde{L}_0)_{m+1} \end{pmatrix} \begin{pmatrix} \tilde{E}_{m-1} \\ \tilde{E}_m \\ \tilde{E}_{m+1} \end{pmatrix} = 0 \quad (4.28)$$

4.4 Numerical Results and Discussion

Here we consider two typical GAE modes for CIT parameters. Notice that the edge density is not zero in order to have finite Alfvén frequency at the edge. Also we choose the edge density to be small enough for a sideband resonance to exist. For the sake of comparison and of numerical calculation, we use ε as an independent variable in Eq. (4.28). Thus, for $\varepsilon = 0$, our calculation will recover the cylindrical eigenvalues. The known cylindrical eigenvalues will then provide us with very good guesses for the corresponding toroidal eigenvalues, which can be traced as the value of ε is increased.

4.4.1 Mode $(1, -2)$

Here we consider toroidicity effects on the cylindrical GAE $(1, -2)$ mode. Shown in Figs. 4.5–4.7 are the eigenfunctions for the main poloidal mode $(1, -2)$ and its two sidebands $(1, -1)$ and $(1, -3)$, for various values of the toroidicity parameter ε. Figure 4.8 shows both the Landau damping rate obtained without alpha particles, as well as the growth rate induced by alpha particles with $L_\alpha/a = 0.25$. Note that this alpha particle density scale length L_α corresponds to the maximum growth rate in the cylindrical limit, as shown

in Fig. 4.3(a).

The following observations emerge after examing these results:

(1) The structure of the sideband $(1, -1)$ near its Alfvén resonance has two distinctive types of behavior depending on the value of ε. For small $\varepsilon < 0.2$, the sideband $(1, -1)$ is like an Airy function and the mode propagates toward the center of the plasma. In fact, Stix [61] has shown that for $\beta_e/(m_e/m_i) > 1$ at the resonance, the essential evanescent compressional wave at the edge of the plasma will convert to a kinetic Alfvén wave, which propagates toward the high density region. Indeed our results confirm this physical process. Furthermore, as ε increases, we observe that the sideband resonance shifts toward the edge of the plasma. As a result, $\beta_e/(m_e/m_i)$ decreases and eventually becomes less than unity, at which point the KAW becomes the so-called cold surface Alfvén wave. Notice that the toroidal coupling will lower the $(1, -1)$ Alfvén continuum and therefore its resonance moves toward the outside as ε increases. Finally, for $\varepsilon = 0.48$, which corresponds to the CIT value, the $(1, -1)$ singularity simply disappears.

(2) More or less related to the above observations, we note that there are three distinct stages for the Landau damping rate γ_L and the growth rate γ induced by alpha particles. For small $\varepsilon < 0.1$, the sideband amplitudes scale roughly linearly with ε, and we have $\gamma_L \propto \varepsilon^2$ and $\gamma \propto \varepsilon^2$; for intermediate values of ε, $0.1 < \varepsilon < 0.2$, we have linear scaling $\gamma_L \propto \varepsilon$ and $\gamma \propto \varepsilon$; for still larger $\varepsilon > 0.25$, γ_L is eventually saturated and begins to decrease. Meanwhile, the trend for γ is exactly the opposite of that for γ_L.

Recall that the electron Landau damping rate for the localized KAW mode is much higher than that for the GAE modes. Thus the toroidal GAE mode, which is a mixture of the cylindrical GAE mode and a sideband KAW

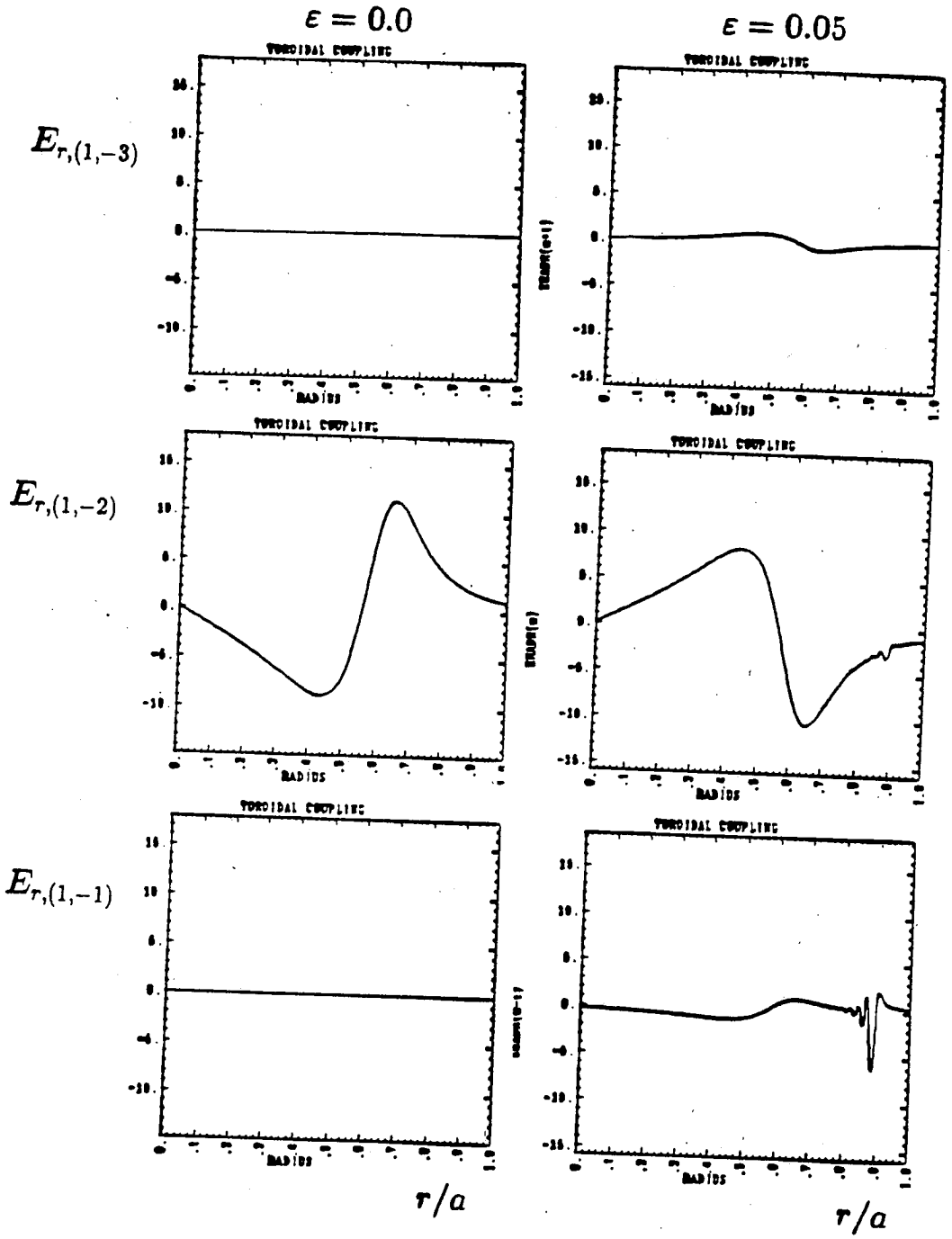

Figure 4.5: Numerical eigenfunctions for the toroidal global Alfvén eigenmode $(1,-2)$ and the sidebands $(1,-1)$ and $(1,-3)$, with CIT parameters, for inverse aspect ratio values of $\varepsilon = 0.0$ and $\varepsilon = 0.05$.

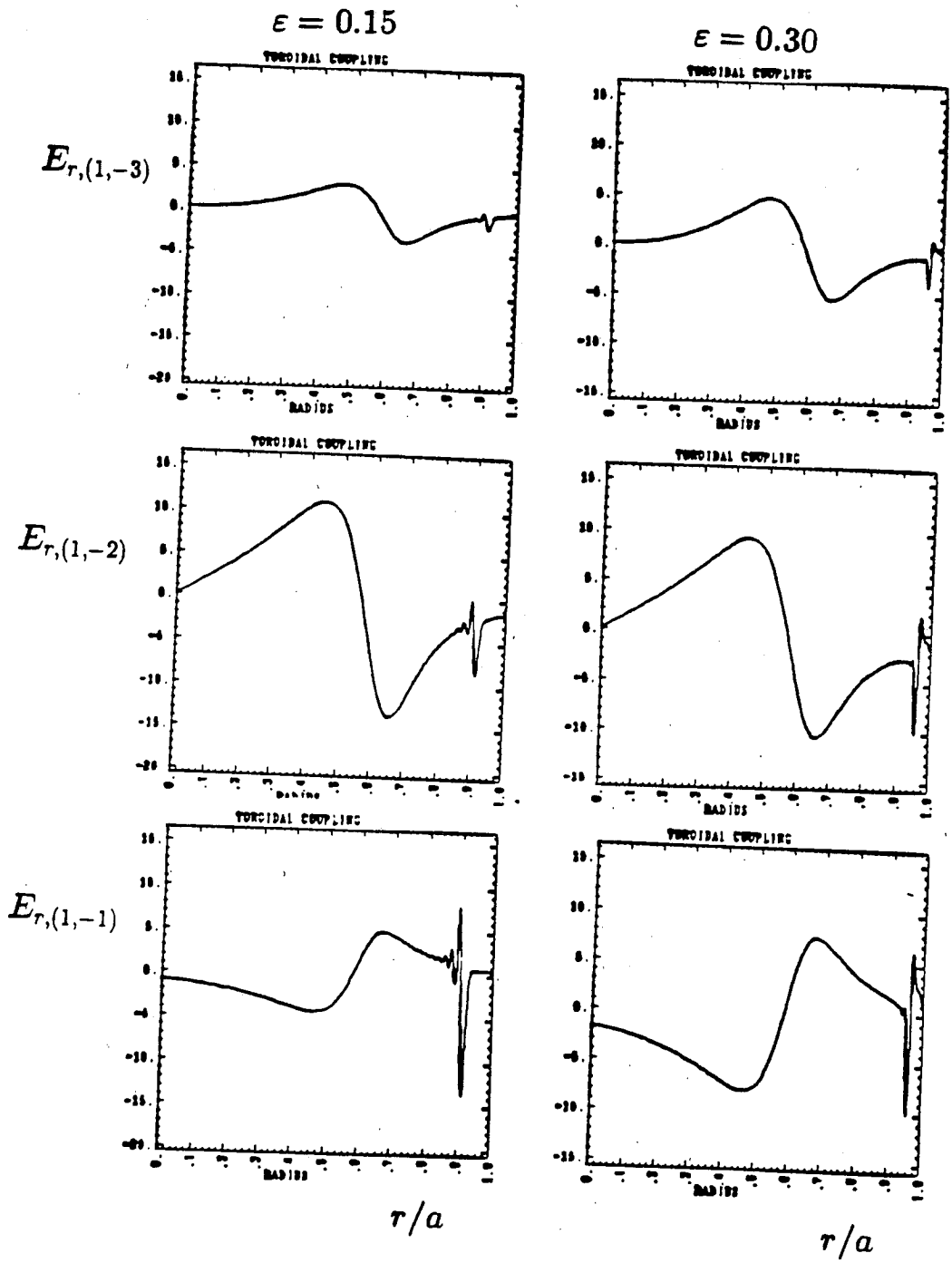

Figure 4.6: As in Fig. 4.5, but for $\varepsilon = 0.15$ and $\varepsilon = 0.30$.

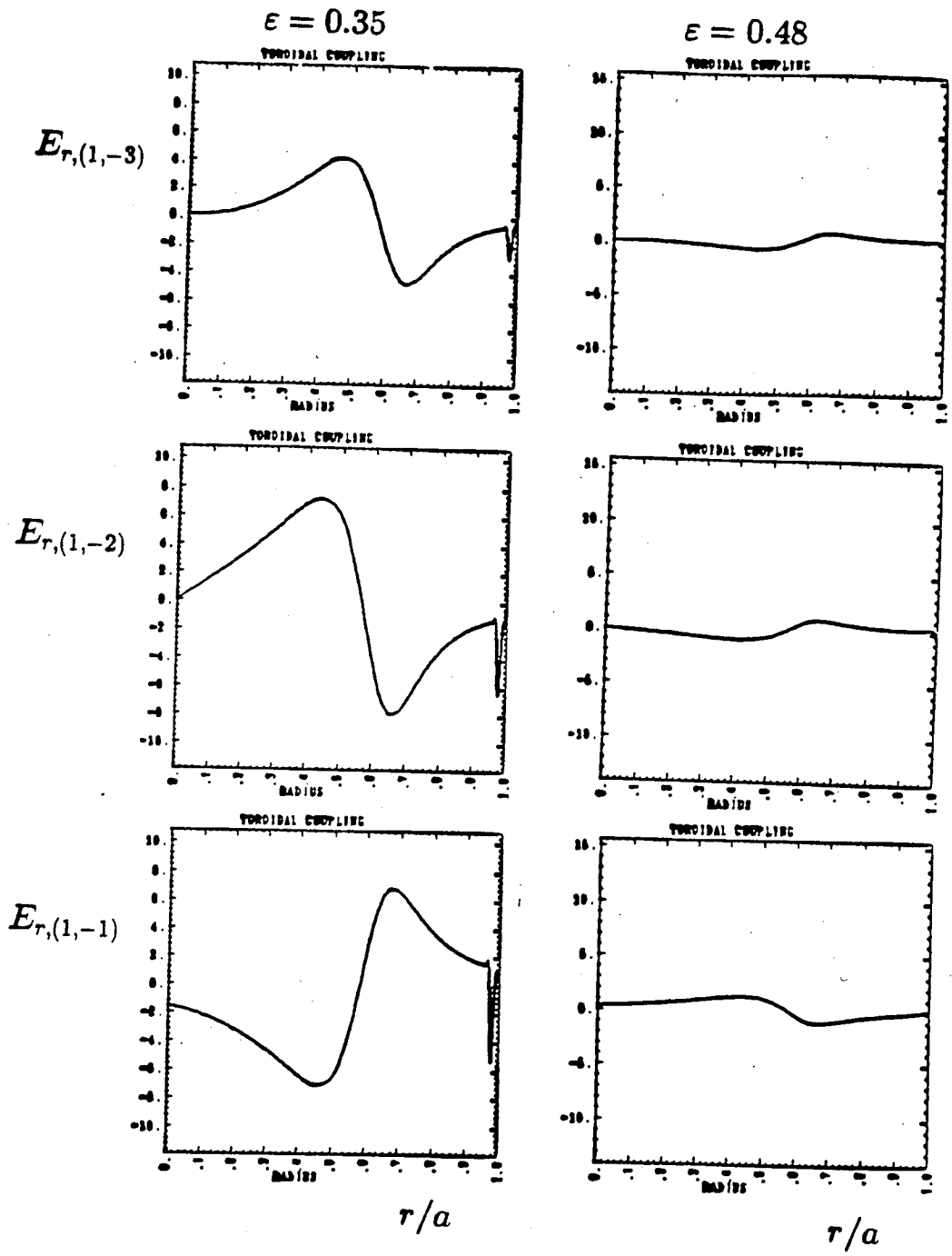

Figure 4.7: As in Fig. 4.5, but for $\varepsilon = 0.35$ and $\varepsilon = 0.48$.

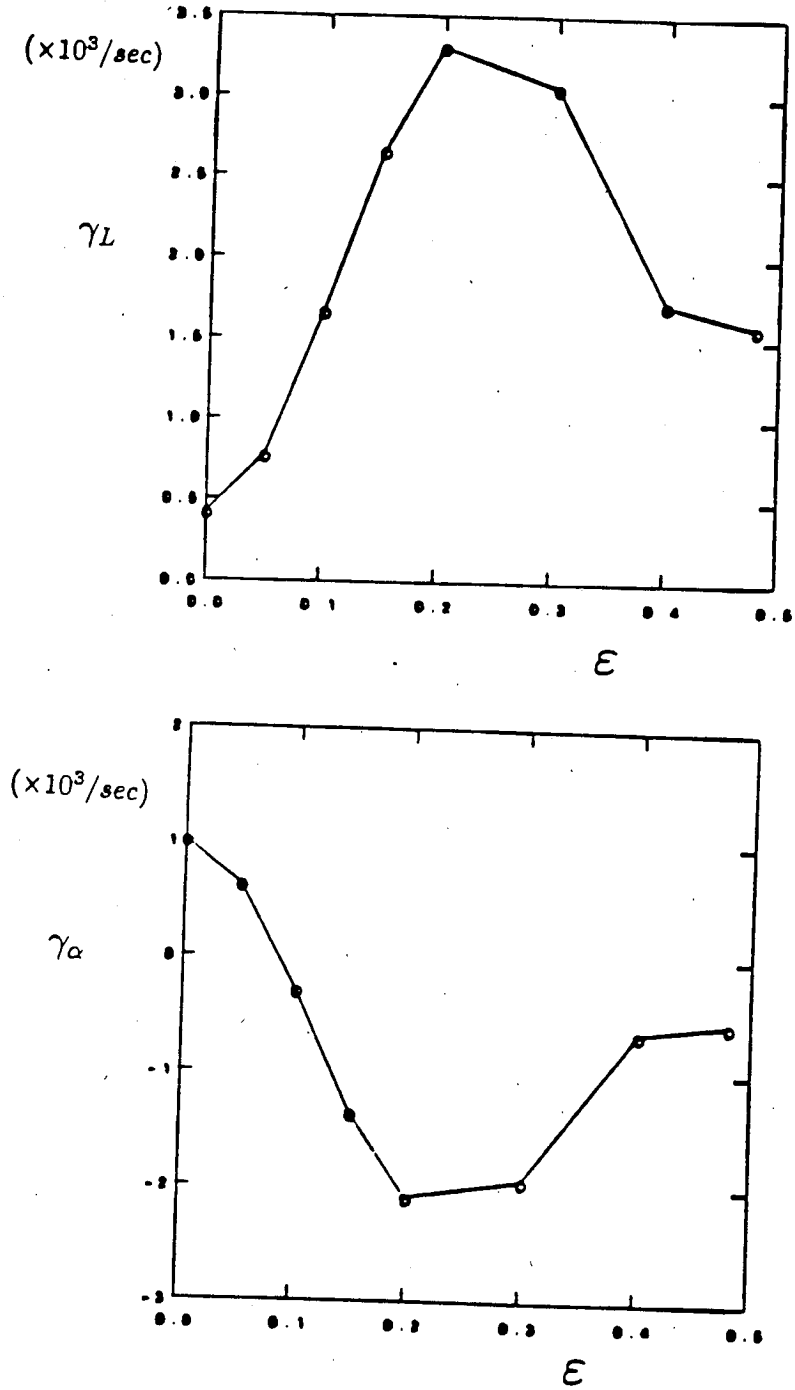

Figure 4.8: Electron Landau damping rate γ_L and alpha-induced growth rate γ_α as functions of the inverse aspect ratio ε for the global Alfvén eigenmode $(1,-2)$ coupled to the sidebands $(1,-1)$ and $(1,-3)$.

mode, has a greater damping rate. On the other hand, the KAW sideband should contribute little to the alpha destabilization since it is localized near the edge of the plasma where few alpha particles reside. Therefore, as ε increases, the electron Landau damping is enhanced and the alpha particle-induced growth rate decreases. For $\varepsilon = 0.1$, the mode is stabilized. However, as ε is raised further, the Landau damping begins to saturate and, eventually, to decrease; consequently, the stabilization through toroidal coupling is weakened. The reason for the reduction in the Landau damping is the shifting of the $(1, -1)$ resonance toward the edge of the plasma as ε increases; correspondingly, the coupling between the GAE mode and the KAW sideband is reduced. For the CIT value of $\varepsilon = 0.48$, the GAE mode is still stabilized. Moreover, the inclusion of the additional sideband $(1, 0)$ is expected to shift the $(1, -1)$ resonance toward the center of the plasma, as opposed to the $(1, -2)$ mode. Thus we expect the stabilizing effect to be further enhanced. Indeed, our numerical results confirm this. Shown in Fig. 4.9 is the electron Landau damping rate and the growth rate for the GAE $(1, -2)$ mode coupled to sidebands $(1, -1)$ and $(1, 0)$. The saturation of Landau damping is delayed until $\varepsilon = 0.4$.

At this time, it is instructive to apply quantum mechanics perturbation theory to our mode coupling problem. Previously the toroidal Alfvén modes had been constructed [62] analytically by a superposition of cylindrical eigenmodes in the ideal MHD limit. Here, however, all the kinetic effects are included in our eigen-equation. Our problem is similar to a quantum mechanical system in the following sense. Equation (4.28) can be seen as an eigenvalue equation, with the diagonal elements as the unperturbed operators and the off-diagonal elements as the perturbation. In the limit of $\varepsilon \to 0$ or zero perturbation, the eigenvalue of our system reduces to the unperturbed spectrum or the cylindrical spectrum. Making the analogy with quantum mechanics

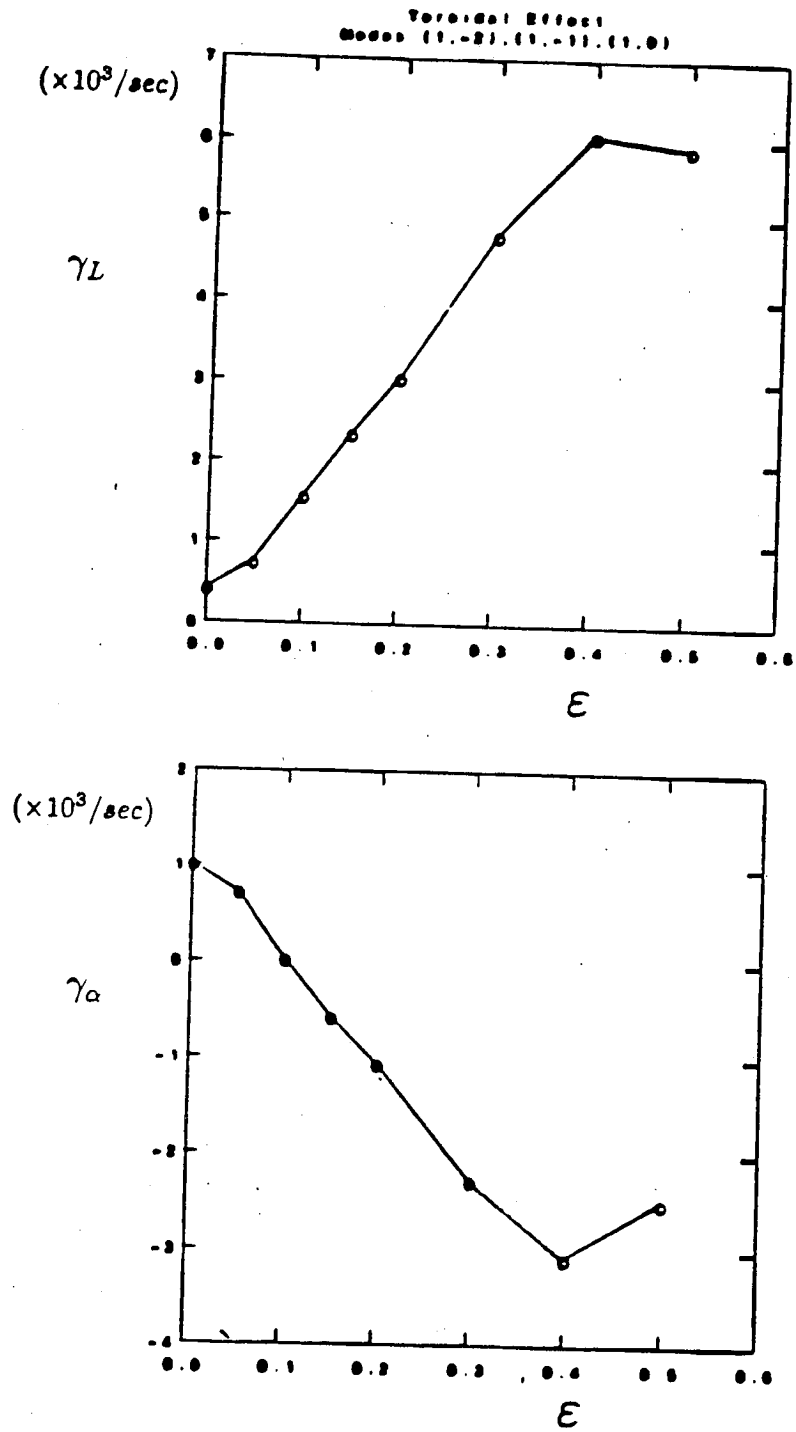

Figure 4.9: Electron Landau damping rate γ_L and alpha-induced growth rate γ_α as functions of the inverse aspect ratio ε for the global Alfvén eigenmode $(1,-2)$ coupled to the sidebands $(1,-1)$ and $(1,0)$.

perturbation theory, we can recover the scaling of the frequency shift and the sideband amplitude due to toroidal perturbation. For small ε, the unperturbed spectrum is non-degenerate; consequently the amplitude of the perturbed sideband is proportional to ε and the frequency shift $\delta\omega$ has the scaling $\delta\omega \propto \varepsilon^2$. As ε is increased, the spectrum becomes degenerate and we must invoke the method of degenerate perturbation theory. In this case, we have the scaling $\delta\omega \propto \varepsilon$. These analytic scalings agrees well with our numerical results.

4.4.2 Mode $(0, -2)$

Recall that this mode has been identified as the most unstable GAE mode for typical ignition parameters. Therefore, the toroidal effect on this mode is particularly interesting. Figure 8 shows the Alfvén continuum for this mode and its two sidebands, with a edge density 1.5% that of the center density. Note that the $(0, -1)$ sideband resonance is very close to the edge of the plasma. Figure 4.11–4.13 shows the numerical results for the eigenfunctions, the Landau damping rate, and the alpha-induced growth rate, with $L_\alpha/a = 0.4$, corresponding to the most unstable case in the cylindrical limit. We observe that the sideband $(0, -1)$ is similar to the cold surface Alfvén wave since $\beta_e/(m_e/m_i) < 1$ at the resonance. For the CIT value of $\varepsilon = 0.48$, the mode is completely stabilized. However, we found that the toroidicity effect in this particular case is somewhat sensitive to the edge parameters—especially the edge density—since the sideband resonance is very close to the edge. For example, with a 10% edge density, there is no sideband resonance, the existence of which is crucial to toroidicity stabilization. Shown in Fig. 4.14 is the growth rate for different values of the edge density. We found that for the CIT parameters, the mode remains unstable for 10% edge density, is marginally stable for

2%, and is completely stabilized for 1.5%. We conjecture that as long as the sideband resonance exists in the toroidal Alfvén continuum, the GAE mode is likely to be stabilized by the toroidal mode coupling.

4.5 Conclusion

In this chapter, we have shown that the unstable cylindrical global shear Alfvén waves excited by alpha particles can be stabilized by sideband electron Landau resonance damping for the parameters of CIT, as long as the mode frequency is embedded in the toroidal continuum. An exception is the $(0, -1)$ mode, whose sidebands have no resonance. However, the growth of this mode is small , so it might not be important for the nonlinear consequences. Furthermore, other stabilizing mechanisms, such as the curvature-induced electron Landau damping (similar to the alpha particle term considered here), could provide additional stabilition of this GAE modes. We also found that these toroidicity effects are somewhat sensitive to the details of the toroidal Alfvén continuum—in particular, the plasma edge condition. Therefore an extended study with a realistic tokamak equilibrium would be worthwhile for an accurate assessment of the stability of these modes in an ignited tokamak experiment.

The results of this chapter have several important implications. With regard to Alfvén wave heating, the sideband resonance may lead to substabtial edge heating, which is very unfavorable. In the case of tokamak divertor operation, the toroidal mode coupling is expected to be stronger and more complicated since the magnetic surfaces are elongated and a magnetic flux separatrix exists at the edge of the plasma. Much work is needed in this area. Another important aspect of toroidal coupling is the discrete gap mode with its frequency within the toroidicity-induced gaps in the Alfvén continuum. This

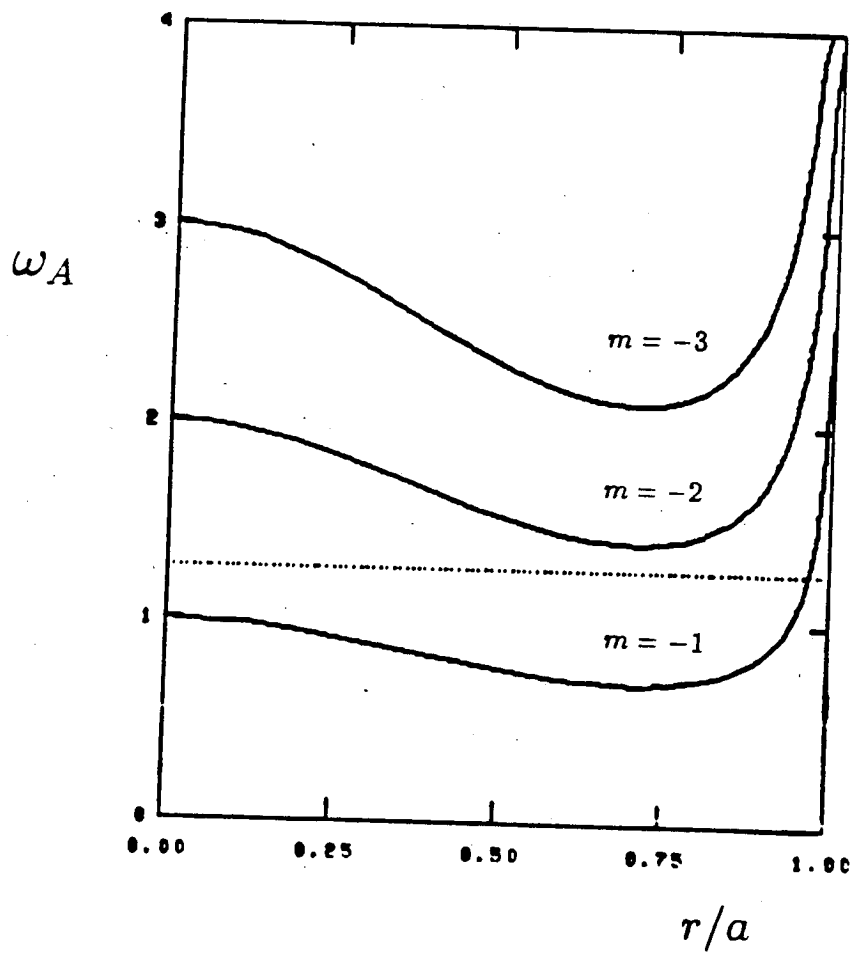

Figure 4.10: Cylindrical shear Alfvén continua for mode number $n = 0$ and $m = -1, -2$, and -3.

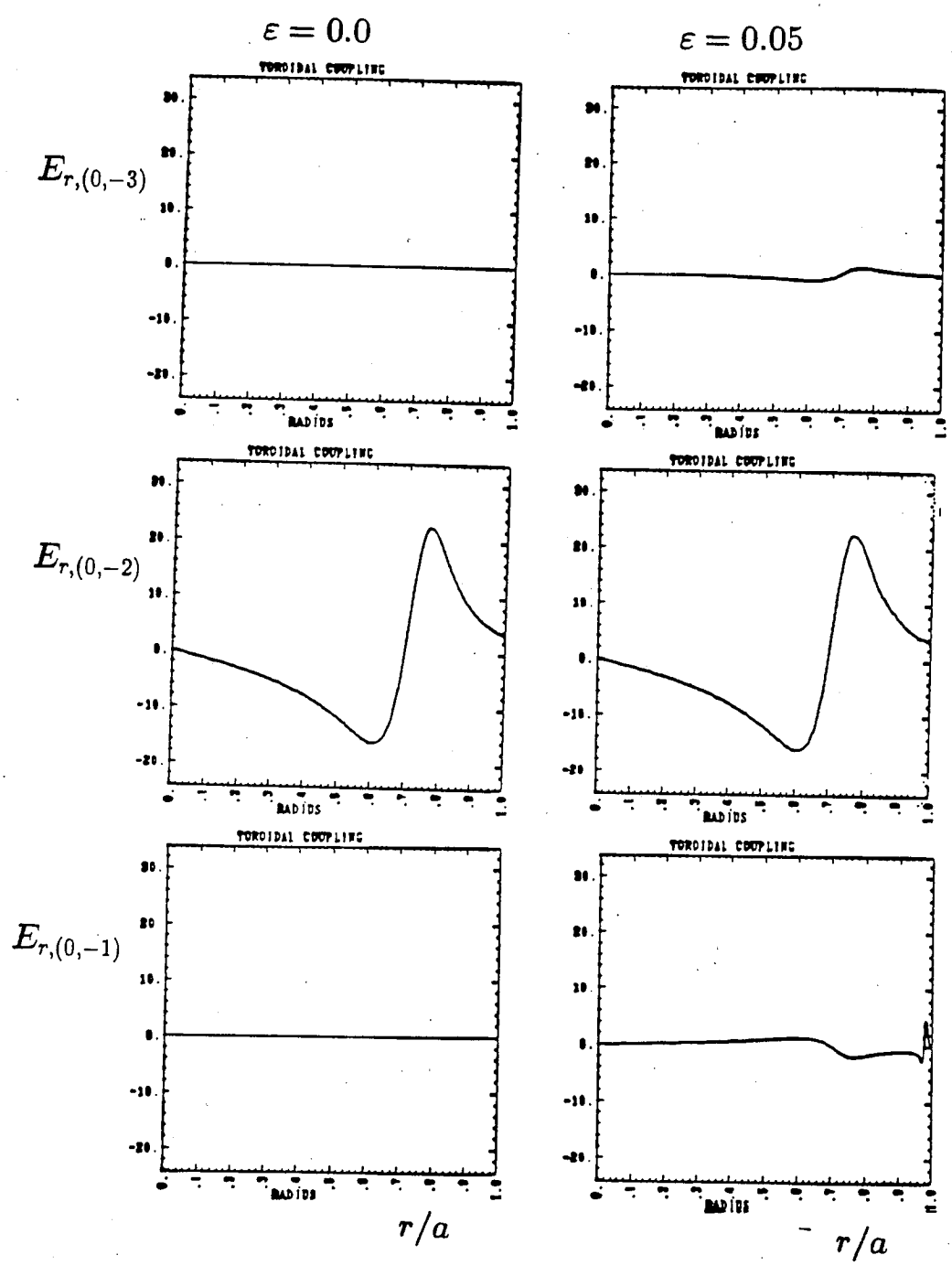

Figure 4.11: Numerical eigenfunctions for the toroidal global Alfvén eigenmode $(0,-2)$ and the sidebands $(0,-1)$ and $(0,-3)$, with CIT parameters, for the inverse aspect ratio values of $\varepsilon = 0.0$ and $\varepsilon = 0.05$.

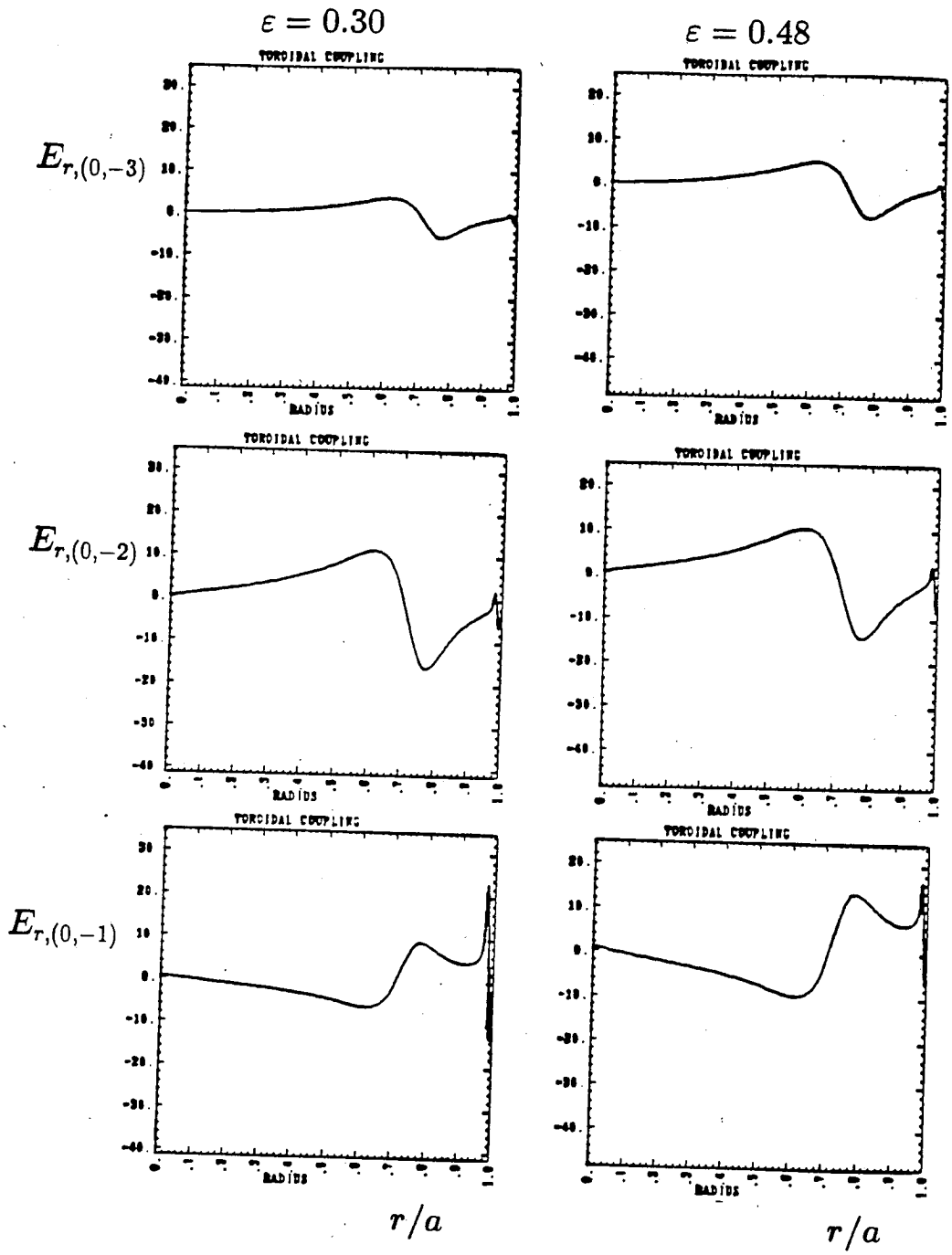

Figure 4.12: As in Fig. 4.11, but for $\varepsilon = 0.30$ and $\varepsilon = 0.48$.

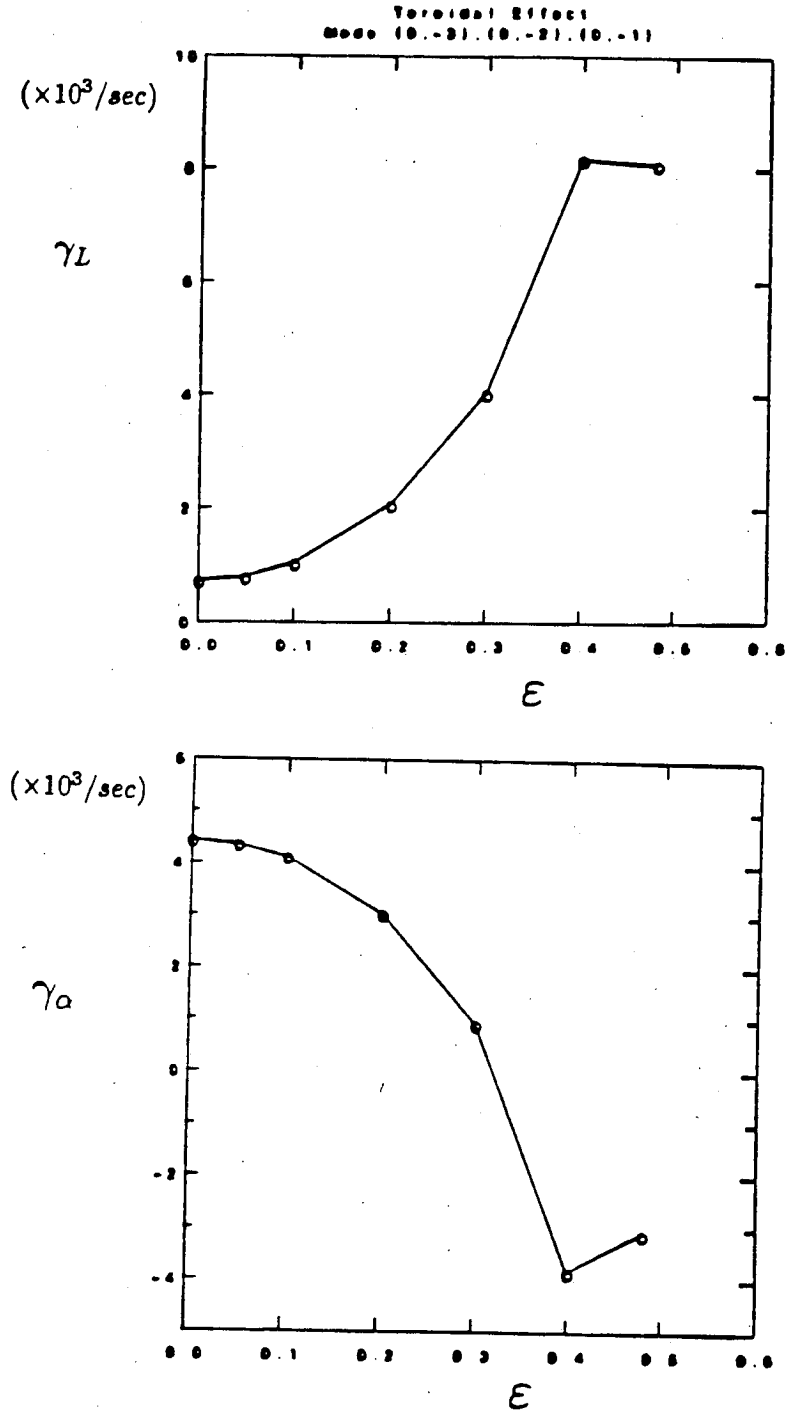

Figure 4.13: Electron Landau damping rate γ_L and alpha-induced growth rate γ_α as functions of the inverse aspect ratio ε for the global Alfvén eigenmode $(0,-2)$ coupled to the sidebands $(0,-1)$ and $(0,-3)$.

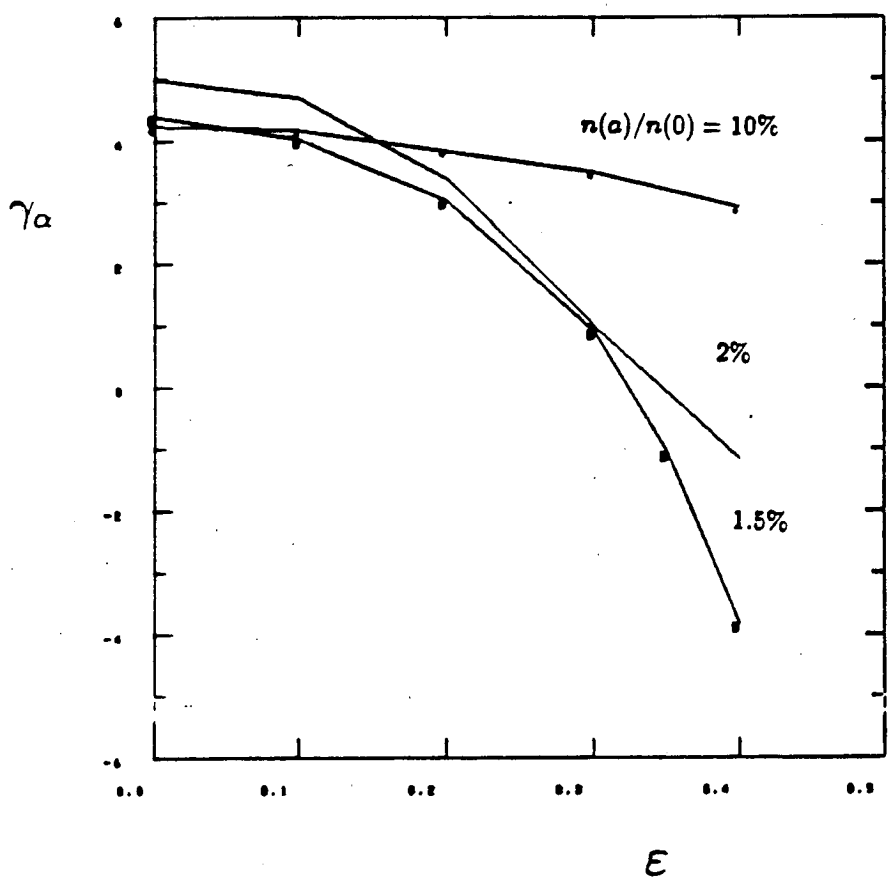

Figure 4.14: Growth rate γ_α for the global Alfvén eigenmode $(0, -2)$ coupled to the sidebands $(0, -1)$ and $(0, -3)$ as functions of the inverse aspect ratio ε for various values of the edge density.

new toroidal global mode has a parallel wave length that is typically longer than that of the cylindrical GAE mode, and therefore is more easily destabilized by alpha particles. We will study this gap mode in the next chapter.

Chapter 5

Destabilization of the Toroidicity-Induced Alfvén Gap Mode by Alpha Particles in an Ignited Tokamak

5.1 Introduction

In the preceeding chapter, the first type of global Alfvén wave was discussed in toroidal geometry. We found that the cylindrical global Alfvén eigenmodes (GAE) can be stabilized by toroidal effects in an ignited tokamak. In this chapter, we study the possibility of alpha particle destabilization of another type of global Alfvén eigenmode, namely, the toroidicity-induced shear Alfvén gap eigenmode (TAGE), whose frequency lies within the toroidicity-induced gaps in the Alfvén frequency continuum. Cheng and Chance [39] were the first to show the existence of the TAGE mode numerically and analytically. In this chapter, we will prove that the TAGE mode exists even when finite ion Larmor radius effects are included. Furthermore, we have found that these gap modes, as well as the cylindrical global modes, can be destabilized by alpha particles in an ignited plasma. Moreover, we find that the TAGE mode is actually more unstable than the GAE mode, over a wider range of value for the alpha particle density scale length, which is a measure of the available free energy.

Our consideration of the TAGE mode is motivated by the fact that the TAGE mode has a substantially longer parallel wavelength compared to that for the cylindrical GAE mode. Therefore, we expect the interaction between the alpha particles and the TAGE mode to be stronger. This comparison can

be clearly seen from a simple estimate of the alpha particle-induced growth rate, which scales as $\gamma \propto \beta_\alpha/(4k_\parallel^2 R^2)(\omega_{*\alpha} - \omega)$, where β_α is the alpha particle beta value, $k_\parallel$ is the parallel wave number, R is the major radius, and $\omega_{*\alpha}$ is the alpha particle diamagnetic frequency. It is evident that the global mode with the smallest $k_\parallel$ has the largest growth rate. Furthermore, we expect that the electron Landau damping of the TAGE mode is small, since the TAGE mode is intrinsically a global MHD kink-type mode, even though the TAGE is somewhat less global than the cylindrical GAE. Indeed, we found both analytically and numerically that the kinetic effects hardly modify the global structure of the TAGE mode and, as a result, the electron Landau damping is found to be negligibly small compared to the alpha-induced growth rate for the instability.

5.2 Eigenmode Equation

To incorporate the toroidal coupling correctly is the main concern in this section. Following Rosenbluth and Rutherford [35], we describe the dynamics by the linearized drift kinetic equation, using ϕ and $A_\parallel$ to represent the perturbed fields (this implies that $B_\parallel = 0$). We integrate the linearized drift kinetic equation over all velocities, multiply it by the charge e_s, and sum over all species (indexed by "s"), thus obtaining a moment equation for the perturbed current density:

$$\begin{aligned} &\mathbf{b}\cdot\nabla j_{\parallel 1} + \mathbf{b}_1\cdot\nabla j_\parallel + \sum_s e_s \int d^3v \mathbf{v}_{ds}\cdot\nabla f_{1s} \\ = \; & -\nabla\cdot[\frac{i\omega m_i n_i c^2}{B^2}(1+\frac{3}{4}\rho_i^2\nabla_\perp^2)\nabla_\perp\phi] \end{aligned} \tag{5.1}$$

Here $\mathbf{v}_{ds} = m_s c(\mu B + v_\parallel^2)/(e_s B^2)\mathbf{b}\times\nabla B$, $\mu = v_\perp^2/2B$, and ρ_i is the thermal ion gyroradius. The subscript "1" denotes perturbed quantities. Note that here we have neglected the alpha particle contribution to the polarization current,

owing to the orderings $n_\alpha << n_i$ and $\beta_\alpha << \beta_i$. However, the perturbed alpha current caused by the equilibrium magnetic field ∇B and curvature drift velocity $\mathbf{v}_{ds}$ is retained, due to the very high energy of the alpha particles. With the help of Ampere's law, one can rewrite Eq. (5.1) in terms of $A_\parallel$ and ϕ:

$$\mathbf{b}\cdot\nabla\nabla_\perp^2(-\frac{c}{4\pi}A_\parallel)+\frac{\mathbf{b}\times\nabla A_\parallel}{B}\cdot\nabla j_\parallel$$
$$+\quad\nabla\cdot[\frac{i\omega m_i n_i c^2}{B^2}(1+\frac{3}{4}\rho_i^2\nabla_\perp^2)\nabla_\perp\phi]+\sum_s e_s\int d^3v\mathbf{v}_{ds}\cdot\nabla f_{1s}=0 \quad (5.2)$$

Another equation for $A_\parallel$ and ϕ can be obtained from the quasi-neutrality condition, with the use of the gyro-kinetic equation:

$$\mathbf{b}\cdot\nabla\phi-\frac{i\omega}{c}A_\parallel=\mathbf{b}\cdot\nabla\frac{\tau\rho_i^2}{1+\zeta_e Z(\zeta_e)}\nabla_\perp^2\phi \quad (5.3)$$

where $\tau=T_e/T_i$, $\zeta_e=\omega/|k_\parallel|v_e$ for electrons, and Z is the plasma dispersion function. We have ignored the contribution of the alpha particles in Eq. (5.3) because $n_\alpha << n_i$ and $T_\alpha >> T_i$. After eliminating $A_\parallel$ in Eqs. (5.2) and (5.3), we obtain the following eigen-equation for ϕ:

$$\rho_i^2\nabla_\perp^2[\frac{3}{4}\frac{\omega^2}{v_A^2}+(\mathbf{b}\cdot\nabla)^2\frac{\tau}{1+\zeta_e Z(\zeta_e)}]\nabla_\perp^2\phi+\mathbf{b}\cdot\nabla\nabla_\perp^2\mathbf{b}\cdot\nabla\phi$$
$$-\frac{\mathbf{b}\times\nabla(\mathbf{b}\cdot\nabla\phi)}{B}\cdot\nabla(\frac{c}{4\pi}j_\parallel)+\nabla\cdot\frac{\omega^2}{v_A^2}\nabla_\perp\phi$$
$$=\frac{i4\pi\omega}{c^2}e_\alpha\int d^3v\mathbf{v}_{ds}\cdot\nabla f_{1s} \quad (5.4)$$

Here we have assumed $\partial/\partial r >> 1/L_s$, with L_s being the equilibrium scale length.

For simplicity, we assume concentric magnetic flux surfaces and adopt the following toroidal coodinates:

$$\begin{cases} x=R\cos(-\varphi)\\ y=R\sin(-\varphi)\\ z=r\sin\theta\\ R=R_0+r\cos\theta\end{cases}$$

In terms of these coodinates, the representations for the operators $\mathbf{b}\cdot\nabla$, $\nabla_\perp^2$, and $\nabla\cdot F\nabla_\perp$ are given as follows:

$$\mathbf{b}\cdot\nabla = \frac{1}{R}(\frac{\partial}{\partial\phi}+\frac{1}{q}\frac{\partial}{\theta}) \tag{5.5}$$

$$\nabla_\perp^2 = \frac{1}{rR}\frac{\partial}{\partial r}rR\frac{\partial}{\partial r}+\frac{1}{R}\frac{\partial}{\partial\theta} \tag{5.6}$$

$$\nabla\cdot F\nabla_\perp = \frac{1}{rR}\frac{\partial}{\partial r}rRF\frac{\partial}{\partial r}+\frac{1}{R}\frac{\partial}{\partial\theta}RF\frac{\partial}{\partial\theta} \tag{5.7}$$

Here F is a arbitrary function of r and θ. Notice that Eq. (5.4) contains the toroidicity through these operators, since $R = R_0 + r\cos\theta$, and through B and v_A, since $v_A \propto B \propto 1/R$. In general, all the terms in Eq. (5.4) contain some toroidicity. Here, we keep only the mode coupling due to the term $\nabla\cdot\frac{\omega^2}{v_A^2}\nabla_\perp\phi$ for simplicity. It turns out that this term is dominant in the formation of the continuum gap since it is a second-order radial derivative operator.

Now we can expand the toroidicity in this term to first order in a/R. After some straightforward algebra, we obtain the following infinite series of coupled eigen-equations:

$$L_\varepsilon E_{m-1} + (L_{k,m} + L_{0,m} + L_{\alpha,m})E_m + L_\varepsilon E_{m+1} = 0 \tag{5.8}$$

where $L_{k,m}$, $L_{0,m}$, L_ε and $L_{\alpha,m}$ are the differential operators for the kinetic term, the cylindrical MHD term, the toroidal coupling term, and the alpha particle term, respectively. The subscript m is the poloidal mode number. These operators are defined as follows:

$$L_{k,m} = r^2\nabla_\perp^2\rho_i^2(\frac{3}{4}\frac{\omega^2}{v_A^2}+\frac{\tau k_{\|m}^2}{1+\zeta_e Z(\zeta_e)})\nabla_\perp^2 r \tag{5.9}$$

$$L_{0,m} = \frac{d}{dr}r^3(\frac{\omega^2}{v_A^2}-k_{\|m}^2)\frac{d}{dr}-(m^2-1)r(\frac{\omega^2}{v_A^2}-k_{\|m}^2)+(\frac{\omega^2}{v_A^2})'r^2 \tag{5.10}$$

$$L_\varepsilon = \hat{\varepsilon}\frac{d}{dr}\frac{\omega^2}{v_A^2}\frac{r^4}{a}\frac{d}{dr} \tag{5.11}$$

$$L_{\alpha,m} = \frac{d}{dr}r^2A_\alpha\frac{d}{dr}-(m^2-1)rA_\alpha+A_\alpha' r^2+B_\alpha' mr^2 \tag{5.12}$$

where $\hat{\epsilon} = 3a/2R_0$. The form for A_α and B_α has been derived by Li, Mahajan, and Ross [37] by who solved the linearized drift kinetic equation for the alpha particles as follows:

$$A_\alpha = Q_{m-1} + Q_{m+1} \tag{5.13}$$

$$B_\alpha = Q_{m-1} - Q_{m+1} \tag{5.14}$$

$$Q_{m\pm1} = -i\frac{\beta_\alpha}{2R^2}\frac{c^2}{\omega^2}\left(P_{m\pm1} - \frac{\omega_{*\alpha m}}{\omega}R_{m\pm1}\right) \tag{5.15}$$

$$P_{m\pm1} = \frac{\pi\omega}{v_\alpha^4}\int d^3v\left(v_\perp^2/2 + v_\parallel^2\right)^2\left(-T_\alpha\frac{\partial f_{\alpha 0}}{\partial\epsilon}\right)\delta(\omega - k_\parallel v_\parallel) \tag{5.16}$$

$$R_{m\pm1} = \frac{\pi\omega}{v_\alpha^4}\int d^3v\left(v_\perp^2/2 + v_\parallel^2\right)^2 f_{\alpha 0}\delta(\omega - k_\parallel v_\parallel) \tag{5.17}$$

where $v_\alpha^2 = 2T_\alpha/m_\alpha$.

In general, two poloidal Fourier components of the gap eigenmode dominate over the other components, since the gap in the continuum spectrum is formed due to the toroidal perturbation of two degenerate cylindrical continua. For example, the toroidal coupling of poloidal modes (n, m) and $(n, m+1)$ would form a gap at $q = (2m+1)/2n$. Therefore, we consider here only two poloidal components, (n, m) and $(n, m+1)$, and neglect all others for simplicity. Then our infinite series of coupled equations reduces to the following two coupled eigen-equations:

$$\begin{aligned}(L_{k,m} + L_{0,m} + L_{\alpha,m})E_m + L_\varepsilon E_{m+1} &= 0\\ L_\varepsilon E_m + (L_{k,m+1} + L_{0,m+1} + L_{\alpha,m+1})E_{m+1} &= 0\end{aligned} \tag{5.18}$$

5.3 Destabilization of Toroidicity-Induced Shear Alfvén Gap Mode by Alpha Particles

In this section, we study the formation of the toroidicity-induced gaps in the shear Alfvén continuum and the existence of the gap eigenmodes within

these gaps, using the toroidal shear Alfvén eigenmode equations derived in the preceeding section. Previously the gap eigenmodes were discovered by Cheng and Chance [39] through a numerical calculation of the full MHD equations and also through an analytic analysis of the reduced MHD equation,[66]. Here, in addition to re-examining these gap modes using our shear Alfvén eigen-equations, we will also study the kinetic effects of the background cold plasma on these gap modes. Most significantly, we shall also study the destabilizing effect of alpha particles on these modes, in particular, for the parameters of the proposed Compact Ignition Tokamak (CIT). The parameters for the CIT device are given in Table 4.1. For simplicity we assume a constant plasma density profile. The profile for the safety factor q and the alpha particle density are taken to be $q = 1 + (r/a)^2$ and $n_\alpha = n_{\alpha 0}\exp(-r^2/L_\alpha^2)$, respectively.

5.3.1 Gap Eigenmodes in the MHD Limit

Here we consider the MHD limit of our coupled eigen-equations, given in Eq. (5.18). Dropping the kinetic terms and the alpha particle terms terms, we find that Eq. (5.18) becomes:

$$\begin{aligned}
&\left[\frac{d}{dr}r^3(\frac{\omega^2}{v_A^2} - k_{\|_m}^2)\frac{d}{dr} - (m^2-1)r(\frac{\omega^2}{v_A^2} - k_{\|_m}^2) + (\frac{\omega^2}{v_A^2})'r^2\right]E_m \\
&+\hat{\varepsilon}\frac{d}{dr}\frac{\omega^2}{v_A^2}\frac{r^4}{a}\frac{d}{dr}E_{m+1} = 0 \\
&\left[\frac{d}{dr}r^3(\frac{\omega^2}{v_A^2} - k_{\|_{m+1}}^2)\frac{d}{dr} - (m+1^2-1)r(\frac{\omega^2}{v_A^2} - k_{\|_{m+1}} + (\frac{\omega^2}{v_A^2})'r^2\right]E_{m+1} \\
&+\hat{\varepsilon}\frac{d}{dr}\frac{\omega^2}{v_A^2}\frac{r^4}{a}\frac{d}{dr}E_m = 0
\end{aligned} \tag{5.19}$$

In the cylindrical limit $\hat{\varepsilon} \to 0$, the two poloidal modes are naturally decoupled and we have two cylindrical continua, $\omega_1^2 = k_{\|_m}^2 v_A^2$ and $\omega_2^2 = k_{\|_{m+1}}^2 v_A^2$. For nonzero $\hat{\varepsilon}$, the continuum is determined by the determinant of the coefficients

of the second-order derivative terms being zero:

$$\begin{vmatrix} r^3(\frac{\omega^2}{v_A^2} - k_{\|_m}^2 v_A^2) & \hat{\varepsilon}\frac{\omega^2}{v_A^2}\frac{r^4}{a} \\ \hat{\varepsilon}\frac{\omega^2}{v_A^2}\frac{r^4}{a} & r^3(\frac{\omega^2}{v_A^2} - k_{\|_{m+1}}^2 v_A^2) \end{vmatrix} = 0 \tag{5.20}$$

Eq. (5.20) has two roots, which define two branches of $n = 1$ toroidal continua:

$$\omega_\pm^2 = \frac{k_{\|_m}^2 v_A^2 + k_{\|_{m+1}}^2 v_A^2 \pm \sqrt{(k_{\|_m}^2 v_A^2 - k_{\|_{m+1}}^2 v_A^2)^2 + 4\hat{\varepsilon}^2 x^2 k_{\|_m}^2 v_A^2 k_{\|_{m+1}}^2 v_A^2}}{2(1 - \hat{\varepsilon}^2 x^2)}$$

where $x = r/a$. For $n = -1$ and $m = -2$, we have a crossing of two cylindrical continua, $k_{\|_m}^2 v_A^2 = k_{\|_{m+1}}^2 v_A^2$, at $q = 1.5$, where a gap is formed whose width is given by

$$\Delta\omega = \omega_+ - \omega_- \approx \hat{\varepsilon}|k_{\|_m} v_A|_{q=1.5} \tag{5.21}$$

Shown in Fig. 5.1 is the toroidal continuum (solid curve) and the cylindrical continuum (dotted curve). We numerically solved Eq. (5.19) using the shooting method and obtained the TAGE mode eigenfrequency $\omega_0 = 0.89|k_{\|_m} v_A|_{q=1.5}$, which is well within the gap. The eigenfunction is shown in Fig. 5.2.

5.3.2 Kinetic Effects

Here we study whether finite Larmor radius effects will modify the global structure of the MHD gap eigenmode. To begin with, it is convenient to rewrite our coupled Eq. (5.18) into the following compact matrix form:

$$\begin{aligned} &(\tilde{L}_k + \tilde{L}_M + \tilde{L}_\alpha)\tilde{E} \\ \equiv &\begin{pmatrix} L_{k,m} + L_{0,m} + L_{\alpha,m}\ , & L_\varepsilon \\ L_\varepsilon\ , & L_{k,m+1} + L_{0,m+1} + L_{\alpha,m+1} \end{pmatrix} \begin{pmatrix} E_m \\ E_{m+1} \end{pmatrix} = 0 \end{aligned} \tag{5.22}$$

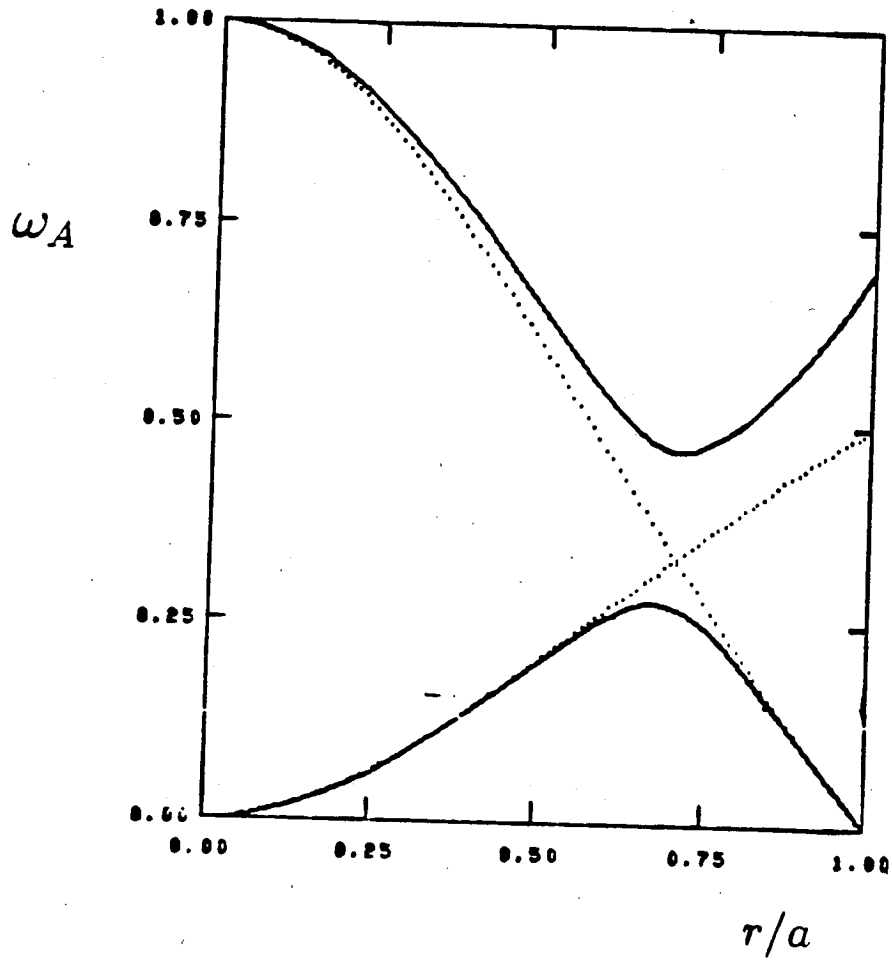

Figure 5.1: Shear Alfvén continuous spectrum with gap, for safety factor profile $q = 1 + (r/a)^2$ and a constant density profile; the uncoupled spectrum (dotted line) for $n = -1$ and $m = -1$ and $m = -2$ cross at the surface where $q = 1.5$.

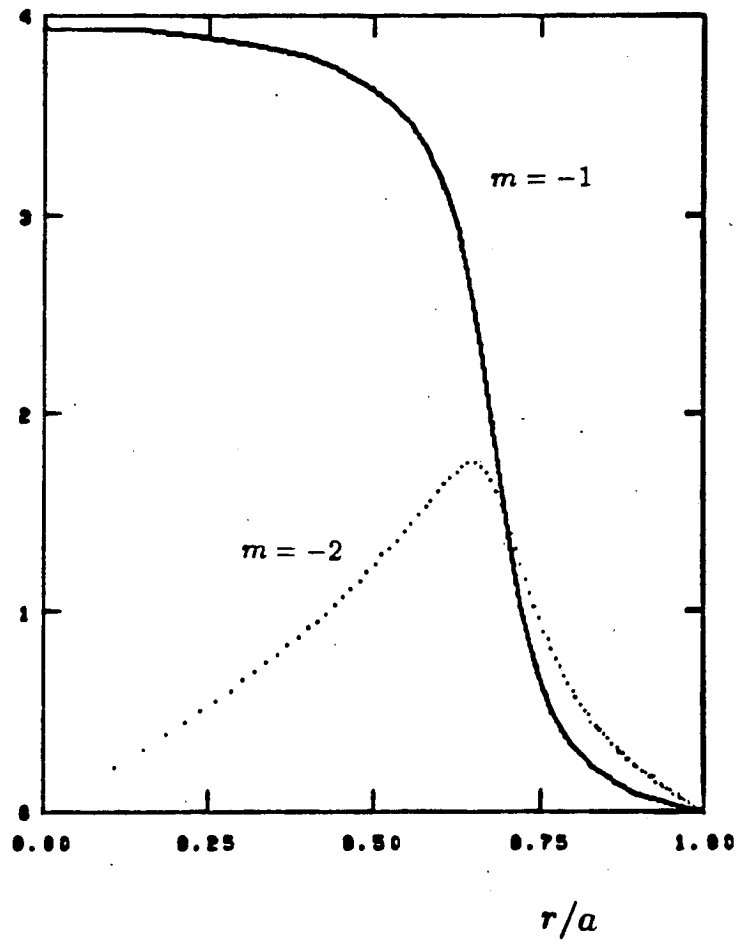

Figure 5.2: Poloidal harmonics for the $n = -1$ shear Alfvén gap eigenmode versus radius, for the same profiles as in Fig. 5.1.

where $\tilde{L}_k$, $\tilde{L}_M$, and $\tilde{L}_\alpha$ correspond to the matrix operators for the kinetic effect, the MHD equation, and the alpha particle response, respectively, and are defined as follows:

$$\tilde{L}_k = \begin{pmatrix} L_{k,m} & 0 \\ 0 & L_{k,m+1} \end{pmatrix} \quad , \quad \tilde{L}_M = \begin{pmatrix} L_{0,m} & L_\varepsilon \\ L_\varepsilon & L_{0,,m+1} \end{pmatrix}$$

$$\tilde{L}_\alpha = \begin{pmatrix} L_{\alpha,m} & 0 \\ 0 & L_{\alpha,m+1} \end{pmatrix} \quad , \quad \tilde{E} = \begin{pmatrix} E_m \\ E_{m+1} \end{pmatrix}$$

Here we drop the alpha particle term temporarily, since we wish to consider only the kinetic effects from the background cold plasma. Then Eq. (5.22) becomes

$$\tilde{L}_M \tilde{E} + \tilde{L}_k \tilde{E} = 0 \tag{5.23}$$

Eq. (5.23) can be solved perturbatively, assuming the kinetic effects are small. Of course this assumption should be verified a *posteriori* in order to have a self-consistent solution. Now expand $\tilde{E}$ around the MHD eigensolution $\tilde{E}_0$ as $\tilde{E} = \tilde{E}_0 + \delta\tilde{E}$; then we have

$$\tilde{L}_M \delta\tilde{E} = -\tilde{L}_k \tilde{E}_0 \tag{5.24}$$

Shown in Fig. 5.3 is the numerical result for $\delta\tilde{E}$ at $\omega = \omega_0$. We observe that $\delta\tilde{E}$ is negligibly small compared to the MHD eigenfunction $\tilde{E}_0$. Thus our assumption of a perturbative kinetic effect is confirmed.

This assumption can also be verified analytically. Using $\hat{\varepsilon}$ as a small parameter, the MHD equation $\tilde{L}_M \tilde{E}_0 = 0$ can be solved analytically near $q = (2m+1)/2n$. The scale length for $\tilde{E}_0$ is found to be

$$\Delta_r = \sqrt{\frac{\hat{\varepsilon}^2\Omega^2 - (1-\Omega^2)^2(1+\frac{1}{4m(m+1)})}{16m(m+1)}} \cdot \frac{r_0}{s} \tag{5.25}$$

Here $\Omega = (\omega_0/k_{\|}v_A)_{r=r_0}$ and S=rdq/qdr is the shear at $r = r_0$, with r_0 the radius where $q(r_0) = (2m+1)/2n$. Now insert this analytic MHD solution into Eq. (5.22) and compare the kinetic term to the MHD term:

$$\frac{L_k}{L_\varepsilon} \sim \frac{r_0^3\rho_i^2/\Delta_r^4}{\hat{\varepsilon}r_0^4/(a\Delta_r^2)} = \left(\frac{\rho_i/a}{\sqrt{\hat{\varepsilon}}r_0\Delta_r/a^2}\right)^2 \tag{5.26}$$

Using the values of $\Omega^2 = 0.78$, $r_0 = 0.7a$, and $\hat{\varepsilon}r_0/a = 0.5$, which correspond to the parameters used in the proceeding section, we have $\sqrt{\hat{\varepsilon}}r_0\Delta_r/a^2 \approx 0.05$. Therefore the kinetic effect is small if $\rho_i/a << 0.05$. This condition is well satified for typical ignition tokamak parameters; in particular, for CIT, we have $\rho_i/a \approx 4 \times 10^{-3}$ and, accordingly, $L_k/L_\varepsilon \sim 10^{-2}$. We then conclude that the kinetic term is negligibly small and will not modify the global structure of the MHD gap modes.

With the knowlege that the kinetic effects are small, we now proceed to calculate the electron Landau damping rate of the gap mode perturbatively. Expanding Eq. (5.23) to first order, we have

$$\tilde{L}_M\delta\tilde{E} + \frac{\partial\tilde{L}_M}{\partial\omega}\delta\omega\tilde{E}_0 + \tilde{L}_k\tilde{E}_0 = 0 \tag{5.27}$$

The MHD operator $\tilde{L}_M$ is self-adjoint in the following sense. For arbitrary fields $\tilde{E}_1$ and $\tilde{E}_2$, we have

$$\langle\tilde{E}_1^+\tilde{L}_M\tilde{E}_2\rangle = \langle\tilde{E}_2^+\tilde{L}_M\tilde{E}_1\rangle \tag{5.28}$$

where we have defined $\tilde{E}^+ = (E_m, E_{m+1})$ and $\langle\cdots\rangle = \int(\cdots)dr$. The surface term is taken to be zero because of the boundary conditions. Exploiting this property, we multiply both sides of Eq. (5.27) by $\tilde{E}_0^+$ and integrate over the radius to obtain

$$\delta\omega = -\frac{\langle\tilde{E}_0^+\tilde{L}_k\tilde{E}_0\rangle}{\langle\tilde{E}_0^+\frac{\partial\tilde{L}_M}{\partial\omega}\tilde{E}_0\rangle} \tag{5.29}$$

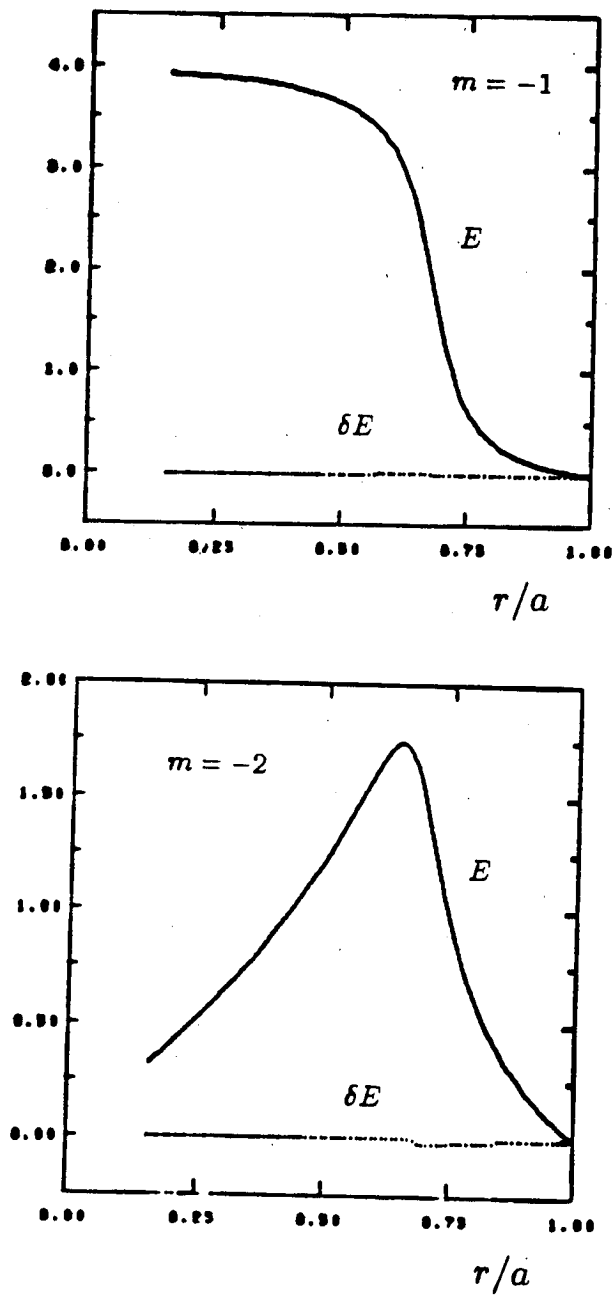

Figure 5.3: Poloidal harmonics for the $n = -1$ shear Alfvén gap eigenmode: shown are the MHD solution (E) and the kinetic correction (δE), versus radius for the same profile as in Fig. 5.1.

Numerically, we obtain the Landau damping rate $\gamma = 10^2$ sec^{-1}. This damping rate is small, even compared to the cylindrical global eigenmode. Initially we had expected that the damping rate of the gap mode would be at least larger than that for the cylindrical global mode, since the gap mode is somewhat less global. Recall, however, that $\gamma \propto \rho_i^2 \nabla_\perp^2$. For the gap mode, the gradient $\nabla_\perp^2$ falls off rapidly away from the peak of the mode, and the average of $\nabla_\perp^2$ should yield a relatively small value. Thus, the smallness of the damping rate does appear to be reasonable.

5.3.3 Alpha-Induced Growth Rate

The growth rate of the gap mode induced by the alpha particles can be calculated in a manner similar to that used for obtaining the electron Landau damping rate. Once again exploiting the self-adjointness of the MHD equation, we have

$$\gamma_\alpha = i \frac{\langle \tilde{E}_0^+ \tilde{L}_\alpha \tilde{E}_0 \rangle}{\langle \tilde{E}_0^+ \frac{\partial \tilde{L}_M}{\partial \omega} \tilde{E}_0 \rangle} \tag{5.30}$$

Shown in Fig. 5.4 is the alpha-induced growth rate γ_α (dotted curve) versus the alpha particle density scale length L_α. As a useful comparison, we have also plotted, as a solid curve, the growth rate for the most unstable cylindrical global eigenmode $(0, -2)$. We observe that the gap mode is substantially more unstable over a wider range of scale lengths. For the expected CIT value of $L_\alpha/a \approx 0.4$, we have $\gamma_\alpha \approx 10^4$ sec^{-1} for the gap mode, which is about three times larger than the growth rate for the cylindrical $(0, -2)$ mode. To gain further physical insight, we can estimate analytically the ratio of the growth rate for the gap mode to that of the cylindrical (0,-2) global mode. From

Eq. 4.12, we obtain the following scaling:

$$\gamma_\alpha \propto \frac{\beta_\alpha}{k_{\|_m}^2 R^2} \omega_{*\alpha}(u_+ + u_-) \tag{5.31}$$

where we have assumed $\omega << \omega_{*\alpha}$ and, for the phase, $u_\pm = \omega/|k_{\|_{m\pm1}}|v_{\alpha 0} << 1$. Evaluating all quantities at the peak of the mode, we find the ratio of growth rates to be

$$\begin{aligned} \frac{\gamma_{\alpha,gap}}{\gamma_{\alpha,GAE}} &\sim \frac{(k_\|^2)_{GAE}}{(k_\|^2)_{gap}} \cdot \frac{(\omega_{*\alpha})_{gap}}{(\omega_{*\alpha})_{GAE}} \cdot \frac{(u_+ + u_-)_{gap}}{(u_+ + u_-)_{GAE}} \\ &\sim \frac{1}{(1/3)^2} \cdot \frac{(1+2)/2}{2} \cdot \frac{(1+3)}{(8+8/3)} \approx 2.5 \end{aligned}$$

since $\omega_{*\alpha} \propto m$, we have taken an average value of m: viz., $m_{ave} = [(m) + (m+1)]/2$, for the gap mode. Furthermore, we can also estimate the ratio of the critical scale length corresponding to zero growth rate:

$$\begin{aligned} \frac{(L_{\alpha,cr})_{gap}}{(L_{\alpha,cr})_{GAE}} &\sim \sqrt{\frac{(m/\omega)_{gap}}{(m/\omega)_{GAE}}} \\ &\sim \sqrt{\frac{(1+2)/2}{2/4}} = 1.7 \end{aligned}$$

Looking at Fig. 5.4, we find that these estimates agree quite well with the numerical results.

5.3.4 Curvature-Induced Electron Landau Damping

We have also considered the electron contribution to the perturbed curvature drift current on the right-hand side of Eq. (5.4). This electron term is stabilizing since $\omega_{*e}/\omega_A << 1$, where ω_{*e} is the electron diamagnetic frequency. Although the electron thermal velocity is much larger than the Alfvén phase velocity, the electron term could be comparable to the alpha term because it is proportional to the beta value of the species, and $\beta_e >> \beta_\alpha$, in general.

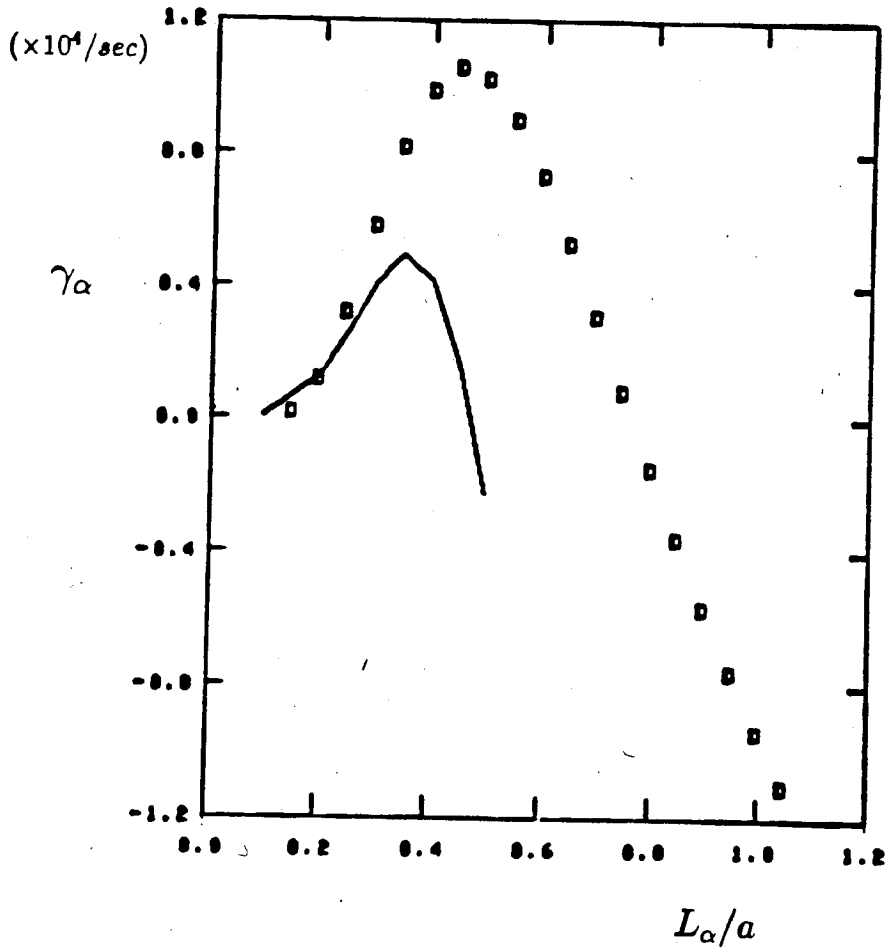

Figure 5.4: Growth rate for the $n = -1$ gap eigenmode (dotted line) and the cylindrical global eigenmode $(0, -2)$ (solid line), as functions of L_α, with CIT parameters and the profiles of Fig. 5.1.

For the gap mode that was just considered, we are able to estimate that the damping rate due to this electron curvature drift is about four times smaller than the alpha-induced growth rate and, hence, may be neglected. However, for the global Alfvén eigenmode (GAE) that we discussed in the Chap. 4, we find that this damping rate can be comparable to the alpha-induced growth rate. In particular, the most unstable GAE $(0, -2)$ mode is stabilized by this curvature-induced electron Landau damping, even without any stabilization due to finite toroidicity.

5.4 Conclusion

In this chapter we have shown that the toroidicity-induced shear Alfvén gap mode can be destabilized by fusion-product alpha particles for the parameters of the proposed Compact Ignition Tokamak. For the parameters of TFTR with tritium, we expect the GAE modes are marginal stable since the beta value of alpha particles is relatively low as compared to that of CIT. We have also demonstrated that kinetic effects such as finite ion Larmor radius do not modify the MHD global structure of the gap mode, and consequently the electron Landau damping cannot overcome the destabilizing effect of the alpha particles. More significantly, we find that the gap mode is more unstable over a wider range of values for the alpha particle density scale length than the cylindrical global modes. Therefore, the nonlinear consequences of this gap mode may be quite serious for tokamak confinement of an ignited plasma. We conclude that these gap modes deserve further theoretical and experimental investigation.

Chapter 6

Summary and Conclusions

In this thesis the two problems of access to the ballooning second stability regime and the stability of global-type shear Alfvén waves in an ignited tokamak plasma have been theoretically investigated. In a sense, these two problem are complementary: in the second stability access problem, one studies the transport, assuming that the stability properties are known; whereas with the Alfvén waves, one focuses attention on stability and temporarily neglects the associated transport. These two problems are related to the confinement of both the bulk plasma and the fusion-product alpha particles and, therefore, are of fundamental importance to tokamak ignition.

In a tokamak plasma, the operative plasma pressure is limited by the ballooning first stability limit. However, with enhancement of ballooning mode stability by means of energetic particle stabilization or other means, a bridge between first stability and second stability can be constructed by which plasma can directly gain access to the second regime. Assuming some such sort of partial stabilization of ballooning modes for small values of the shear, we found that the critical heating power needed to gain access to the second regime is proportional to the square root of the anomalous diffusion that is induced by the ballooning instability. Furthermore, we found the power scaling favors tokamaks with large aspect ratio. In fact, an experiment of this sort (the SRX tokamak) has been proposed specifically for investigating access to and operating in the high-beta regime of second stability.

In order to have an accurate assessment of the access power, it is necessary to incorporate into our model a realistic equilibrium and heating profile and to have the correct anomalous diffusivity induced by the ballooning instability. Therefore, studies of the behavior of nonlinear ballooning modes and their induced transport are highly recommended. It could also be useful to apply our transport treatment to study the transition from the L-mode to the H-mode in auxiliary heated divertor tokamaks. In fact, it has been proposed that the enhancement of ballooning stability due to the current sheet near the separatrix in a divertor tokamak could be a senario to explain the H-mode phenomena [56].

Although highly energetic particles can stabilize ballooning modes and be helpful for access to the second regime of stability, they also drive various MHD waves unstable. In particuar, the highly energetic alpha particles that will be created during ignition can destabilize shear Alfvén waves. Here we retained the full effects of toroidicity in a theoretical description of global-type shear Alfvén waves that can be destablized by such alpha particles. We found that the global Alfvén eigenmodes (GAE) are likely to be stable for the parameters of CIT due to the stabilizing effect of finite toroidicity. Other mechanisms, such as the curvature-induced electron Landau damping, could provide additional stabilization. We expect that the same stabilization of the GAE modes could occur in the International Thermonuclear Experimental Reactor (ITER) since its parameters are very similar to that of CIT. For the parameters of TFTR with tritium, the GAE modes are strongly stable since its alpha particle beta value is very low.

Meanwhile, toroidicity also introduces a discrete toroidal global shear Alfvén gap mode (TAGE), which we found to be more easily destabilized by

the alpha particles than the cylindrical GAE modes. In particular, for the parameters of CIT, we found that the TAGE mode is unstable even with the inclusion of the curvature-induced electron Landau damping. We also expect the same destabilization could occur in ITER. However, for the parameters of TFTR with tritium, the TAGE mode is likely to be stable since the beta value of alpha particles will be low.

We caution that our results on the cylindrical global eigenmodes, as well as Alfvén gap modes, are somewhat dependent on the details of plasma profiles—in particular, the plasma edge conditions, such as the value of the safety factor and the density. Therefore, it would be worthwhile to extend our work eventually to a more realistic equilibrium and to a regime where the profiles are unique, e.g., such as the H-mode phase of a diverted tokamak. Ultimately, experimental investigation of toroidal effects is needed in order to determine the damping rate of these global-type shear Alfvén waves.

Our studies indicate that in the presence of alpha particles, the toroidal shear Alfvén gap modes are the most unstable global Alfvén modes. However, the existence of these gap modes has not been yet confirmed experimentally. Considering their potentially detrimental effects on confinement and the uncertainty of the plasma profile, various experimental studies of these gap modes would be recommended.

Finally, nonlinear studies of both types of global Alfvén modes are needed in order to assess their possible detrimental effects on the confinement of both bulk plasma and the fusion alpha particles.

BIBLIOGRAPHY

[1] Troyon et al., Plasma Physics and Controlled Fusion **26**, 209 (1984).

[2] Troyon et al., Nucl. Fusion **23**, 1475 (1983).

[3] M. N. Rosenbluth, S. T. Tsai, J. W. Van Dam, and M. G. Engquist, Phys. Rev. Lett. **51**, 1967 (1983).

[4] H. Naitou, J. W. Van Dam, and D. C. Barnes, Nucl. Fusion **27**, 765 (1987).

[5] R. L. Miller and J. W. Van Dam, Nucl. Fusion **27**, 2101 (1987).

[6] R. L. Miller and R. W. Moore, Phys. Rev. Lett. **43**, 765 (1979).

[7] M. S. Chance, S. C. Jardin, and T. H. Stix, Phys. Rev. Lett. **51**, 1963(1983)

[8] B. Coppi, G. B. Crew, and J. J. Ramos, *Comments on Plasma Physics and Controlled Fusion* **8**, 11 (1983).

[9] B. Coppi, A. Ferreira, J. W. Mark, and J. J. Ramos, Nucl. Fusion **19**, 715 (1979).

[10] B. Coppi, A. Ferreira, and J. J. Ramos, Phys. Rev. Lett. **44**, 990 (1980).

[11] J. M. Greene and M. S. Chance, Nucl. Fusion **21**, 453 (1981).

[12] M. Azumi, T. Tsunematsu, K. Itoh, T. Tuda, G. Kurita, T. Takeda, T. Takizuka, S. Tokuda, T. Matsuura, Y. Tanaka, S. Inoue, and M. Tanaka, in *Plasma Physics and Controlled Nuclear Fusion Research*, Proceedings of the 8th International Conference, Brussels, 1980 (IAEA, Vienna, 1981) Vol. I, p. 293

[13] J. W. Connor, J. B. Taylor, and M. F. Turner, Nucl. Fusion **24**, 642 (1984).

[14] D. B. Nelson and H. Grad, Oak Ridge Natl. Lab. Rep. ORNL/TM-1587 (1979).

[15] S. M. Kaye and R. J. Goldston, Nucl. Fusion **25**, 65 (1985).

[16] SRX Group, Columbia University Report No. 109 (1987).

[17] B. A. Carreras, P. H. Diamond, M. Murakami, et al., Phys. Rev. Lett. **50**, 503 (1983).

[18] D. B. Nelson and C. L. Hedrick, Nucl. Fusion **19**, 239 (1979).

[19] J. W. Van Dam and Y. C. Lee, in *Proceedings of the EBT Ring Workshop* (ORNL, Oak Ridge, TN, 1979), Conf. 791288, p. 471.

[20] H. L. Berk, C. Z. Cheng, M. N. Rosenbluth, and J. W. Van Dam, Phys. Fluids **26**, 2642 (1983).

[21] K. McGuire, R. Goldston, M. Bell, M. Bitter, K. Bol, K. Brau, D. Buchenauer, T. Crowley, S. Davis, F. Dylla, H. Eubank, H. Fishman, R. Fonck, B. Grek, R. Grimm, R. Hawryluk, H. Hsuan, R. Hulse, R. Izzo, R. Kaita, S. Kaye, H. Kugel, D. Johnson, J. Manicham, D. Manos, D. Mansfield, E. Mazzucato, R. McCann, D. McCune, D. Monticello, R. Motley, D. Mueller, K. Oasa, M. Okabayshi, K. Owens, W. Park, M. Reusch, N. Sauthoff, G. Schmidt, S. Sesnic, J. Strachan, C. Surko, R. Slusher, H. Takahasi, F. Tenney, P. Thomas, H. Towner, J. Valley, and R. White, Phys. Rev. Lett. **50**, 891 (1983).

[22] J. Weiland and L. Chen, Phys. Fluids **28**, 1359 (1985)

[23] J. W. Van Dam et al., in *Plasma Physics and Controlled Nuclear Fusion Research* 1986 (IAEA, Vienna 1987).

[24] E. M. Barston, Ann. Phys. **29**, 282 (1964).

[25] Z. Sedacek, J. Plasma Phys. **5**, 239 (1971).

[26] J. P. Goedbloed, Phys. Fluid **18**, 1258 (1975).

[27] K. Appert, R. Gruber, F. Troyon, and J. Vaclavik, Plasma Phys. **24**, 1147 (1982).

[28] D. W. Ross, G. L. Chen, and S. M. Mahajan, Phys. Fluids **25**, 652 (1982).

[29] S. M. Mahajan, D. W. Ross, and G. L. Chen, Phys. Fluids **26**, 2195 (1983)

[30] S. M. Mahajan, Phys. Fluids **27**, 2238 (1984).

[31] R. Behn, A. de Chambrier, G. A. Collins, P. A. Duperrex, A. Heym, F. Hofmann, Ch. Hollenstein, B. Joye, R. Keller, A. Lietti, J. B. Lister, J. M. Moret, S. Nowak, J. O'Rourke, A. Pochelon, and W. Simm, Plasma Phys. Contr. Fusion **26**, No. 1A, 173 (1984).

[32] T. E. Evans, P. M. Valanju, J. F. Benesch, R. D. Bengtson, Y.-M. Li, S. M. Mahajan, M. E. Oakes, D. W. Ross, Z.-Z. Wang and J. G. Watkins, Phys. Rev. Lett. **53**, 1743 (1984); R. D. Bengtson, T. E. Evans, Y.-M. Li, S. M. Mahajan, M. E. Oakes, D. W. Ross, C. M. Surko, P. M. Valanju, X.-Z. Wang, and J. G. Watkins, Proc. Fourth Joint Varenna-Grenoble Int. Symposium on Heating in Toroidal Plasma, Roma (International School of Physics, Varenna, 1984),Vol. **1**, p. 121.

[33] Liu Chen and A. Hasegawa, Phys. Fluids **17**, 1399 (1974).

[34] A. B. Mikhailovskii, Zh. Eksp. Teor. Fiz. **68**, 1772 [Sov. Phys. – JETP **41**, 890 (1975)]

[35] M. N. Rosenbluth and P. H. Rutherford, Phys. Rev. Lett. **34**, 1428 (1975).

[36] K. T. Tsang, D. J. Sigmar, and J. C. Whitson, Phys. Fluids **24**, 1508 (1981).

[37] Y. M. Li, S. M. Mahajan, and D. W. Ross, Phys. Fluids **30**, 1466 (1987).

[38] X. P. Pao, Nucl. Fusion **15**, 631 (1975).

[39] C. Z. Cheng and M. S. Chance, Phys. Fluids **29**, 3695 (1986).

[40] J. P. Freidberg and D. J. Sigmar, Bull. Amer. Phys. Soc. **29**, 370 (1984)

[41] J. P. Freidberg, S. P. Hakkarainen and D. J. Sigmar, *Annual Controlled Fusion Theory Meeting* (Madison, Wisconsin, 15–17 April, 1985), paper 2B4.

[42] W. H. Choe and J. P. Freidberg, Phys. Fluids **29**, 1766 (1986)

[43] R. J. Goldston, Plasma Phys. Controlled Fusion **26**, 87 (1984).

[44] R. J. Hastie and K. W. Hesketh, Nucl. Fusion **21**, 651 (1981).

[45] W. M. Tang, R. L. Dewar, and J. Manickam, Nucl. Fusion **22**, 1081 (1982).

[46] P. J. Fielding and F. A. Haas, Phys. Rev. Lett. **41**, 801 (1978).

[47] C. M. Bishop and R. J. Hastie, *Annual Controlled Fusion Theory Meeting* (Madison, Wisconsin, 15–17 April, 1985), paper 1R2.

[48] L. JR. Spitzer, *Physics of Fully Ionized Gases* (Interscience Publishers, New York, Second Revised Edition, 1982), p. 139.

[49] T. Tuda, M. Azumi, G. Kurita, T. Takizuka, and T. Takeda, Japan Atomic Energy Research Institute, Report JAERI–M 9472 (1981).

[50] A. A. Ware and F. A. Haas, Phys. Fluids **9**, 956 (1966).

[51] V. D. Shafranov and E. I. Yurchenko, Zh. Eksp. Teor. Fiz. **53**, 1157 (1967) [Sov. Phys. JETP **26**, 682 (1968)]

[52] A. B. Mikhailovskii and E. I. Yurchenko, Plasma Phys. **24**, 977 (1982).

[53] A. B. Mikhailovskii, V. V. Demchenko, and A. Ya. Omelchenko, Fiz. Plazmy **9**, 351 (1983) [Sov. J. Plasma Phys. **9**, 204 (1983).]

[54] R. Z. Sagdeev, in *Reviews of Plasma Physics*, Vol. 4, edited by M. A. Leontovich (translated from the Russian by Consultants Bureau, New York, 1966), p.23.

[55] G. A. Navratil and T. C. Marshall, *Comments on Plasma Physics and Controlled Fusion* **10**, 185 (1986).

[56] C. M. Bishop, Nucl. Fusion **26**, 1063 (1986).

[57] S. Seki, T. Tsunematsum, M. Azumi, and T. Menoto, Nucl. Fusion **27**, 330 (1987).

[58] J. Manickam, N. Pomphrey and A. M. M. Todd, PPPL Report No. 2420 (1987).

[59] L. Chen, R. B. White, and M. N. Rosenbluth, Phys. Rev. Lett. **52**, 1122 (1984).

[60] C. Z. Cheng, Bull. Amer. Phys. Soc. bf 32, 1771 (1984)

[61] T. H. Stix, presented at the *Second International Symposium on the Heating in Toroidal Plasma*, Como, Italy (1980).

[62] S. Riyopoulos and S. Mahajan, Phys. Fluids **29**, 731 (1986).

[63] N. Dominguez, Ph.D. thesis, University of Texas at Austin, Report IFSR No. 245. (1986)

[64] H. Biglari and L. Chen, Phys. Fluids **29**, 1760 (1986).

[65] R. Izzo, P. A. Monticello, W. Park, J. Manickam, H. R. Strauss, R. C. Grim, and K. McGuire, Phys. Fluids **26**, 2240 (1983).

VITA

Guo-yong Fu was born on June 15, 1962, in Ningbo, Zhejiang, the People's Republic of China, the son of Xin-ting Fu and An-yu Zhou. He entered the University of Science and Technology of China in Hefei, Anhui, China, majoring in physics, and received the degree of Bachelor of Science in physics in July of 1983. In September, 1983, he entered the Graduate School of the University of Texas at Austin and was employed as a teaching assistant in the Department of Physics. Since 1984, he has been employed as a reseach assistant in the Institute for Fusion Studies of the University of Texas at Austin.

Permanent address: 89 Zhongma Street
Ningbo, Zhejiang
China (P.R.C.)

This dissertation was typeset[1] with LaTeX by the author.

[1] LaTeX document preparation system was developed by Leslie Lamport as a special version of Donald Knuth's TeX program for computer typesetting. TeX is a trademark of the American Mathematical Society. The LaTeX macro package for The University of Texas at Austin dissertation format was written by Khe-Sing The.